SEE/TP-2004-400

Meteor Properties Database - Final Report

Principal Investigator – Dr. Robert M. Suggs
NASA Marshall Space Flight Center

Co-Investigators:
Dr. William Cooke
Computer Sciences Corporation

Dr. Peter Brown
University of Western Ontario

Collaborators:
Dr. Anthea Coster
Dr. Sigrid Close
Stephen Hunt
Denis F. Durand
MIT-Lincoln Labs

National Aeronautics and
Space Administration

Marshall Space Flight Center • MSFC, Alabama 35812

August 2004

TABLE OF CONTENTS

LIST OF FIGURES

LIST OF FIGURES (continued)

LIST OF FIGURES (continued)

LIST OF FIGURES (continued)

LIST OF FIGURES (concluded)

LIST OF TABLES

THIS PAGE INTENTIONALLY LEFT BLANK.

1. INTRODUCTION

We set out to help fill a major gap in current knowledge of the meteoroid environment by directly estimating the densities of ablating meteoroids from measurements of their decelerations. This was done by analyzing three unique data sets obtained by the high-power ALTAIR radar located on Kwajalein Atoll during the Leonid showers of 1998 and 1999. The characteristics of the ALTAIR radar were such that not only can precise meteor velocities be measured (thereby enabling determination of the decelerations), but also the trajectories of the meteors in the upper atmosphere can be ascertained, which, when combined with the velocity information, permit the establishment of accurate meteor orbits, which in turn revealed the origins of the various meteors in the data. Knowledge of the origins of these meteoroids is important for the validation of the theory behind some of the new meteoroid environment models under development.

The results contained in the database accompanying this document will have a major impact upon spacecraft meteoroid risk analyses in that, for the first time, a density distribution associated with the sporadic meteor background can be constructed, rather than the crude 3 values used in current environment models. This will permit hypervelocity experimenters to choose materials with similar bulk properties for their gun tests, and, as the density of the projectile is an important parameter in any penetration equation, enable spacecraft engineers to accurately determine penetration probabilities. It will also give designers a better handle on the plasma production capabilities of meteoroids, plasmas which can serve as conducting paths for current flows capable of disabling a spacecraft (such as OLYMPUS in 1993).

NASA TM-4527, the Natural Orbital Environments Guide For Use in Aerospace Vehicle Development, has this to say about the uncertainty in mass (density) for meteoroids with masses above 10^{-6} grams:

For meteoroids above this size, the flux is well defined but the associated mass is even more uncertain. This implies an effective uncertainty in the flux (at a set mass) of a factor of 0.1 to 10 (because of the slope of the functional relationship.

Fold in this environmental uncertainty with the other uncertainties introduced by lack of knowledge of meteoroid densities – poor projectile choices for hypervelocity gun tests and "guesstimates" for the meteoroid densities in penetration equations – and it is little wonder that spacecraft meteoroid risk assessments are little more than "back of the envelope" calculations. If one is to achieve a reasonable degree of uncertainty in these calculations, then the difficult problem of determining, with reasonable accuracy, meteoroid densities must be tackled. The work recently completed and described in this document represents the best effort to date in obtaining such densities, and the database will hopefully help relieve some of the headaches that have been plaguing designers of new spacecraft.

1.1 Uniqueness of the Data and Its Potential

The data collected by the ALTAIR radar on the Kwajalein Missile Range (KMR) during the three campaigns in 1998 and 1999 comprise the **only** simultaneous observations of meteors using seven frequencies as well as optics. ALTAIR (ARPA Long-Range Tracking and Instrumentation Radar) is a highly calibrated radar with interferometry (angle) capabilities which enables the measurement of the true positions of meteors. During the campaigns, ALTAIR detected approximately one meteoroid every second, which is the highest detection rate achieved by radar. A cursory analysis of these data has revealed that approximately 90-95% of all meteors detected by ALTAIR during a shower are sporadics.

It should be mentioned that the data were collected through not only the cooperation of the Department of Defense, but also with active participation by personnel from the Massachusetts Institute of Technology's Lincoln Laboratory. Their past involvement and extensive experience with ALTAIR make them a vital part of this work, especially in the analysis of the raw radar signatures.

Data were collected during three campaigns, including the 1998 Perseid and Leonid meteor showers, and then during the1999 Leonids. The Perseid data were collected at VHF frequencies and comprise 50 minutes of peak shower data on head echoes as well as specular trails with a peak detection rate of 1 meteoroid per second. Leonid 1998 data were collected at seven frequencies (using four radars), including VHF, UHF, L-, S-, C-, Ka- and W-band, as well as in the optical (ballistic camera). Approximately 36 minutes of data were collected on head echoes, specular and non-specular trails spanning the peak of the storm. These data show a peak detection rate of one meteoroid every two

seconds. The 1999 Leonid data were collected at VHF and UHF along with optical (visible and infrared) and have not yet been reduced or analyzed.

The primary meteor sensor employed during these three campaigns was the ALTAIR radar, due to its VHF and UHF operating frequencies. The combination of ALTAIR's capabilities with respect to its high sensitivity, its precise calibration, its dual frequency and polarization observables, and its interferometric measurements make it the best meteor radar in the world.

ALTAIR resides in the central Pacific at 9^o N and 167^o E on the island of Roi-Namur in the Kwajalein Atoll, Republic of the Marshall Islands. It is a high-power, dual-frequency radar that is capable of collecting precise measurements on small targets at long ranges. The radar utilizes a 46-m diameter, mechanically steered, parabolic dish and transmits a peak power of 6 MW simultaneously at two-frequencies, including 160 MHz (VHF) and 422 MHz (UHF). The 46-m diameter antenna employs a focal point VHF feed and multi-mode Cassegrain UHF feed in conjunction with a frequency selective sub-reflector (5.5 m diameter), giving a monopulse angle tracking capability at either frequency. Targets are illuminated with right-circularly polarized energy in a narrow half-power beam-width of 2.8^o and 1.1^o at VHF and UHF, respectively. A right circular (RC) polarization signal is transmitted, and the dual-polarization feed horns enable separate reception of left and right circular polarization. These measurements are denoted sum left circular and sum right circular. ALTAIR's receive horns are also used to collect left-circular signal returns for the purpose of angle measurement. The receivers are offset from the focus of the dish, and their signal energies are differenced to produce two additional channels of data, including the left circular azimuth difference and left-circular elevation difference. Azimuth and elevation are combined in a process known as amplitude comparison monopulse, a form of phase interferometry, to measure the angle of arrival of the radar return (for each pulse) to a small fraction of the beam width. The average angular measurement accuracy (standard deviation) of the ALTAIR system is 11.2 millidegrees in azimuth and elevation at UHF. This accuracy value is derived from orbit solutions computed for earth orbiting calibration spheres routinely tracked by ALTAIR and the NASA Laser ranging network. The results from the numerical orbit fit process are used to assess ALTAIR's residual range and angle errors. The monopulse angle data contribute to the angular error budget and on average, are estimated to be no greater than the 11.2 millidegrees computed as a part of the daily calibration monitoring of the ALTAIR system. As configured for meteor data collection using the most

accurate waveforms, the ALTAIR range accuracy is such that it can detect the meteor at 5 meter intervals along its trajectory. The radar's UHF and VHF Radar Cross Section (RCS) are regularly calibrated using a known target, a 56 cm balloon-borne sphere; the absolute RCS measurement capability of ALTAIR is within 0.5 dB. Combined with a range measurement derived from the time delay of the target return, ALTAIR angle data can be used to determine the position of an object in three dimensions as a function of RCS. The waveforms that were used in the Perseid and Leonid campaign are contained in Table 1.

Table 1. ALTAIR Waveforms.

	V40H	U150	V260M	U1000
Frequency (MHz)	160	422	158	422
Bandwidth (MHz)	3	18	1	1
PRF (Hz)	333	333	50	50
Sample Spacing (m)	30	7.5	75	75
Sensitivity (dBsm)	-55	-75	-74	-80

1.2 Highlights of Past Analyses

During the meteor campaigns, ALTAIR detected approximately one meteoroid every second, which is the highest detection rate achieved by radar. Analysis of these data has realized the following new information on meteoroids:

- Radius/density estimates from 3D angle data
- First to show deceleration is not constant over altitude (or time)
- Dependence of head echo Radar Cross Section (electron line density) on frequency
- First three-frequency head echo ever detected
- Shape of the plasma region (and meteoroid) using polarization measurements
- Shower meteoroids are not as spatially confined as previously thought (meteoroids travel up to 30^{o} off boresight)
- The apparent sporadic background average velocity observed by ALTAIR is roughly 50 km s^{-1}
- Approximately 99% of all meteors detected during a shower are sporadics
- 1-5% of all meteoroids detected appear to be interstellar in origin

To the above, we now add the 1029 meteor densities and orbits comprising this database.

2. RADAR OBSERVATIONS AND ANALYSIS

2.1 Observations

We collected meteor head echo and trail data using radars located on the Kwajalein atoll. The primary meteor radar used in this experiment was the ARPA Long-Range Tracking and Instrumentation Radar (ALTAIR). ALTAIR resides in the central Pacific at 9^o N and 167^o E (geographic) on the island of Roi-Namur in the Kwajalein Atoll, Republic of the Marshall Islands, 12 hours ahead of GMT. ALTAIR is a high-power, two-frequency radar capable of collecting accurate measurements on small targets at long ranges. We use ALTAIR primarily to conduct space surveillance for US Space Command; a picture of ALTAIR is contained in Figure 1.

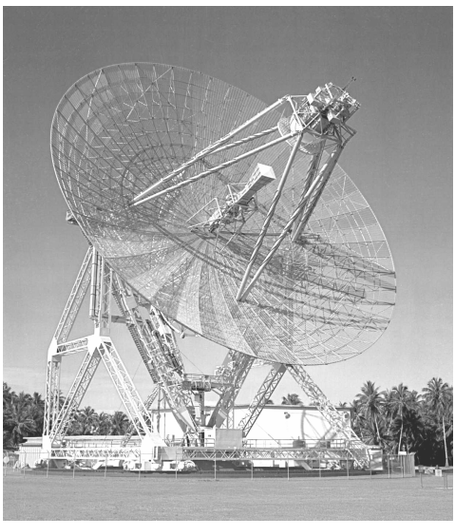

Figure 1. Picture of the ALTAIR radar, located on the Kwajalein atoll.

ALTAIR has a 46-m diameter, mechanically steered, parabolic dish that transmits a peak power of 6 MW simultaneously at two frequencies. A complex transmit and receive radio-frequency antenna feed system allows the simultaneous operation at both VHF and UHF. Targets are illuminated with right-circularly (RC) polarized signal energy in a narrow half-power beam-width of 2.8^o and 1.1^o at VHF and UHF, respectively. The reflected signal energy is focused by the dish into the dually polarized feed horn, which receives the left-circularly (LC) and right-circularly polarized signal energies separately. These two channel measurements are recorded as sum left circular and sum right circular. ALTAIR also has four additional receive horns that collect LC signal returns for the purpose of angle measurement. The received channels are offset from the focus of the dish, and the measured signal

energy is differenced to produce two additional channels of data, including the left-circular azimuth difference (ALC)[1] and left-circular elevation difference (ELC). ALC and ELC are combined in a process known as amplitude comparison monopulse [*Blake*, 1986], which is a form of phase interferometry, to measure the angle of arrival of the radar return (for each pulse) to within a small fraction of the beamwidth. Combined with a range measurement derived from the time delay of the target return, ALTAIR can determine the position of an object in three dimensions. Using the most sensitive waveforms available, ALTAIR can reliably detect a target as small as –74 decibels-relative-to-a-square-meter (dBsm) at VHF, and –80 dBsm at UHF, at a range of 100 km; recall that a dB is ten times the $\log_{10}$ of a number. This high system sensitivity makes ALTAIR well suited for the detection of meteor head echoes. Table 2 contains the parameters of the ALTAIR system. Table 2 contains the parameters of the ALTAIR system.

Table 2. Parameters of the ALTAIR system.

Frequency	160 MHz	422 MHz
Antenna Diameter	46 m	46 m
Beamwidth	2.8^o	1.1^o
Peak Power	6.0 MW	6.4 MW
Xmit Polarization	RC	RC
Rec Polarization	LC, RC	LC, RC

We conducted three meteor experiments using the Kwajalein sensors. These experiments include the Perseid 1998 shower, which peaks on August 12, as well as the Leonid 1998 and Leonid 1999 showers, which peak on November 17. Our approach was to determine the position of the radiant, and then point the radar boresite at this position and allow the head echoes to travel through the beam. We collected data in 2 to 15-minute segments, and then adjusted our boresite position as the radiant moved across the sky. Primarily we stared at the radiant in order to observe meteoroids that travel directly down the beam; however, we also executed some off-radiant pointing in order to determine the

[1] Although commonly referred to as the azimuth channel, the measurement is actually of a traverse variation from boresite, converted to an azimuth variation by dividing by the cosine of the boresite elevation.

sporadic flux, as well as to collect trail data. We describe the experiments in this section, including the waveforms used to collect the data and the pointing.

2.1.1 Perseid Shower 1998

The first meteor data collection occurred during the peak of the Perseid meteor shower on August 12, 1998 using ALTAIR. The purpose of this experiment was to determine ALTAIR's suitability for meteor head echo and trail detection. We collected data by staring at a fixed point in space for a determined length of time using VHF (158 MHz) only. The data collections included both on-radiant and off-radiant pointing. First, ALTAIR pointed on-radiant for 5 minutes beginning at 12:55 AM local time. Next, ALTAIR pointed off-radiant for 15 minutes beginning at 4:45 AM local time. Finally, ALTAIR pointed on-radiant for 5 minutes beginning at 5:10 AM local time. While the radar is pointing at the radiant, Perseid meteoroids follow paths roughly aligned with the antenna beam and therefore endure longer in the beam.

We recorded in-phase and quadrature data for each of the four receive channels, including RC, LC, ALC and ELC, and we collected samples every 75 m for ranges corresponding to altitudes between 70 and 140 km. ALTAIR radiated a VHF 260-*?* s pulse (V260M) 50 times per second using a Bandwidth of 1 MHz; this pulse repetition frequency (PRF) of 50 Hz discriminates against many short-lived head echoes. The pulse was modulated with a 1-MHz linear frequency modulation, which allowed the pulse to be compressed to 1 *?* s after receive filtering. Using this waveform, ALTAIR can detect a –72 dBsm target at 100-km range. The time, pointing azimuth and elevation, and waveform and PRF data are contained in inting.

Table 3 (Kwajalein is 12 hours ahead of GMT); the shaded line corresponds to off-radiant pointing.

Table 3. Perseid 1998 pointing using the ALTAIR radar.

Time	Azimuth	Elevation	Waveform	PRF
12:55 GMT	30?	10?	V260M	50 Hz
16:45 GMT	345?	40?	V260M	50 Hz
17:10 GMT	8?	40?	V260M	50 Hz

2.1.2 Leonid Shower 1998

We collected Leonid data at Kwajalein on November 17, 1998, during a 3-hour period, which we designed to span the predicted peak of the Leonid storm (07:30 AM local time). Four radars, including ALTAIR, TRADEX, ALCOR and MMW as well as a ballistic camera were pointed simultaneously on and off-radiant. Only ALTAIR (160, 422 MHz) data are described herein, due to its lower operating frequencies and therefore higher detection rates; no head echoes were detected using ALCOR and MMW. We recorded in-phase and quadrature data for each frequency using the four receive channels for altitudes spanning 70 to 140 km at VHF and 90 to 110 km at UHF. The smaller UHF altitude extent was necessitated by the limit on disk space. The two ALTAIR waveforms used to collect the majority of these data were a 40 ?sec VHF pulse (30 meter range spacing), and a 150 ?sec UHF pulse (7.5 meter range spacing). Using these waveforms at 100 km range, ALTAIR can detect a –55 dBsm target at VHF, and a -75 dBsm target at UHF. We primarily utilized a 333 Hz pulse-repetition frequency (PRF) for its high sampling rate. The time, pointing azimuth and elevation, ecliptic latitude and longitude, and waveform and PRF data associated with the Leonid 1998 experiment is contained in

Table 4. The shaded lines correspond to off-radiant pointing.

Table 4. Leonid 1998 pointing using the Kwajalein radars.

Time	Azimuth	Elevation	Longitude	Latitude	Waveform	PRF
15:00 GMT	70º	29º	145.6º	9.6º	V260M/U1000M	50 Hz
15:15 GMT	30º	31º	124.0º	37.1º	V260M/U1000M	50 Hz
18:20 GMT	43º	72º	146.3º	10.1º	V40H/U150	333 Hz
18:40 GMT	30º	74º	146.3º	11.1º	V40H/U150	333 Hz
19:40 GMT	328º	75º	145.0º	9.1º	V40H/U150	333 Hz
20:20 GMT	357º	68º	155.9º	23.9º	V40H/U150	333 Hz
20:40 GMT	302º	64º	144.9º	9.4º	V40H/U150	333 Hz
21:00 GMT	298º	60º	145.1º	9.3º	V40H/U150	333 Hz
21:18 GMT	295º	55º	144.1º	8.9º	V40Ha/U150a	50 Hz
21:30 GMT	294º	53º	144.8º	9.1º	V40Ha/U150a	50 Hz

2.1.3 Leonid Shower 1999

We collected Leonid data at Kwajalein on November 17, 1999, during an 11-hour period. The peak of the storm occurred over Europe, and we therefore missed the peak detection rate; we collected data from 2:40 AM local time on November 17 through 1:20 PM local time on November 18 in 2-minute segments. ALTAIR and optical instruments were pointed simultaneously on-radiant only. Our goal was to collect head echo data while pointing on-radiant simultaneously with radar and optical in order to cross-calibrate RCS with visual magnitude. Unfortunately, while ALTAIR detected numerous head echoes, inclement weather prevented us from collecting any optical meteor data.

We recorded in-phase and quadrature data at each frequency using four receive channels for altitudes spanning 70 to 140 km at VHF and 90 to 110 km at UHF. The two ALTAIR waveforms used in collecting the data were identical to the ones primarily used during the Leonid 1998 shower. These include a 40 ?sec VHF pulse (30 meter range spacing), and a 150 ?sec UHF pulse (7.5 meter range spacing) using a 333 Hz PRF. The radar pointing for the Leonid 1999 shower is contained in Table 5.

Table 5. Leonid 1999 pointing using the Kwajalein radars.

Time	Azimuth	Elevation	Longitude	Latitude	Waveforms	PRF
14:40 GMT	69.3º	19.7º	149.7º	11.7º	V40H/U150	333 Hz
14:48 GMT	69.3º	21.5º	147.0º	10.8º	V40H/U150	333 Hz
15:04 GMT	69.3º	25.3º	149.6º	11.8º	V40H/U150	333 Hz
15:12 GMT	69.3º	27.2º	149.5º	11.8º	V40H/U150	333 Hz
15:20 GMT	69.3º	28.9º	149.6º	11.8º	V40H/U150	333 Hz
16:50 GMT	66º	49.5º	149.7º	11.8º	V40H/U150	333 Hz
16:54 GMT	65.8º	50º	150.1º	12.0º	V40H/U150	333 Hz
16:58 GMT	65.5º	51.4º	149.7º	11.7º	V40H/U150	333 Hz
17:06 GMT	64.7º	53.2º	149.7º	11.7º	V40H/U150	333 Hz

2.2 Data Reduction and Processing

2.2.1 Introduction

Data reduction begins with understanding and translating the form of the original data, and ends with the final calculations of ranging data (range and range rate) and angle offsets from boresite (using

monopulse information), along with the error estimates for these data. The following reduction steps are described:

- ? Noise and Bias Determination
- ? Data Thresholding and Interpolation
- ? Streak Detection
- ? Streak Modeling and Regression
- ? Monopulse Correction

The subject of meteor physical quantities (mass, density, etc.) is treated in subsequent sections.

This section makes use of the following terminology:

Head Echo	The radar return by a single meteor from a single radar pulse.
Streak	The collection of head echoes for a single meteor.
Range Window	The range (time) extent observed by the radar for returns from a single pulse.
Sample Gate	A segment of the range window for which a sample of the receiver signal amplitude is recorded in digital counts. Such a sample is taken for each of four channels: sum left circular, sum right circular, traverse difference, and elevation difference. A typical range window consists of about 2000 to 3000 sample gates.
Gate Set	A group of sample gates corresponding to a single echo. These gates are interpolated to locate the maximum amplitude and its associated range.
Data Collection Period	The collection of all sample gates for a single pulse (i.e., all the sample gates for one range window).
Collection Sequence	The sequence of Data Collection Periods produced by a single "run" or "mission" of the radar for either UHF or VHF, corresponding to a single data file.
Data Collection Packet	The data from both Data Files for a single "run" (if both exist).

2.2.2 Source Data

The ALTAIR radar collected data using the waveforms listed in

Table 6, and stored the data on several DLT (Digital Linear Tape) cartridges. Each cartridge contained several data files. Some of the tapes were entirely unreadable, and some files on the readable tapes were unrecoverable. The recovered data collection packets are listed in Table 7, which includes the collection sequence, its waveforms and durations.

Table 6. Waveforms.

Waveform	Frequency (MHz)	Bandwidth (MHz)	Pulsewidth (microsec)	Sample Spacing (m)	PRF (Hz)
U1000M	422	1	1000	75	50
U150	422	18	150	7.5	333
U150A	422	18	150	7.5	50
V260M	158	1	260	75	50
V40H	160	3.5	40	30	333
V40HA	158	3.5	40	30	50

Table 7. Recovered Collection Periods.

Sequence	UHF		VHF	
	Waveform	Minutes	Waveform	Minutes
perseids1_539			V260M	4.99
perseids2_541			V260M	15.00
leonids1_1500	U1000M	5.10	V260M	5.12
leonids2_1515	U1000M	4.09	V260M	5.01
leonids3_1820	U150	1.99	V40H	2.00
leonids4_1840	U150	1.32	V40H	2.01
leonids7_1940			V40	2.02
leonids9_2020	U150	1.99	V40H	1.97
leonids10_2040	U150	1.31	V40H	1.97
leonids11_2_2100	U150	1.99	V40H	2.01
leonids12_2118	U150A	8.67	V40HA	10.09
leonids13_2130	U150A	6.90	V40HA	6.88
dcp2_321_1440			V40H	2.00
dcp3_321_1448			V40H	1.99
dcp5_321_1504			V40H	2.03
dcp6_321_1512			V40H	1.99
dcp7_321_1520			V40H	2.03
dcp9_321_1650	U150	0.04		
dcp9_321_1654	U150	1.27		
dcp10_321_1658	U150	1.99	V40H	2.01
dcp11_321_1706	U150	1.94	V40H	1.95

The packet naming conventions include, for 1998: the meteor shower name, the collection packet number, and the time of day (GMT); for 1999: the data collection packet number (dcp<n>), the Julian day number (321 in all cases), and the time of day in GMT.

The data files are in binary format, with a data collection period for each radar pulse. The collection period data consists of a header, followed by radar samples for each of four channels: sum left circular (LC, with complex components LCI and LCQ), sum right circular (RC, components RCI and RCQ), traverse difference (TR, components TRI and TRQ, related to azimuth error via the elevation of boresite), and elevation difference (EL, components ELI and ELQ). Figure 2 illustrates the collection bit pattern.

Header

Bit 15	8 7	Bit 0
Header Flag Word		
Sequence Number		
Status Buffer		Status Buffer
Status Buffer		Status Buffer
DFB Interface CCA Status		
Number of Sample Patterns in Previous Collection Period		
Number of Sample Gates		
Binary Time of Day (bits 15:0)		
Binary Time of Day (bits 31:16)		
(zero filled)		Binary Time of Day (bits 39:32)

Radar Sample Gate Values in Counts

Sum Left Circular Q (gate 1)
Sum Left Circular I (gate 1)
Sum Right Circular Q (gate 1)
Sum Right Circular I (gate 1)
Transverse Offset Q (gate 1)
Transverse Offset I (gate 1)
Elevation Offset Q (gate 1)
Elevation Offset I (gate 1)
…
Sum Left Circular Q (gate n)
Sum Left Circular I (gate n)
Sum Right Circular Q (gate n)
Sum Right Circular I (gate n)
Transverse Offset Q (gate n)
Transverse Offset I (gate n)
Elevation Offset Q (gate n)
Elevation Offset I (gate n)

Figure 2. Bit Arrangement for a Single Collection Period

Only a subset of the collection period data, described below, was used in the data reduction process:

Header Flag Word	Identifies the beginning of a collection period (set to AA55h).
Sequence Number	16-bit binary value defining the sequence number of the collection period within the mission.
DFB Interface CCA Status	Used only bits 3 to 0, which are set to indicate which channels are enabled. Checked for all four enabled.
Number of Sample Gates	Counts the total number of data words (16-bit), or sample gates, received by any one of the four channels during the collection period.
Binary Time of Day	The four segments are concatenated to form the full 40-bit number, taken as the time of pulse emission, in hundreds of nanoseconds since midnight.
Radar Samples[2]	Values in digital counts (integers) proportional to the voltage of the radar return signal in each channel for each sample gate, as given by its quadrature (Q) and in-phase (I) complex components.

Figure 3 provides an illustration of what the data represents. For each transmitted pulse, the receiver listens for echoes during a time span (before the next pulse is transmitted) corresponding to a desired range window. Figure 4 depicts the range window and its corresponding sample gates. If a meteor is streaking through this window, the maximum amplitude of the return echo will appear at a gate number corresponding to the meteor's range for that echo (the return of a single echo is actually dispersed over about 3 to 8 sample gates, depending upon the parameters of the transmitted waveform--this is discussed later)[3].

[2] Two of the data files (leonids10_2040 UHF and VHF) contained collection periods for which the number of radar samples did not match (were less than) the number given by the "Number of Sample Gates" word. These periods were filtered out. Data file leonids6_1920 VHF contained no good collection periods.

[3] Note that a data point in these plots indicates a position in space and time. The amplitude of the received signal echo emanating from that position is a third dimension not shown here, indicated by colors in later plots.

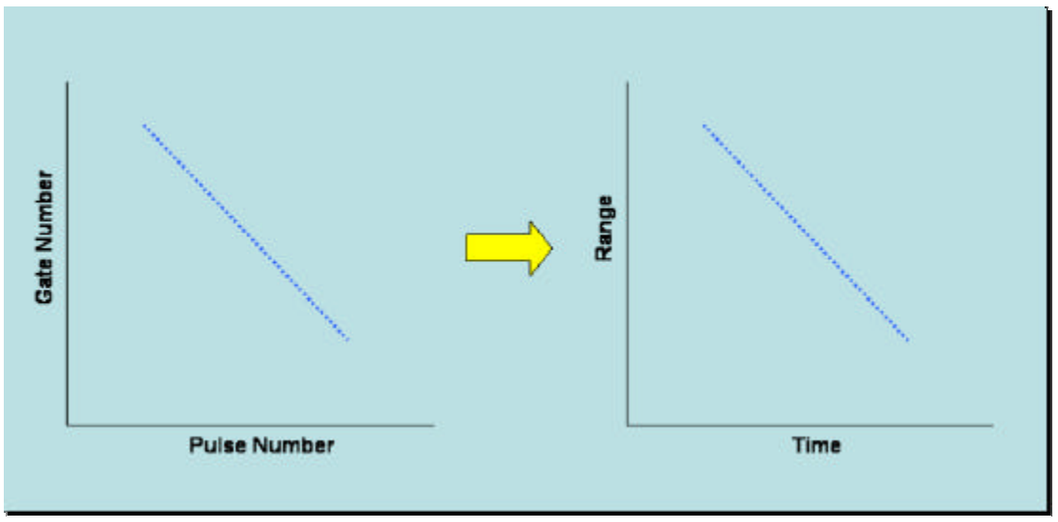

Figure 3. Gate vs. Pulse Equivalence to Range vs. Time

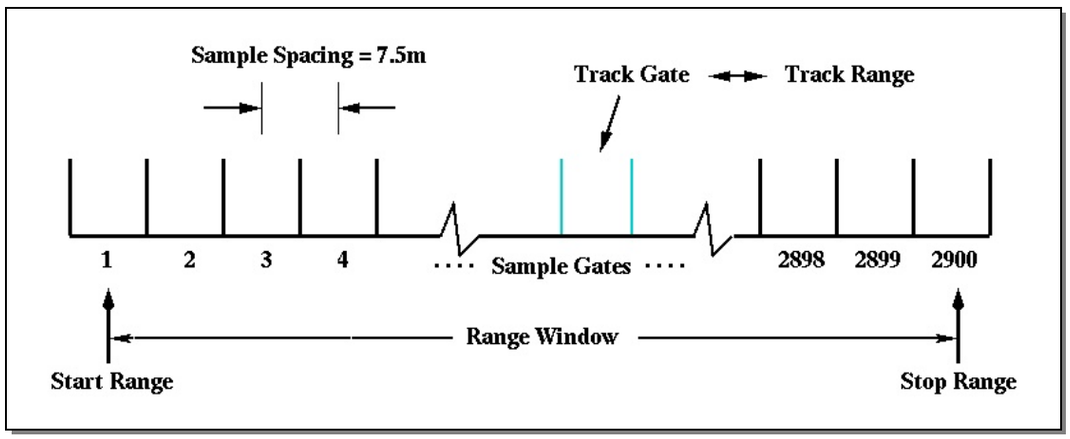

Figure 4. Sample Gate Geometry (U150 Waveform)

The result is a streak of points, one for each returned echo of each pulse. To transform from gate/pulse space to range/time space, the size of each sample gate is needed (sample spacing, in time or length), along with the associated range of each sample gate. The sample spacing values for each of the waveforms used is given in

Table 6. The number of sample gates per collection period, as well as the track gate and track range, is listed in Table 8. The track range is the range associated with the track gate, from which all other sample gate ranges and times are inferred.

The range r_g and time t_g associated with a given sample gate g are therefore given by

$$r_g \; ? \; r_T \; ? \; ? s ? g \; ? \; g_T ? \quad \text{and} \quad t_g \; ? \; t_p \; ? \; r_g / c ,$$

where r_T is the track range, $? s$ is the sample spacing, g_T is the index of the track gate, t_T is the pulse transmit time, and c is the speed of light.

Table 8. Sample Gate Parameters.

Sequence	UHF			VHF		
	# Sample Gates	Track Gate	Track Range (km)	# Sample Gates	Track Gate	Track Range (km)
perseids1_539				4000	1	350.0
perseids2_541				1600	1	108.0
leonids1_1500	1904	670	201.329226	1904	670	201.329226
leonids2_1515	1904	670	190.177427	1904	670	190.177427
leonids3_1820	2900	1450	105.060682	2640	1133	105.060682
leonids4_1840	2900	1450	103.964006	2640	1133	103.964006
leonids7_1940				2640	1133	103.470311
leonids9_2020	2900	1450	107.717926	2640	1133	107.717926
leonids10_2040	2900	1450	111.056655	2640	1133	111.056655
leonids11_2_2100	2900	1450	115.174484	2640	1133	115.174484
leonids12_2118	2900	1	101.7	2640	1	79.2
leonids13_2130	2900	1	101.7	2640	1	79.2
dcp2_321_1440				2900	1450	291.299603
dcp3_321_1448				2900	1450	270.4344
dcp5_321_1504				2900	1450	235.1928
dcp6_321_1512				2900	1450	221.0008
dcp7_321_1520				2900	1450	209.8090
dcp9_321_1650	2900	1450	135.9779			
dcp9_321_1654	2900	1450	135.9779			
dcp10_321_1658	2900	1450	132.4005	2900	1450	132.4005
dcp11_321_1706	2900	1450	129.3033	2900	1450	129.3033

2.2.3 Noise and Bias Determination

Each of the four receiver channels samples provides a value of the received amplitude for every sample gate, and the vast majority of the sampled data is a mix of system thermal noise and background sky noise, occasionally "dotted" with a bona fide echo. An estimation of the magnitude of the noise floor was used in calculating signal-to-noise ratios (*SNR*) for the head echoes, and for establishing a threshold value for data selection. The receiver biases were estimated and removed from all sampled data passing the *SNR* threshold.

Figure 5 through Figure 8 are histograms of the distribution of gate sample count values for Leonids 1998:1840 VHF and UHF, and Leonids 1999:1658 VHF and UHF respectively, showing the nicely Gaussian behavior with small offsets from zero mean due to the receiver biases. Each chart represents data from an entire collection sequence, or file.

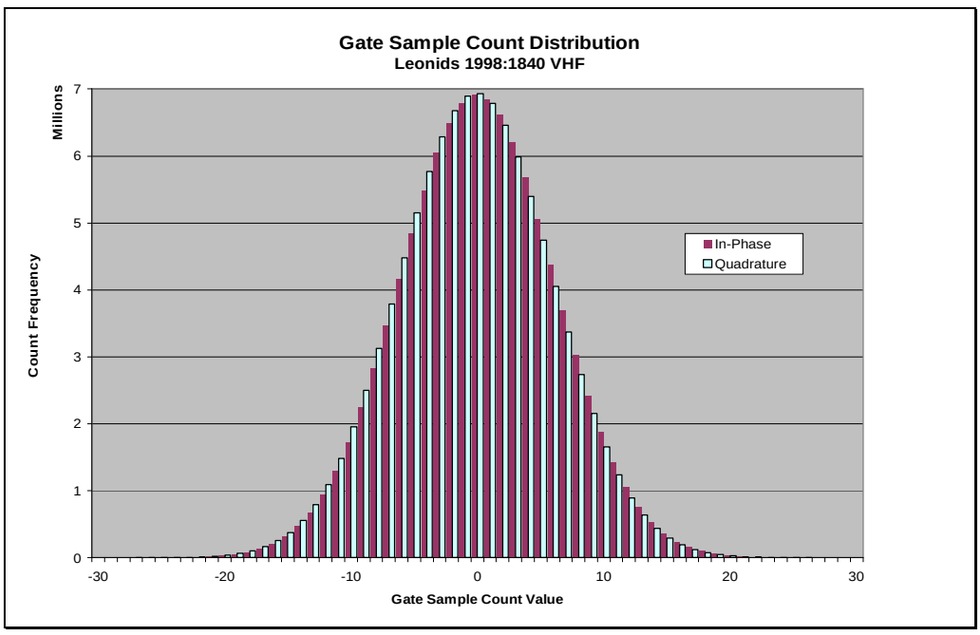

Figure 5. Gate Sample Count Distribution for Leonids 1998:1840 VHF.

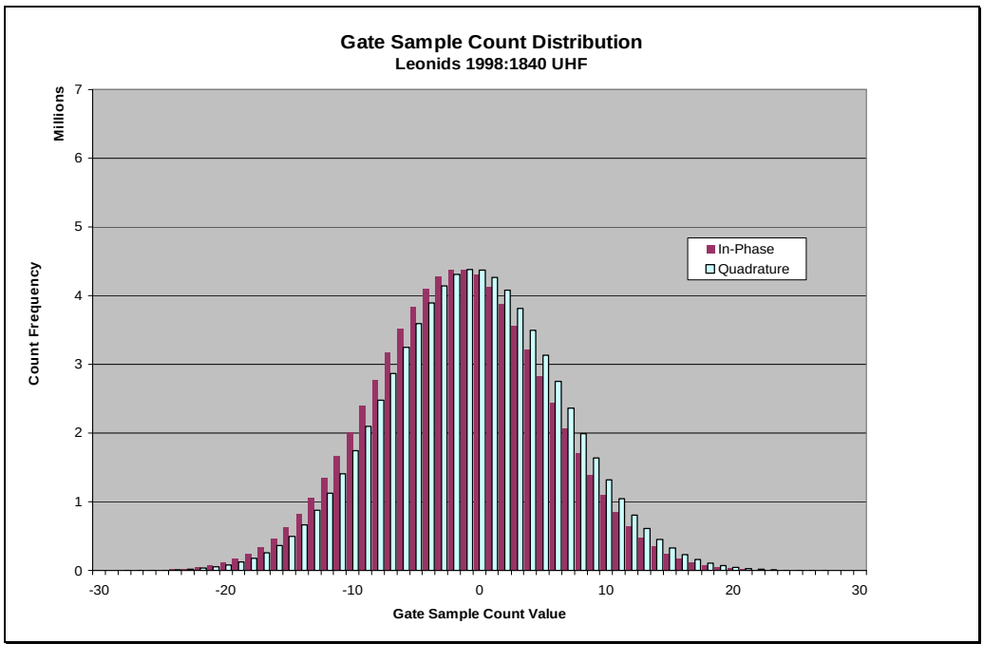

Figure 6. Gate Sample Count Distribution for Leonids 1998:1840 UHF.

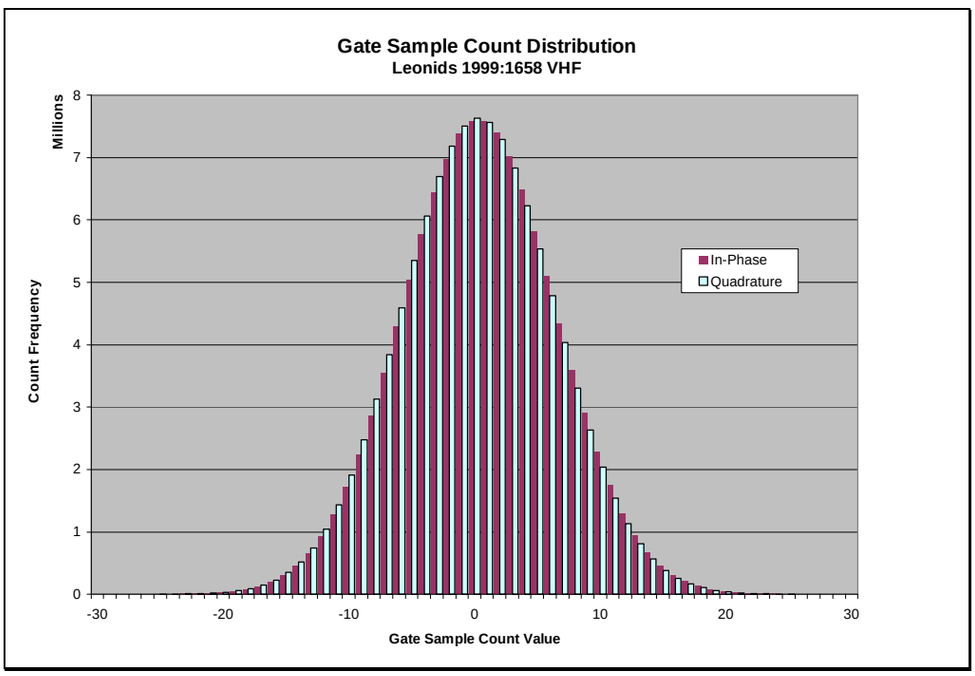

Figure 7. Gate Sample Count Distribution for Leonids 1999:1658 VHF.

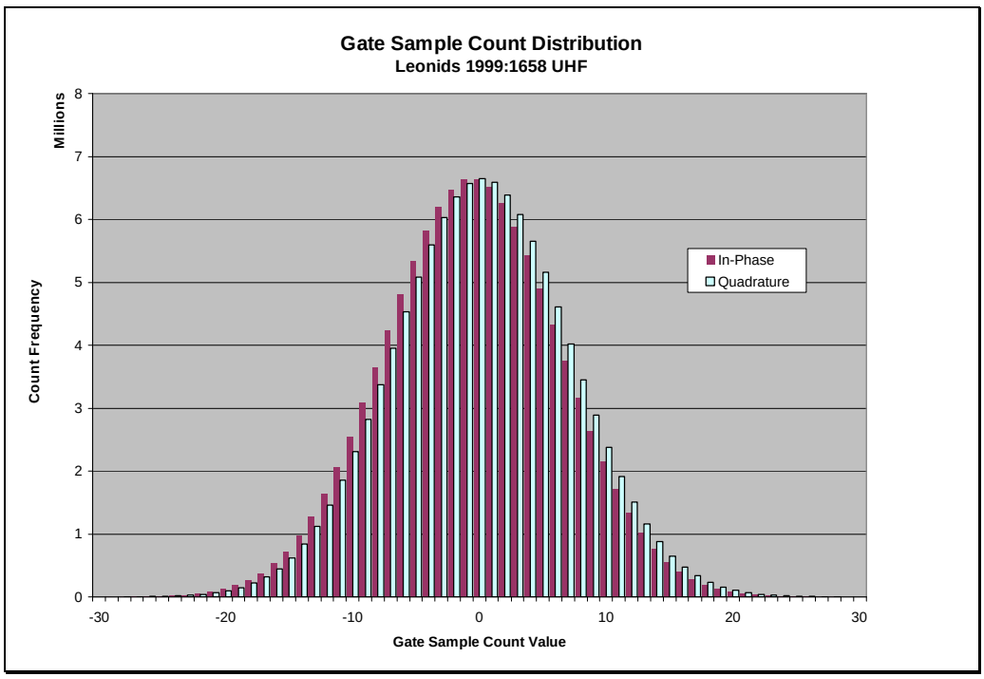

Figure 8. Gate Sample Count Distribution for Leonids 1999:1658 UHF.

2.2.3.1 Biases

Beginning with the estimation of receiver biases for the *I* and *Q* components,

$$\bar{I} = \frac{\sum I_i}{n}, \qquad \bar{Q} = \frac{\sum Q_i}{n},$$

where the index *i* spans an entire file of all gates for all pulses, and *n* is the total number of *I* and *Q* pairs for the given file. Alternately, binning[4] the data provides for

$$\bar{I} = \frac{\sum f_{I,j} I_j}{\sum f_{I,j}}, \qquad \bar{Q} = \frac{\sum f_{Q,k} Q_k}{\sum f_{Q,k}},$$

where the indices *j* and *k* span the collection of count values for an entire file, and f_I and f_Q are the *I* and *Q* count frequencies of the *j*th and *k*th count values respectively ($\sum f_{I,j} = \sum f_{Q,k} = n$). Ideally, the *I* and *Q* values in these expressions are strictly noise data, but the noise to head echo ratio is sufficiently large to consider the effect of the presence of head echo signal to be insignificant when estimating noise and biases. However, counts with absolute values greater than 50 were excluded[5] from the bias and noise

[4] Binning was used to conveniently produce bin/frequency files for graphical views of the large quantity of data. The bins were single count, the resolution of the source data.

[5] This was an arbitrary value chosen after viewing the behavior of the distributions.

estimation process. The biases are applied to all *I* and *Q* data that is thresholded (discussed in the next section) by

$$I_{g,unbiased} = I_g - \bar{I}, \quad \text{and} \quad Q_{g,unbiased} = Q_g - \bar{Q},$$

where *g* is an arbitrary sample gate number for a given pulse.

2.2.3.2 Noise

The *SNR* for the *g*th sample gate value is given by

$$SNR_g = \frac{A_g^2}{s_{noise}^2},$$

where

$$A_g = \sqrt{I_{g,unbiased}^2 + Q_{g,unbiased}^2},$$

and s^2_{noise} is the unbiased estimate for the variance of the noise floor. The source data *I* and *Q* values are in digital counts, which are proportional to the receiver signal voltage, so the squares are maintained to produce a ratio of powers. In dB,

$$SNR_{g,dB} = 10\log\left(\frac{A_g^2}{s_{noise}^2}\right)$$

We estimated the noise floor variance, on a per file basis, by

$$s_{noise}^2 = \frac{\sum (I_i - \bar{I})^2 + \sum (Q_i - \bar{Q})^2}{n - 1},$$

where again the index *i* spans the entire file of all gates for all pulses. Expanding and simplifying yields

$$s_{noise}^2 = \frac{\sum I_i^2 + Q_i^2 - n\left(\bar{I}^2 + \bar{Q}^2\right)}{n - 1}.$$

Using the previously collected binned data,

$$s_{noise}^2 = \frac{\sum f_{I,j} I_j^2 + \sum f_{Q,k} Q_k^2 - n\left(\bar{I}^2 + \bar{Q}^2\right)}{n - 1}.$$

Table 9 lists the resulting noise and bias values.

Table 9. Noise and Bias Estimates by File.

File	Bias (counts)						Noise Variance (counts^2)		
	LCI	LCQ	AZI	AZQ	ELI	ELQ	LC	AZ	EL
leonids1_1500.uhf	0.538	-0.541	0.165	-0.501	0.071	1.162	107.97	135.93	146.94
leonids1_1500.vhf	-0.221	-0.74	-0.166	0.366	-0.179	-0.38	25.57	22.6	19.2
leonids2_1515.uhf	1.42	-0.719	1.753	-0.642	-1.124	0.513	115	145.91	155.12
leonids2_1515.vhf	-1.05	-0.456	-0.008	-0.516	-0.364	-0.317	47.05	35.8	47.24
leonids3_1820.uhf	-1.314	-0.641	-0.412	-0.944	-1.14	-0.42	90.35	117.72	132.69
leonids3_1820.vhf	0.565	-0.55	-0.265	0.33	0.397	-0.567	76.1	62.87	53.76
leonids4_1840.uhf	-1.436	-0.647	-0.332	-0.852	-1.169	-0.441	89.68	118.12	133.06
leonids4_1840.vhf	0.155	-0.307	-0.584	0.572	0.687	-0.191	74.68	62.85	52.57
leonids7_1940.vhf	0.777	-0.682	0.312	0.947	1.072	-0.404	75.04	60.54	50.24
leonids9_2020.uhf	-1.446	-0.732	-0.348	-0.85	-0.917	-0.197	98.14	119.95	136.7
leonids9_2020.vhf	1.165	-0.576	-0.85	1.237	0.594	-0.221	91.97	74.24	58.59
leonids10_2040.uhf	-1.264	-0.7	-0.394	-0.932	-0.951	-0.189	93.21	117.37	134.22
leonids10_2040.vhf	0.925	-0.527	-0.8	1.304	0.676	0.454	76.54	62.03	50.08
leonids11_2_2100.uhf	-1.437	-0.752	-0.349	-0.864	-1.115	-0.546	90.35	116.64	129.06
leonids11_2_2100.vhf	0.819	-0.036	-1.129	0.727	1.023	-0.128	76.93	63.25	49.08
leonids12_2118.uhf	-1.563	-0.684	-0.608	-0.835	-1.081	-0.845	90.22	116.43	126.44
leonids12_2118.vhf	0.535	-1.048	-0.347	0.837	0.607	0.166	84.7	72.53	58.62
leonids13_2130.uhf	-1.559	-0.698	-0.563	-0.843	-1.08	-0.879	89.83	116.59	126.28
leonids13_2130.vhf	0.101	-0.512	-0.816	0.7	0.721	0.152	77.66	67.32	50.79
perseids1_539.vhf	-0.349	-1.056	-0.292	0.144	0.296	-0.869	35.84	30.84	22.63
perseids2_541.vhf	-1.075	-1.006	-0.842	0.268	0.125	-0.385	32.54	29.03	24.05
dcp2_321_1440.vhf	0.025	-0.695	0.475	1.074	0.755	-0.34	75.69	56.36	39.59
dcp3_321_1448.vhf	0.024	-0.129	-0.373	0.83	0.27	-0.498	73.95	56.81	41.08
dcp5_321_1504.vhf	0.402	0.648	0.556	1.139	0.222	-0.753	71.07	55.48	39.58
dcp6_321_1512.vhf	0.245	0.429	0.043	1.133	0.689	-0.332	71.85	55.82	40.29
dcp7_321_1520.vhf	0.741	0.319	0.438	1.671	0.496	-0.209	70.97	52.31	40.54
dcp9_321_1650.uhf	-0.488	0.008	0.15	-0.301	-0.965	-0.752	96.43	115.57	118.44
dcp9_321_1654.uhf	-0.481	0	0.088	-0.303	-0.699	-0.32	95.82	115.59	119.96
dcp10_321_1658.uhf	-0.414	0.069	0.024	-0.341	-0.698	-0.116	95.54	115.48	120.02
dcp10_321_1658.vhf	0.532	0.127	0.086	1.288	0.976	-0.209	73.68	55.33	38.72

2.2.4 Data Thresholding and Interpolation

The reduction of the raw source data began by reading the binary data files while simultaneously performing a two-step filtering process: 1) thresholding on the basis *SNR*, and 2) retaining only groups of sample gates (henceforth called gate sets) suitable for interpolation based on the expected Linear Frequency Modulation (LFM) pulse compression output behavior. These steps are described below.

2.2.4.1 Thresholding

Dominated by noise, the raw source data was filtered in order to retain only the sample gate values with an *SNR* above a predetermined value. In more common radar applications, the choice of thresholding criteria is motivated by optimizing detection probability. In this application, however, all the receiver values have been collected and are available in stored form for all sample gates, thus the thresholding becomes a matter of reducing the processing computer's resource requirements for memory, disk space, and processing time, as well as optimizing both the algorithmic and manual components of the streak identification process. To this end, the threshold values were set as listed in Table 10, where $s_{noise} \; ? \; \sqrt{s_{noise}^2}$.

Table 10. Signal Threshold Values.

Frequency	Signal Threshold Value (counts)
VHF	2.25 $s_{noise,\ vhf}$
UHF	(0.9) 2.25 $s_{noise,\ uhf}$

The UHF data is less dense, affording a slightly lower threshold value. The threshold values differ from file to file according to the file-specific noise floor variance, but the resulting threshold *SNR* was about 7dB.

2.2.4.2 Gate Set Identification and Interpolation

As mentioned above, ALTAIR was configured to operate with an LFM pulse compression scheme. Figure 9 illustrates.

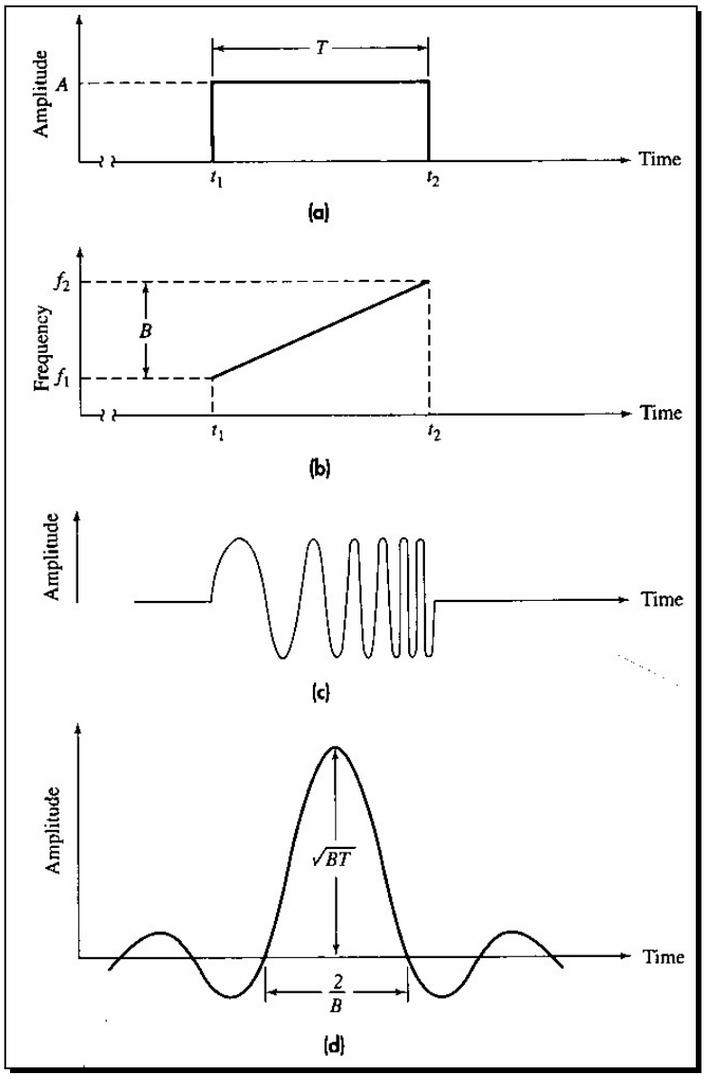

Figure 9[6]. Linear Frequency Modulation (LFM) Pulse Compression. (a) envelope of transmitted waveform; (b) frequency of transmitted waveform as a function of time; (c) representation of the LFM waveform; (d) theoretical output from the pulse-compression filter.

The source data, which are digital samples of the output from the pulse-compression filter for the entire range window of a given pulse, includes samples of a waveform whose ideal shape follows the function Sinc(Bt) = $\sin(Bt)/(Bt)$, shown in Figure 9(d), when a legitimate echo is received. The second step of the reduction process was to group sample gates into gate sets that are samples of the center lobe of this waveform. All other threshold-passing gates were filtered out. To further illustrate,

[6] [Skolnik, 2001]

Figure 10 shows a plot of amplitude versus sample gate number for LC, TR, and EL for a single head echo.

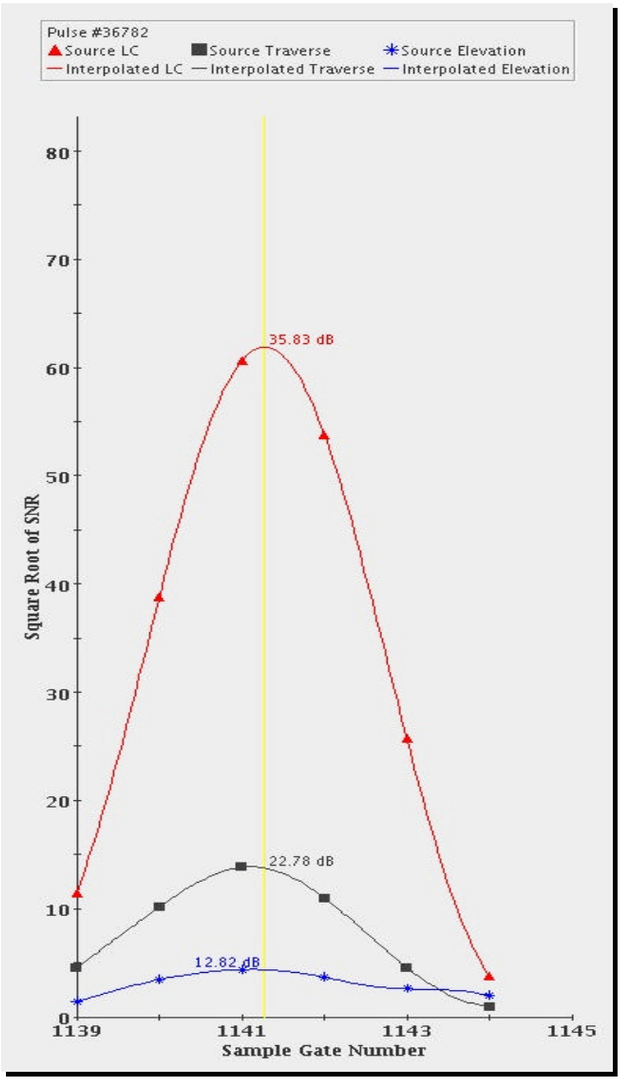

Figure 10. Amplitude vs. Sample Gate Number for a Single Echo.

The filtering process identified gate sets as three or more pulse-contiguous LC sample gates with a single maximum. The associated TR and EL data are also retained. Then, in order to obtain the value and location of the maximum amplitude of the LC return, each gate set was interpolated by recovering the sampled waveform using

$$a(t) = \sum_{g} a(g)\,Sinc(g - t)$$

$$Sinc(g - t) = \begin{cases} 1, & t = g \\ \dfrac{\sin(g - t)}{(g - t)}, & t = g \end{cases}$$

where *a* is the amplitude, *g* is the integer sample gate number of the source data, and *t* is a floating point sample gate value between the first and last gates of the gate set. The choice of interpolation resolution was 1.5 meters, which is less than the smallest sample gate size (7.5 meters), but large enough for good computational speed. The location of the maximum (as a floating-point sample gate value) converts to the range, and the amplitude (in counts) converts to a value for radar cross-section (RCS).

The location of the maximum LC (indicated by a vertical yellow line in Figure 10) was also used to select values for TR and EL, which eventually became angular offsets from boresite. It is important to note here that the LC, TR, and EL maximums of the data were rarely if ever coincident in time. The Sinc function approach is an interpolation, not anestimation, and therefore yields a waveform influenced by the noise, particularly with low *SNR*, which is the case in the difference channels when the boresite offsets are small.

Figure 11 gives an example of head echo data belonging to a single streak, showing another cross-section (indicated by the green vertical line in the left plot and shown in the right plot) of amplitude vs. sample gate for one of the pulses.

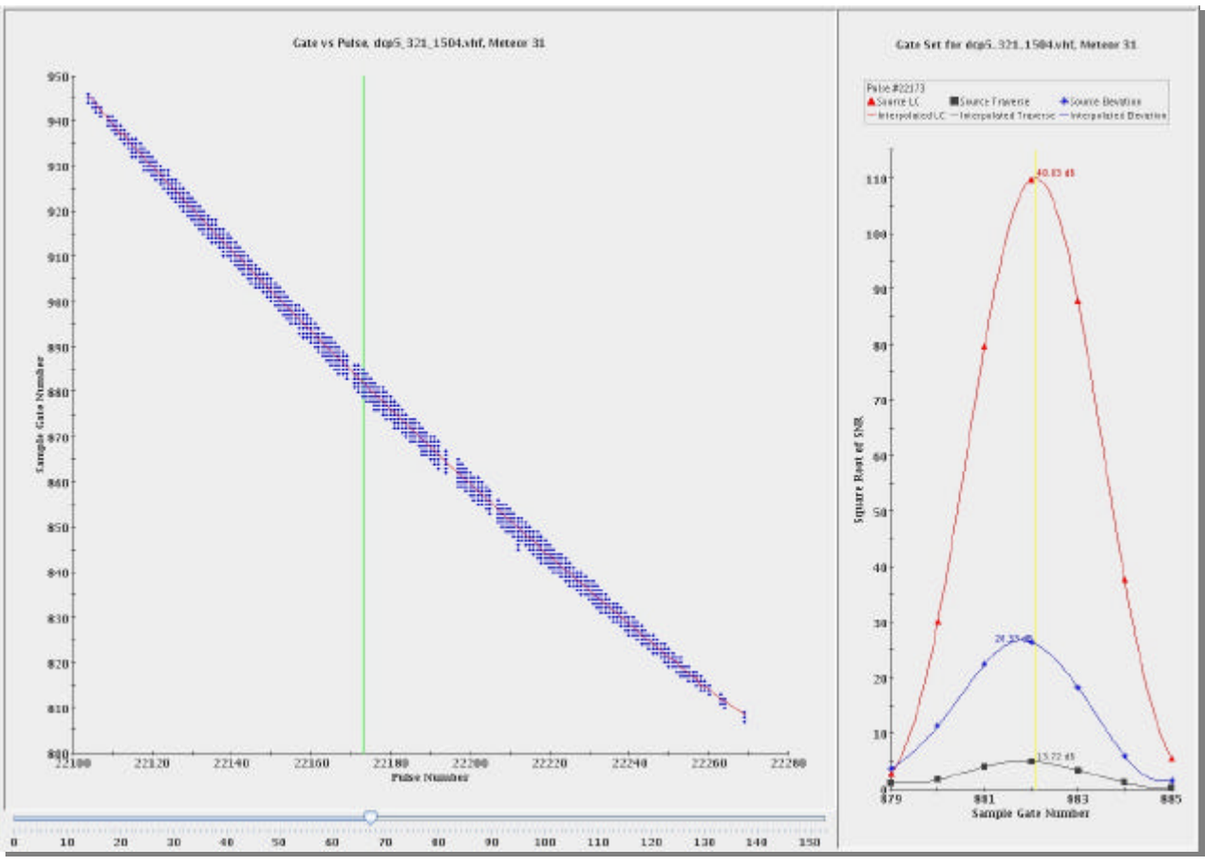

Figure 11. Pre-interpolated Streak and Cross-section.

The solid red line in the left plot joins the maximum thresholded values of the LC amplitude, which are later submitted to a linear regression once identified and tagged as streak head echoes.

2.2.5 Streak Detection

Figure 12 shows a file of data after thresholding and interpolation. The meteor streaks can be seen in the noise, which includes intermittent “bursts” appearing as the vertical columns. Zooming in on a section to the right and center, Figure 13 shows the streaks more pronounced, and with a further zoom to the far right, Figure 14 shows a streak with a trail.

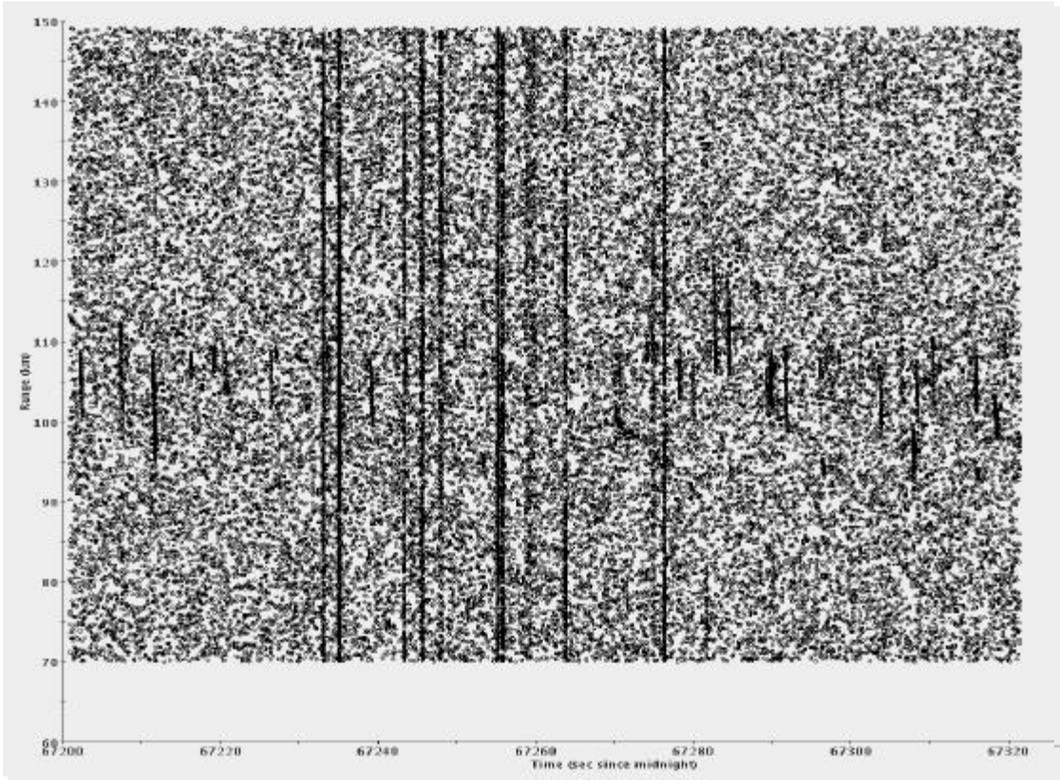

Figure 12. Thresholded and Interpolated Data for a Single File (Leonids 1840 VHF).

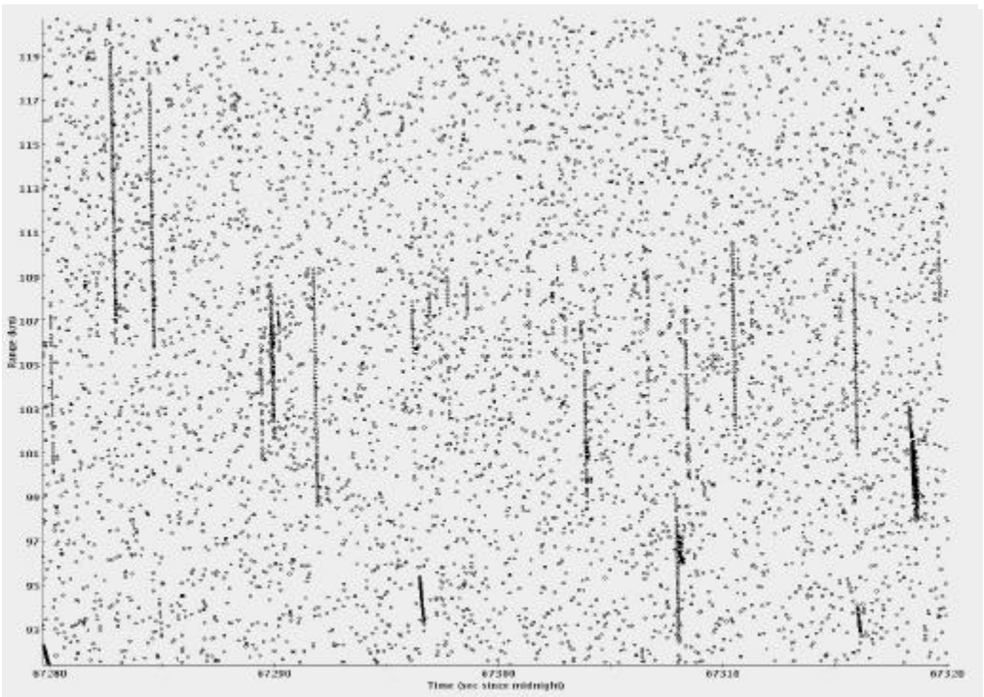

Figure 13. Zooming in on a section of Figure 10.

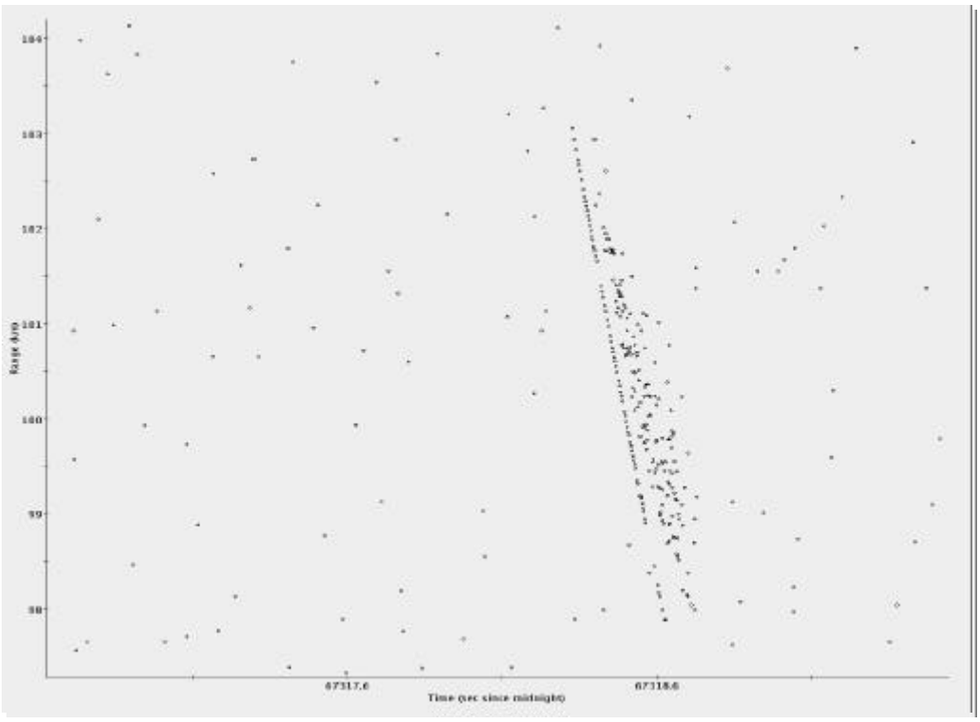

Figure 14. A Closer Look at a Single Streak with a Trail.

We developed an algorithm for automatic streak detection, beginning with sorting the data by pulse and gate, and then performing the following procedure:

1. Identify the next untagged data point. This becomes the "starter."
2. Proceed to the next pulse and identify the next untagged point which, when combined with the starter, produces a range rate (calculated by range differencing) of absolute value less than RR_{max}. This becomes the "anchor." If there is no anchor in the pulse immediately following the starter pulse, return to step 1.
3. Proceed to the next pulse, retaining the first data point that extrapolates the line joining starter and anchor in range/time space to within an extrapolation tolerance of plus or minus EX_{tol} sample gates. If there is no third pulse-contiguous data point, return to step 1.
4. Proceed to the next pulse, retaining the first data point that extrapolates the line joining the previous two points in range/time space to within the tolerance EX_{tol}. This step is repeated to the end of the file data.

5. Juxtapose anchor with starter and perform step 4 in reverse sort order, repeating to the beginning of the file data.

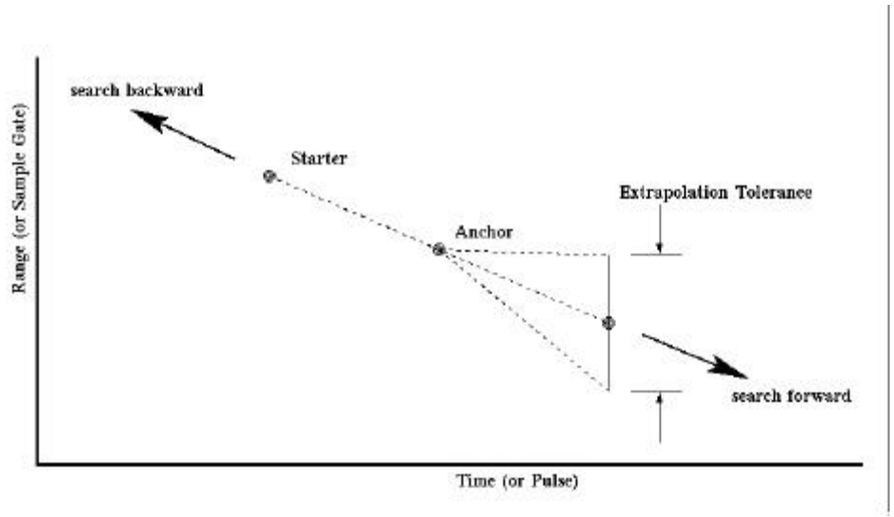

Figure 15. Streak Echo Identification.

6. If the number of head echoes tagged for this streak is less than H_{min}, reject and return to step 1.
7. Perform a straight line fit on the tagged echoes, rejecting this collection of head echoes as a streak (i.e., retag them as noise) if the correlation coefficient of the fit is less than CC_1. If rejected, return to step 1.
8. Examine the residuals from the fit of step 6. Echoes with fit error greater than ER_{max} are retagged as noise. The remaining echoes are again submitted to a straight line fit, rejecting the streak and returning to step 1 if the correlation coefficient is less than CC_2.
9. Perform a quadratic fit in LC amplitude vs. time. If the resultant fit is not concave down, reject and return to step 1.
10. Perform a manual verification and manual retag as necessary.

Steps 2 and 3 begin the streak identification by locating 3 pulse-contiguous data points that satisfy the range rate bounds. Step 4 continues the forward search without the contiguity constraint, and step 5 resumes the search in the reverse direction, with step 6 imposing a minimum head echo count. This procedure does not demand straight lines, as the extrapolation tolerance allows for curves. However, the

majority of streaks from this data set were nearly linear, allowing for steps 7 and 8[7]. We adjusted the values of the various search parameters, listed in Table 11, to minimize false detections, which occurred mostly in trails. Step 9 aided greatly in avoiding streak identification in trail points, given that legitimate streaks generally begin with low LC amplitude, "brighten" in the middle, and then taper off. We then manually edited the false or missed tags via graphical software specifically designed for this work.

Table 11. Streak Detection Parameters.

Parameter	Description	Value
RR_{max}	Maximum range rate absolute value	150 km/sec
EX_{tol}	Linear extrapolation tolerance for streak head echo selection	6 times sample spacing
H_{min}	Minimum number of head echoes for a streak	5
ER_{max}	Maximum linear fit error (residual) for an individual head echo	1.7 times the root mean square error of the fit
CC_1	Minimum correlation coefficient for the first linear fit	0.8
CC_2	Minimum correlation coefficient for the second linear fit	0.9997

Of interest at this point is one very large trail, shown in Figure 16, which required manual tagging *before* we invoked the above procedure.

Figure 17 and Figure 18 complete this section with a view of the tagged streaks from Leonids 1840 VHF and UHF respectively.

[7] The physics of the deceleration and the geometry of the radar tracking can likely produce a curved range-time profile, however the high velocities coupled with the mostly boresite-parallel trajectories may have contributed to the typically "straight" nature of the streaks identified in this study.

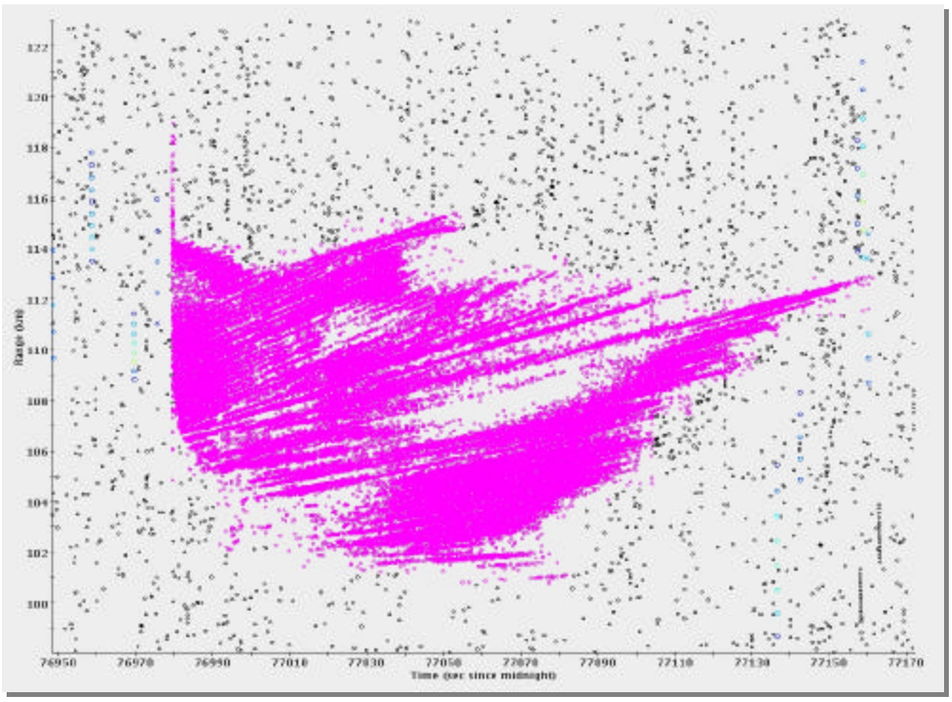

Figure 16. Large Trail in Leonids 1998:2118 VHF.

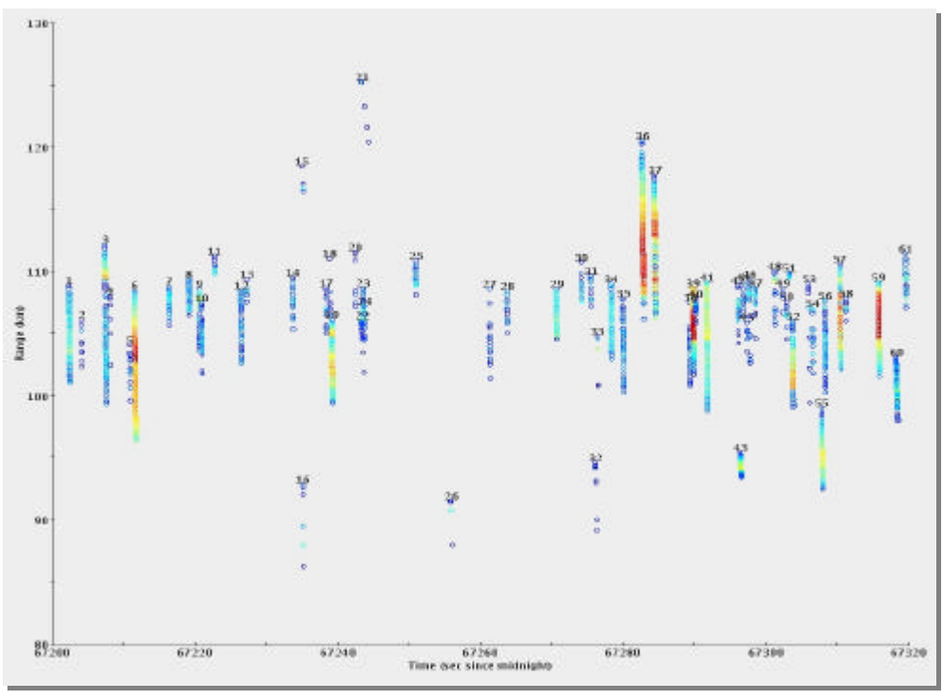

Figure 17. Leonids 1998:1840 VHF Tagged.

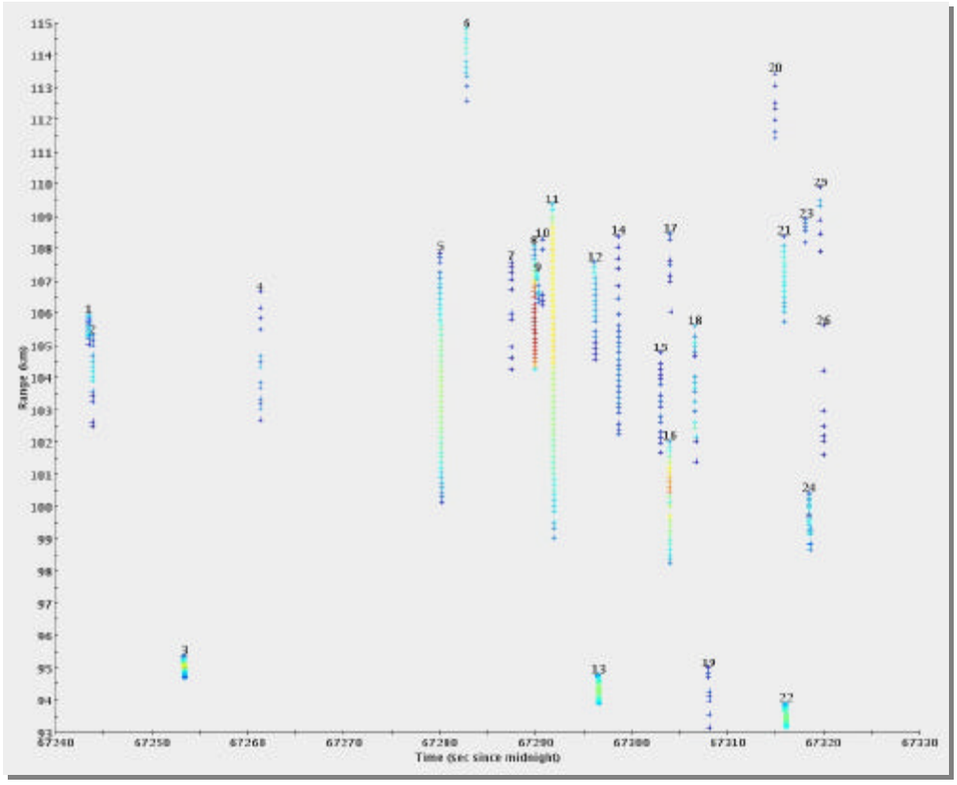

Figure 18. Leonids 1998:1840 UHF Tagged.

2.2.6 Streak Modeling and Regression

With all head echoes tagged according to streak number, we then physically modeled the range-time relationship of the. This provided for the smoothing of the noise-influenced interpolated range values and yielded range rate via differentiation. The range rate and higher derivatives was used in the subsequent analysis of the head echo parameters, but was also needed to remove the effects of range Doppler coupling (RDC). RDC is an artifact of the Linear FM pulse compression scheme, which produces an error in the apparent range given by

$$? _r ? \frac{Tf_0 \dot{r}}{B} ? k\dot{r},$$

where T is the pulse duration, f_0 is the center frequency, B is the bandwidth, and $\dot{r}$ is the range rate, so that

$$r_c = r_m + k\dot{r},$$

where r_m and r_c are the measured and corrected ranges respectively. Based on the deceleration physics of the meteor head, we modeled the fitted range in normalized[8] range-time space by

$$r_{fit} = a_0 + a_1 t + a_2 e^t,$$

$$\dot{r}_{fit} = a_1 + a_2 e^t$$

Using the corrected range and range rate in a linear regression with random error ε,

$$r_c = r_{fit} + \varepsilon,$$

or

$$r_m + k_N (a_1 + a_2 e^t) = a_0 + a_1 t + a_2 e^t + \varepsilon,$$

where k_N is the normalized k. Rearranging yields

$$r_m = a_0 + a_1 t + k_N \left[a_2 (1 + k_N) e^t \right] + \varepsilon,$$

which was used to populate the normal equations for the linear regression, yielding the estimated values of the coefficients, and finally r_{fit}. We weighted the regression by making use of the usual equation [Toomay, 1998] for the rms range accuracy:

$$\sigma_R = \frac{c}{4B\sqrt{SNR}},$$

where c is the speed of light. SNR, and therefore σ_R, takes on a unique value for each r_m. The i_{th} weight is then $w_i = 1/\sigma_{R_i}^2$, so for a given streak, the diagonal weighting matrix is

$$W = \begin{bmatrix} w_1 & & & & & \\ & w_2 & & & 0 & \\ & & \ddots & & & \\ & & & \ddots & & \\ & 0 & & & \ddots & \\ & & & & & w_n \end{bmatrix},$$

where n is the number of echoes in the streak. With the matrices X, A, and R defined by

[8] The data for each streak was normalized by the range and time means and standard deviations for that streak

$$X = \begin{bmatrix} 1 & t_1 - k_N & (1 - k_N)e^{t_1} \\ 1 & t_2 - k_N & (1 - k_N)e^{t_2} \\ \vdots & \vdots & \vdots \\ 1 & t_n - k_N & (1 - k_N)e^{t_n} \end{bmatrix}, \quad A = \begin{bmatrix} a_0 \\ a_1 \\ a_2 \end{bmatrix}, \quad R = \begin{bmatrix} r_{m_1} \\ r_{m_2} \\ \vdots \\ r_{m_n} \end{bmatrix},$$

the weighted least squares estimators of the regression coefficients are

$$A = (X'WX)^{-1} X'WR,$$

where X' denotes the transpose of *X*. The estimated 3 by 3 variance-covariance matrix of the regression coefficients is then

$$S^2(A) = MSE_w (X'WX)^{-1},$$

where the MSE_w (weighted mean square error) is given by

$$MSE_w = \frac{\sum w_i (r_{m_i} - r_{fit_i})^2}{n - 3}.$$

Finally, the estimated variance for the fitted range value r_{fit_i} is

$$s^2(r_{fit_i}) = X_i S^2(A) X_i',$$

where X_i is the i_{th} row of the X matrix.

2.2.7 Monopulse Correction

Monopulse refers to the process of determining the observed object's angular offset from boresite using information from the echo of a single pulse. Specifically, for ALTAIR at the time the source data was collected, the amplitudes of the difference signals in the EL and TR channels relate to the elevation and traverse offset angles θ_{EL} and θ_{TR} by

$$\theta_{EL} = s_{EL}(d_{EL} - x_{EL} d_{TR})$$
$$\theta_{TR} = s_{TR}(d_{TR} - x_{TR} d_{EL}),$$

where d_{EL} and d_{TR} are the real components, in digital counts, of complex divisions, given by

$$d_{EL} \; ? \; \mathrm{Re}\left\{\frac{?\,ELI \; ? \; ELQj\,?}{?\,LCI \; ? \; LCQj\,?}\right\},$$

$$d_{TR} \; ? \; \mathrm{Re}\left\{\frac{?\,TRI \; ? \; TRQj\,?}{?\,LCI \; ? \; LCQj\,?}\right\},$$

s_{EL} is the elevation monopulse slope in radians per count, x_{EL} is the dimensionless elevation cross-term, and s_{TR} and x_{TR} are the slope and cross-term for traverse. The resultant offset angles are in radians. The azimuth offset is then simply

$$? \; _{AZ} \; ? \; \frac{? \; _{TR}}{\cos\left(?El\,?\right)},$$

where *El* is boresite elevation. Note that these monopulse relationships are intended for normal radar tracking operations where the offset angles are kept small enough through tracking to remain within the linear region of the radar. This region is roughly within the half-power beamwidth of the radar, which for this data collection was about 1.06 degrees for UHF and 2.80 degrees for VHF. Some of the source-data monopulse values are outside this region (see Reduction Summary).

The approach taken here was to fit the monopulse offset angle data to straight lines. Again, the physics and geometry of the meteor trajectories could produce curved offset angle behavior, but identifiably curved profiles were not observed, possibly due to the presence of the noise[9]. Figure 19 through Figure 22 give examples of the usual monopulse responses. In these figures, the solid straight red line is the fit for azimuth, and the blue is for elevation (the individual data points are color coded to the sum channel's amplitude – blue is low, red is high).

[9] A bit of a "catch 22" here: near-boresite observations result in low difference channel signals and therefore low SNR, but the tracking of larger offset angles is precluded by design.

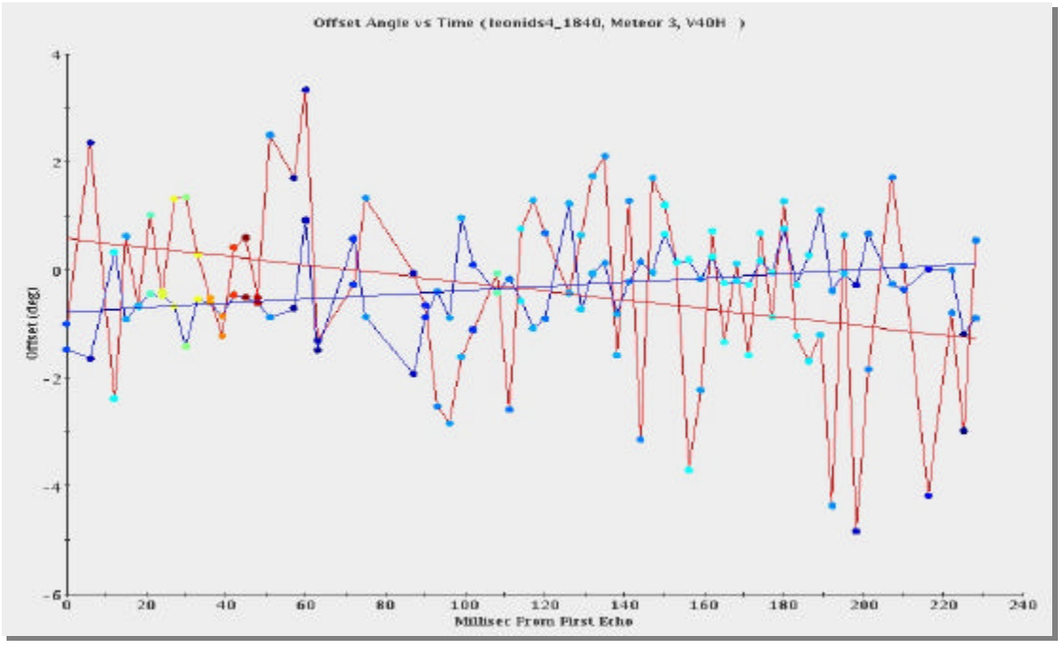

Figure 19. Monopulse Example 1.

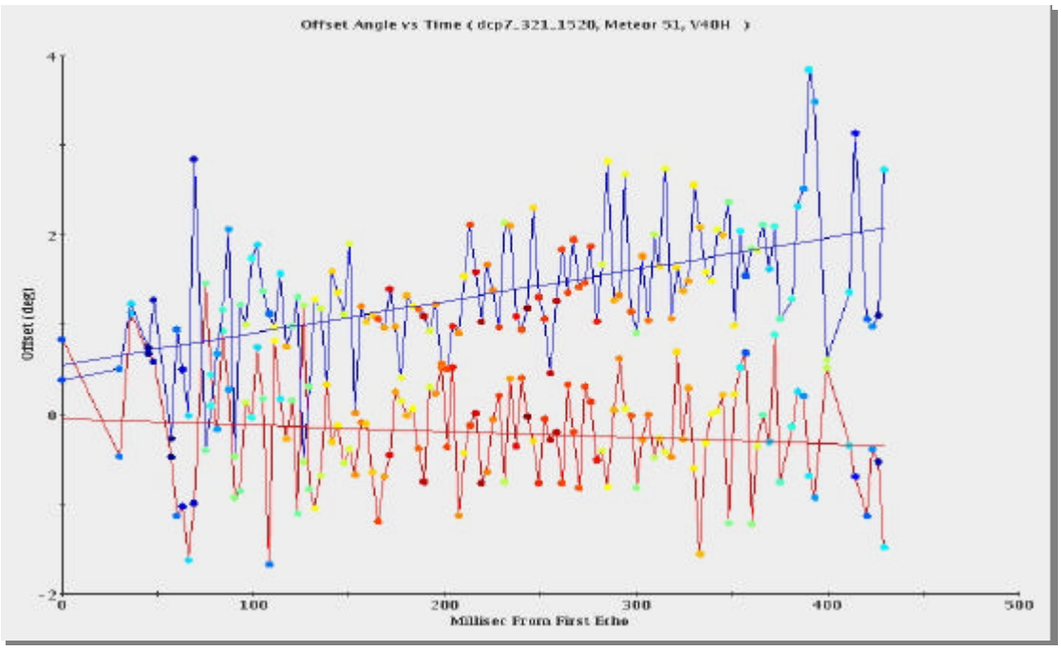

Figure 20. Monopulse Example 2.

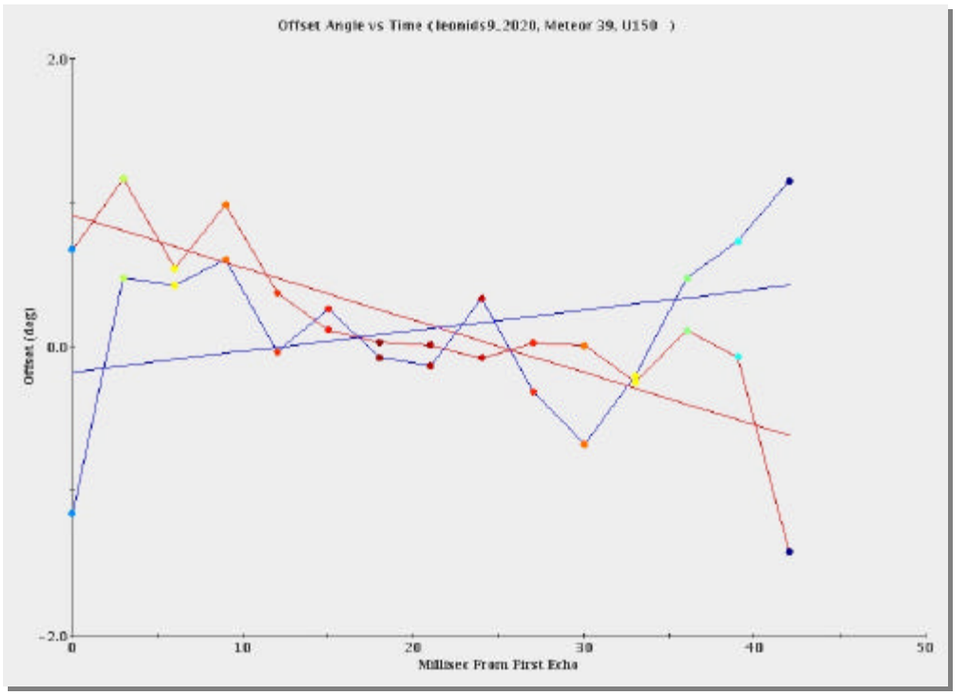

Figure 21. Monopulse Example 3.

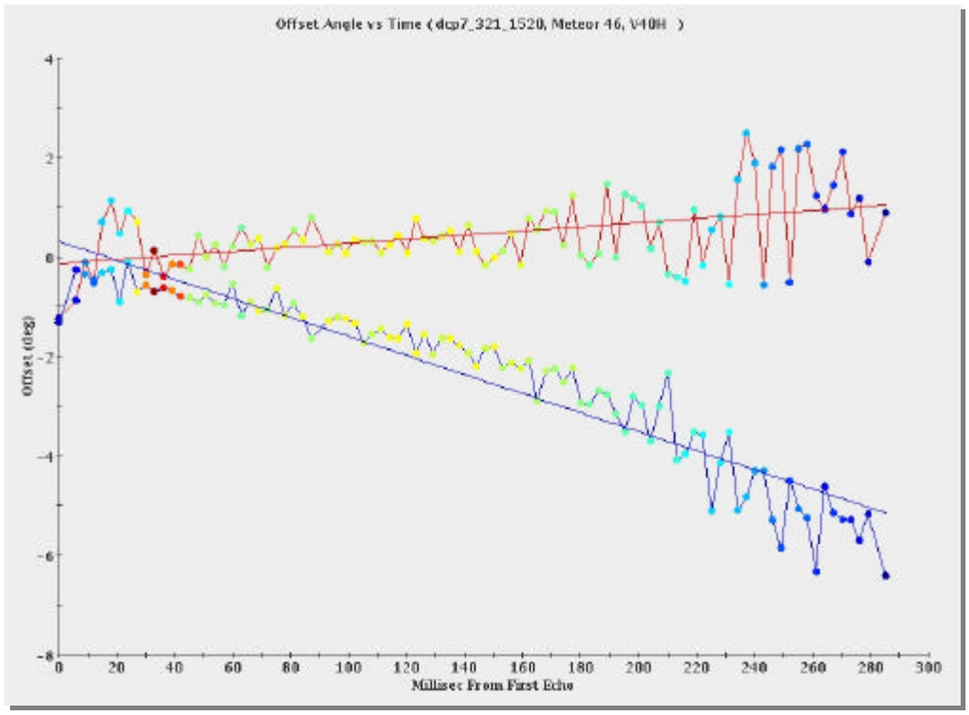

Figure 22. Monopulse Example 4.

In some cases, the profile of the VHF azimuth offset demonstrated a “bow tie” shape where it seems the radar had difficulty determining the sign of the offset for large values. Figure 23 gives an example of this behavior. For the cases where only VHF data was available, only data points with an LC *SNR* of greater than 37dB and an offset magnitude of less than 1.5 degrees were used in the linear fit, if there were at least ten points available satisfying these constraints. Otherwise, we used all available data points.

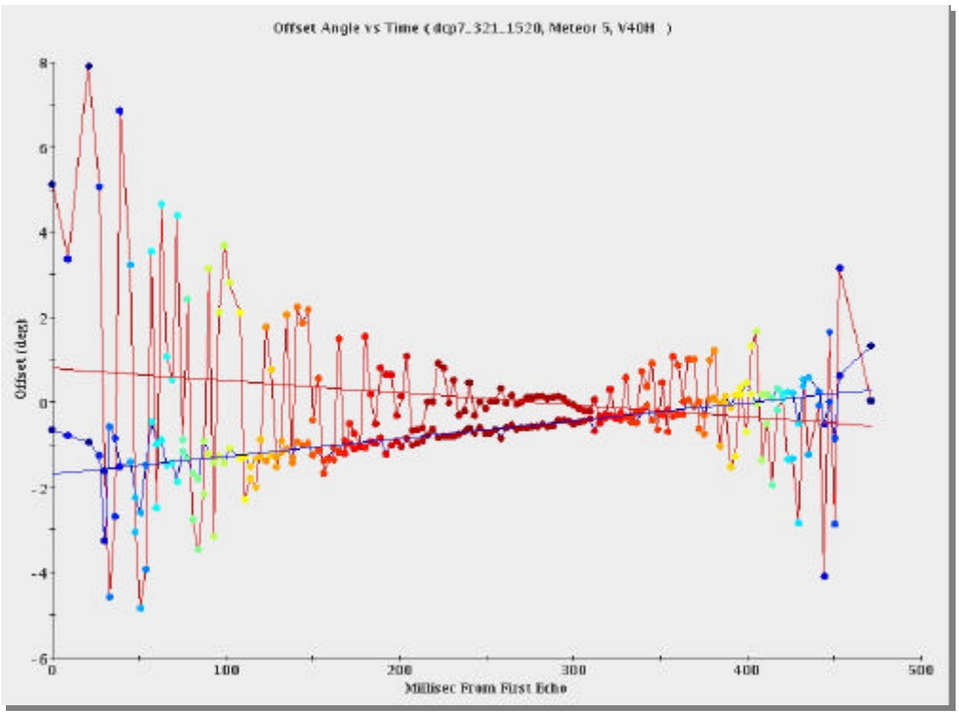

Figure 23. Monopulse VHF Azimuth "Bow Tie" Behavior.

A better solution to the “bow tie” problem was available in dual frequency cases, as shown in Figure 24. Only the VHF azimuth offset data exhibits this anomaly, so for all dual frequency streaks, we created a composite monopulse profile by keeping the UHF azimuth and VHF elevation offset values, as this choice exhibited the best behavior for the majority of cases in both “bow tie” avoidance and smaller root mean square error.

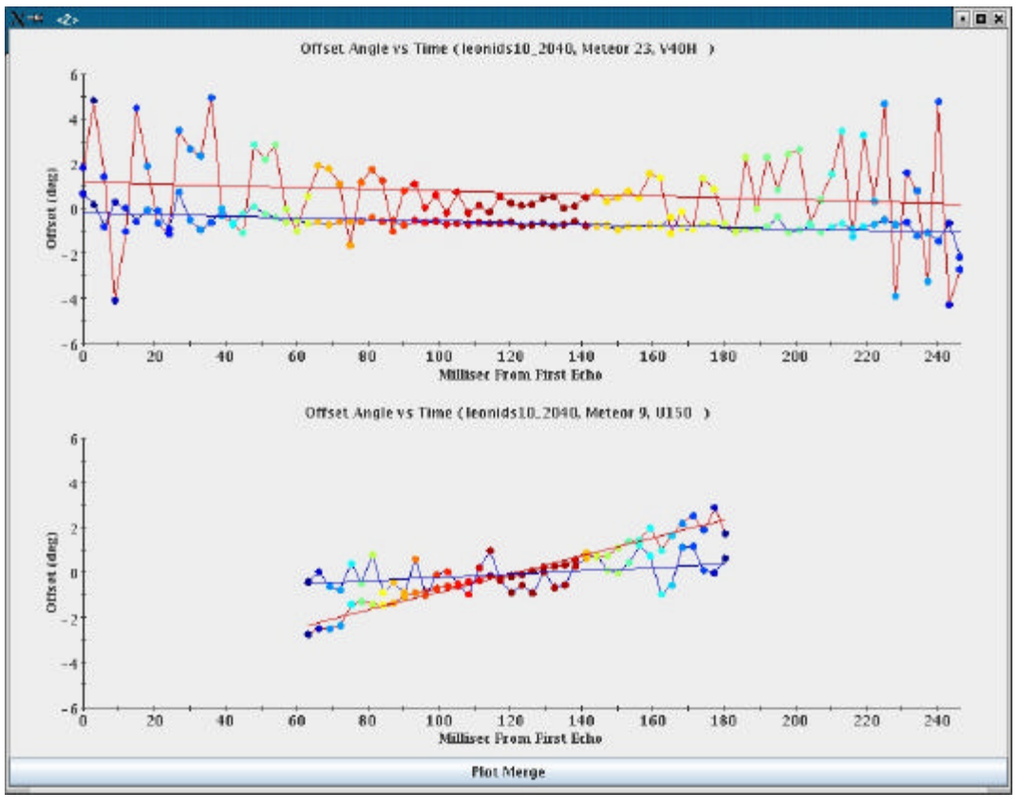

Figure 24. Dual Frequency Monopulse Example.

The linear regression model was then

$$\begin{aligned} ?_{AZ_{fit}} &= ?\, b0_{AZ} + ?\, b1_{AZ}\, t \\ ?_{EL_{fit}} &= ?\, b0_{EL} + ?\, b1_{EL}\, t \end{aligned},$$

using the standard unweighted least squares approach to obtain the estimates of the coefficients as well as the variance of the point estimates. The values of the radar calibration constants (monopulse slope and cross term), which vary by waveform and collection year, are given in Table 12.

Table 12. Monopulse Calibration Constants.

Waveform	Year	s_{EL} *(rad/count)*	x_{EL}	s_{TR} *(rad/count)*	x_{TR}
U150	1998	0.033169	0.002684	0.036194	0.042374
U150	1999	0.032	0.023	0.034	-0.0031
U1000M	1998	0.035057	0.044546	0.039907	0.019419
U1000M	1999	0.035	0.045	0.040	0.019
V40H	1998	0.091224	0.003979	0.059126	-0.206038
V40H	1999	0.10	0.14	0.062	-0.23
V260M	1998	0.091142	0.003974	0.054710	-0.203331
V260M	1999	0.09	0.02	0.055	-0.13

2.3 Reduction Summary

This section provides summary information for the combined UHF/VHF reduction results, beginning with total streak and echo counts in Table 13. Merged echoes belong to streaks tracked in both UHF and VHF. Figure 25 and Figure 26 show the range-rate and altitude distributions; Figure 27 and Figure 28 provide the distributions for elevation and traverse offset. Recalling that the half-power beamwidths are 1.06 and 2.8 degrees for UHF and VHF respectively, the majority of the offset values fall within these ranges for VHF traverse and elevation, and UHF traverse. Figure 29 separates the UHF and VHF elevation offset distributions, suggesting the majority of elevation offset values fall within the half-beamwidth range for UHF as well.

Table 13. Streak and Echo Count Summary.

Total Number of Echoes	42,882
Number of Merged Echoes	10,095
Number of UHF Echoes	5,469
Number of VHF Echoes	37,413
Number of Independent Streaks	2,154
Number of Matched Streaks	200

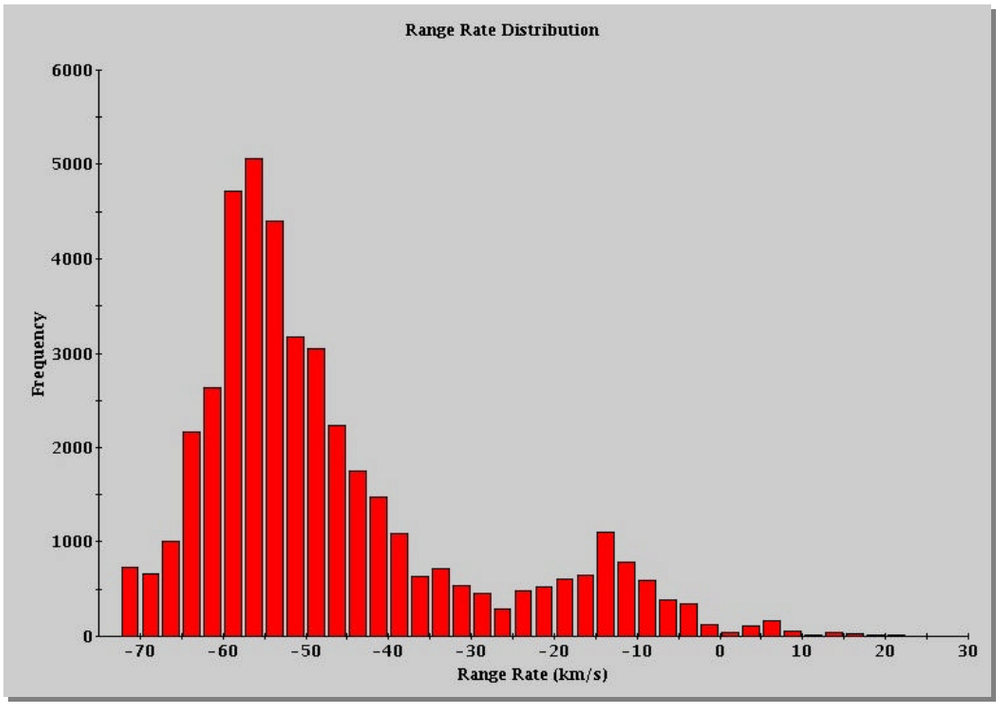

Figure 25. UHF/ VHF Range Rate Distribution.

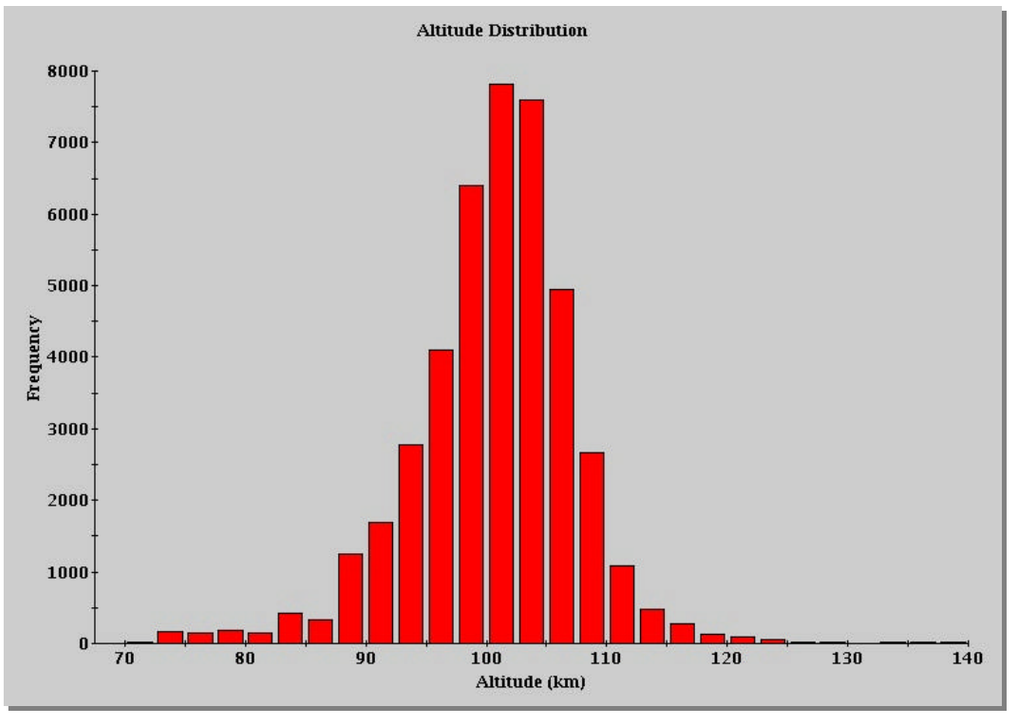

Figure 26. UHF/VHF Altitude Distribution.

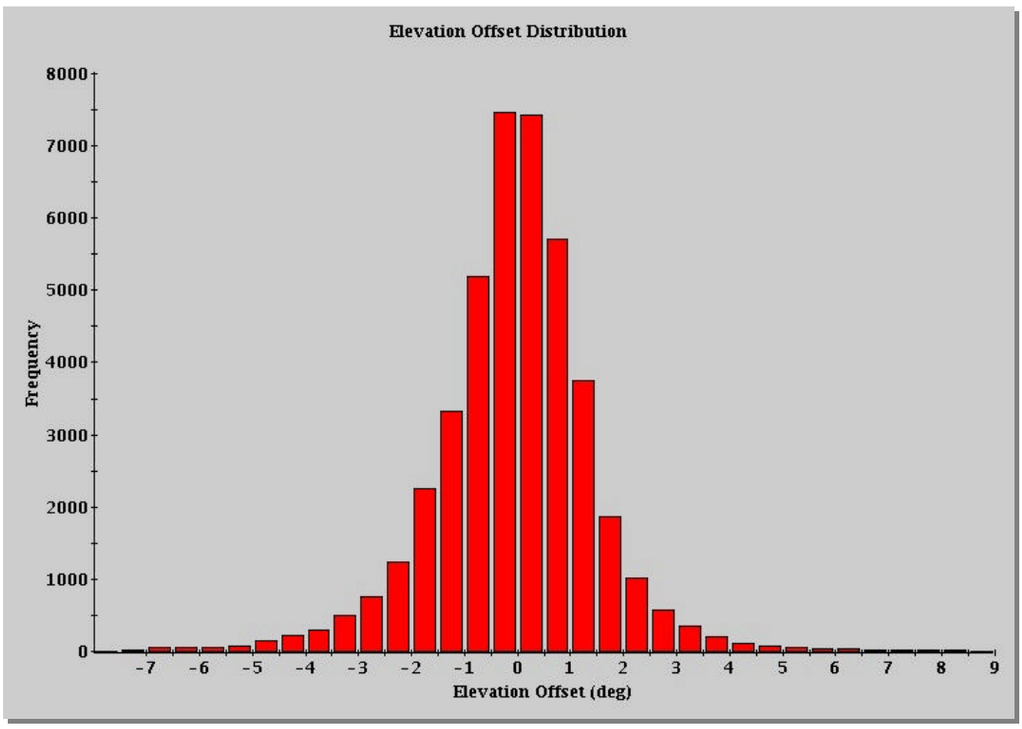

Figure 27. UHF/VHF Elevation Offset Distribution.

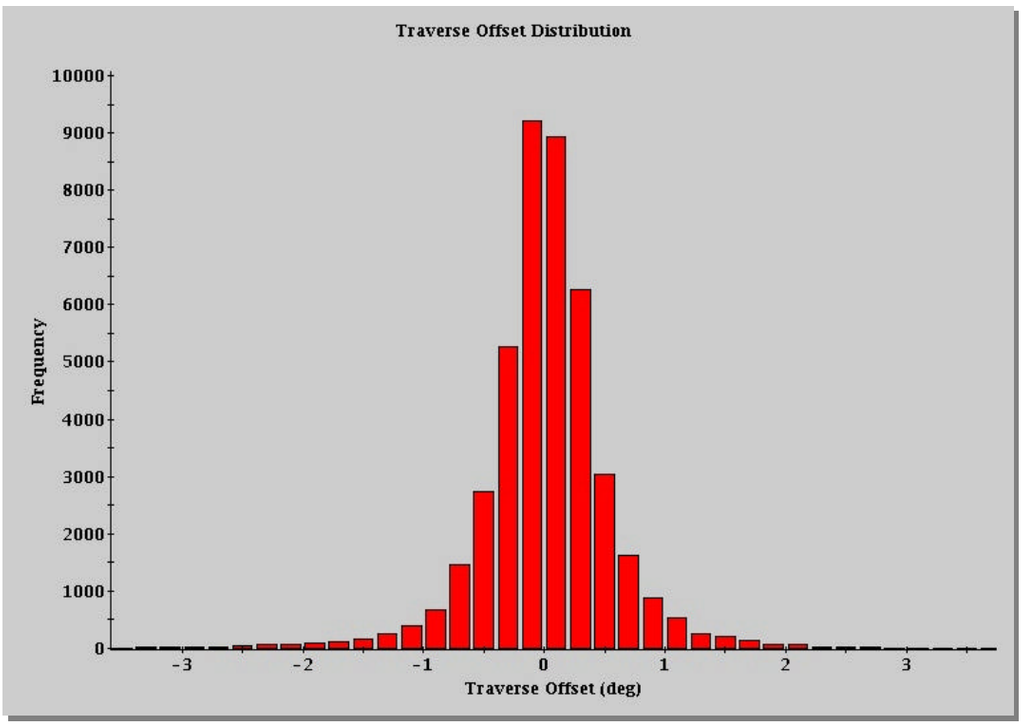

Figure 28. UHF/VHF Traverse Offset Distribution.

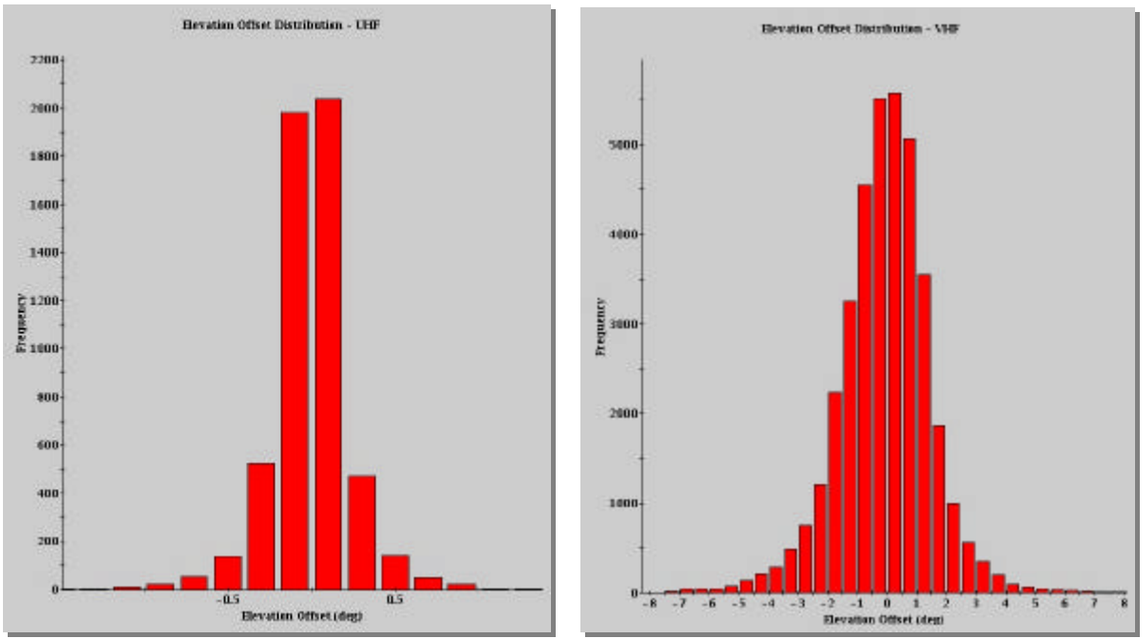

Figure 29. Separate UHF and VHF Elevation Offset Distributions.

2.4 Head Echo Measurements

This section contains a comprehensive description of head echo parameters, which include head echo flux, 3D speed, 3D deceleration, altitude, RCS and polarization ratio.

2.4.1 Flux

We begin our examination of the meteoroid population by determining the meteoroid flux as a function of time of day and position. These data help determine whether the meteoroids we detect are related to the shower, or to the general sporadic population. We examine the Leonid 1998 data to determine flux as a function of time and pointing. We examine the Leonid 1999 data to determine flux as a function of time only. Unfortunately, we cannot determine a change in meteoroid flux as a function of aspect angle or time of day for the Perseid experiment due to the short collection period.

We first examine the Leonid 1998 data. The meteoroid flux while pointing at the Leonid radiant (on-radiant) in 1998 is given in Table 14; Kwajalein local time is 12 hours ahead of GMT, and a dash denotes an unusable data file. The peak VHF detection rate is approximately 0.9 meteoroid per second at 19:40 GMT (no UHF data were recorded at this time), and the peak UHF flux is approximately 1

meteoroid per second at 20:40 GMT. The flux while pointing off-radiant in 1998 is given in Table 15. These data show a peak VHF and UHF flux at 20:20 GMT, with a peak VHF flux of 0.5 and a peak UHF flux of 0.4 meteoroids per second. The peak meteoroid rates using the off-radiant data are smaller than the on-radiant data, but they do occur at approximately the same time (between 19:40 and 20:40 GMT). We note that for most of the 1998 data files, the Leonid radiant aligns with the north apex sporadic meteoroid source.

Table 14. Meteoroid flux, using all of the collected data, as a function of time while pointing at the Leonid radiant (on-radiant) in 1998.

Time (GMT)	VHF Flux (#/second)	UHF Flux (#/second)
15:00	0.29	0.2
18:20	0.5	0.26
18:40	0.48	0.31
19:40	0.88	-
20:40	0.71	1
21:00	0.78	0.22
21:30	0.16	0.02

Table 15. Meteoroid flux, using all of the collected data, as a function of time while pointing away from the Leonid radiant (off-radiant) in 1998.

Time (GMT)	VHF Flux (#/second)	UHF Flux (#/second)
15:15	0.21	0.09
20:20	0.52	0.36
21:18	0.14	0.03

We also examine the Leonid 1999 flux as a function of time of day. Due to viewing location, the Leonid radiant set below the Kwajalein horizon 2 hours before the predicted peak of the storm, which occurred at 02:20 GMT on November 18, 1999. The Leonid 1999 meteor experiment was also shorter in duration than the Leonid 1998 data, and all of the Leonid 1999 data were collected in the on-radiant position. The VHF and UHF flux is given in Table 16. Once again, the Leonid radiant aligns with the north apex sporadic meteoroid source.

Table 16. Meteoroid flux, using all of the data, as a function of time while pointing at the Leonid radiant (on-radiant) in 1999.

Time (GMT)	VHF Flux (#/second)	UHF Flux (#/second)
14:40	0.41	-
14:48	0.27	-
15:04	0.47	-
15:12	0.53	-
15:20	0.43	-
16:50	-	-
16:54	-	0.46
16:58	0.89	0.24
17:06	1.01	0.28

Once again, we note a general increase in meteoroid flux as the time approaches sunrise (18:00 GMT). The VHF data show a more consistent rise, with a peak flux of approximately 1 head echo detected every second at 17:06 GMT. The UHF data show more variation, with a peak flux of approximately 0.5 head echoes per second occurring at 16:54 GMT; the UHF data period lasted only 12 minutes.

2.4.2 3D Speeds

The Kwajalein radars have the capability of determining both head echo range rate, which is the component of the 3D velocity along the radar line-of-sight, as well as the head echo 3D velocity by using the measured monopulse data. The 3D velocity is especially important for determining meteoroid properties such as mass and density, since 3D velocity represents the true measure of the kinetic energy of the meteoroid, not just the component along the radar line-of sight. In this section, we give a brief review of the errors that arise when using this method, and histograms of the 3D speeds derived from each experiment.

While the error on the range rate data is low (typically within a few to tens of meters per second), the monopulse data tends to have higher errors. We attribute these errors to three factors: 1) head echoes have low signal-to-noise ratios relative to those of the large satellites that are typically tracked by the Kwajalein radars and used to calibrate the beam; 2) head echoes are distributed plasmas; this may interfere with the amplitude comparison monopulse method, which is a form of phase interferometry; 3)

most importantly, the monopulse calibration slopes we use to calculate head echo angle from boresite are applicable only in the mainbeam of the radar. Our meteor experiments kept the radar boresite stationary, which allowed head echoes to travel through the entire beam, including side lobes. Therefore, we undoubtedly collected head echoes in the sidelobes, where the calibration constants are not applicable. Further, it is extremely difficult to determine whether a head echo is in the mainbeam or a sidelobe. Although a head echo in a sidelobe would have a much lower signal-to-noise ratio than a head echo in the mainlobe, there is no way to distinguish a large head echo in a sidelobe from a small head echo in the mainlobe. We therefore are unable to calculate reliable 3D velocities for all of the head echo data and instead focus on a subset (approximately 45% to 75%, depending on the experiment and frequency), which we believe are well-behaved, to determine meteoroid properties. We define "well-behaved" as monopulse data that follow a linear trend and do not show an arithmetic jumping between positive and negative angles referred to earlier as a "bow-tie". The total number of detected and well-behaved head echoes is contained in Table 17; the well-behaved head echoes are the only ones utilized for the meteoroid analysis.

Table 17. Head echo statistics for all 3 meteor experiments showing the total number of detected head echoes, and the number of well-behaved head echoes used for the analysis herein.

	# Total Head Echoes		# Well-behaved Head Echoes		
	VHF	**UHF**	**VHF**	**UHF**	**Dual**
Perseid 1998	525	-	239	-	-
Leonid 1998	749	299	451	174	101
Leonid 1999	468	84	223	63	36

An example of well-behaved monopulse data as a function of altitude for a single head echo streak detected at UHF during the Leonid 1998 shower at 21:00 GMT is shown in Figure 30. This plot contains the measured angular offset points for elevation and azimuth in degrees. Lines show the linear fits to the angular offset points; the radar boresite is at 0 degrees. The elevation error varies from 0.04^o at the low and high altitudes, to 0.03^o at 102.5 km altitude. The azimuth error varies from 0.09^o at the low and high altitudes, to 0.04^o at 102.5 km altitude. We consider these data "well-behaved" since the head echo shows a clear track in both azimuth and elevation as a function of altitude during most of its lifetime. However, there are points along this streak that show anomalous behavior, such as the azimuth

data near 100 km where the azimuth appears to be increasing almost in an exponential-manner. If this type of behavior is seen along the entire head echo streak, we would tag this head echo as "ill-behaved" and discard it.

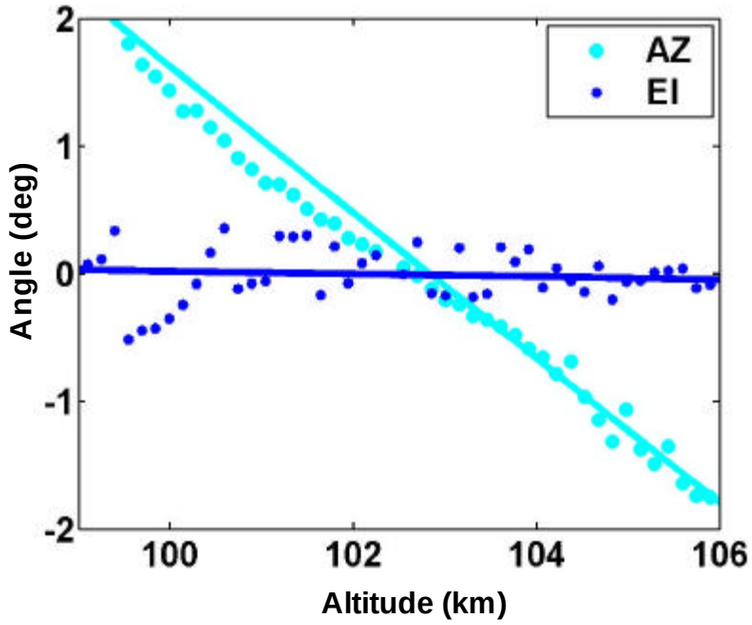

Figure 30. Monopulse angular offset for a single head echo detected during the Leonid 1998 shower, where 0° is ALTAIR boresite. The lines represent the linear fits to the measured points.

We utilize the data shown in Figure 30 to calculate the head echo's 3D position, velocity, and deceleration. The 3D speed data are shown in Figure 31 along with the measured range rate, which is just the difference in range with respect to time; recall that we apply an exponential fit to the range data. The range rate error, which is simply a measure of the variance of the data, changes from 5.6 m/s at 106 km, to 1.4 km/s at 101 km altitude. The altitude extent of the 3D speed differs from the altitude extent of the range rate data because typically we use the range and boresite elevation angle to calculate altitude. By using the monopulse data, we can add the elevation offset to the boresite elevation angle to calculate a more accurate altitude. The 3D speed in Figure 31 is almost 6 km/s faster than the range rate. Note that both 3D speed and range rate decrease as altitude decreases, which demonstrates the head echo's deceleration.

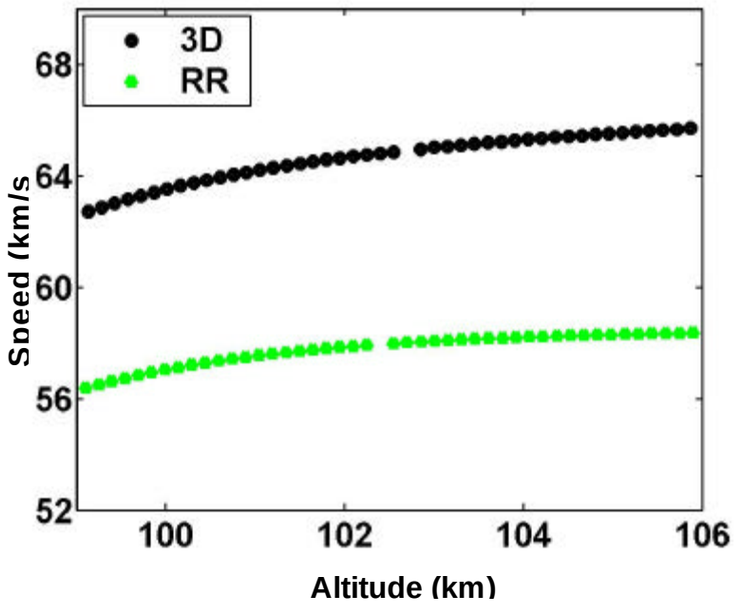

Figure 31. Speed vs. altitude for a single UHF head echo corresponding to the Leonid 1998 data shown in Figure 2. The range rate is the difference in the measured range, whereas the 3D speed is the range rate corrected using the monopulse data.

We next examine 20 head echoes detected at VHF during the Leonid 1998 shower, which all show a marked deceleration. These data are plotted as a function of altitude in Figure 32, which displays the measured range rate as well as the 3D speed. Using these data, we find that the 3D speed of each head echo is always faster than the corresponding range rate, as expected. The smallest difference between range rate and 3D speed is 0.2 km/s, and the largest difference is 17.8 km/s. These data show the need and importance of using the monopulse data to determine the true head echo's speed, not just the speed along the radial direction. A difference in speed of 17.8 km/s between the 3D speed and the range rate can amount to a factor of 2 difference in the meteoroid's kinetic energy.

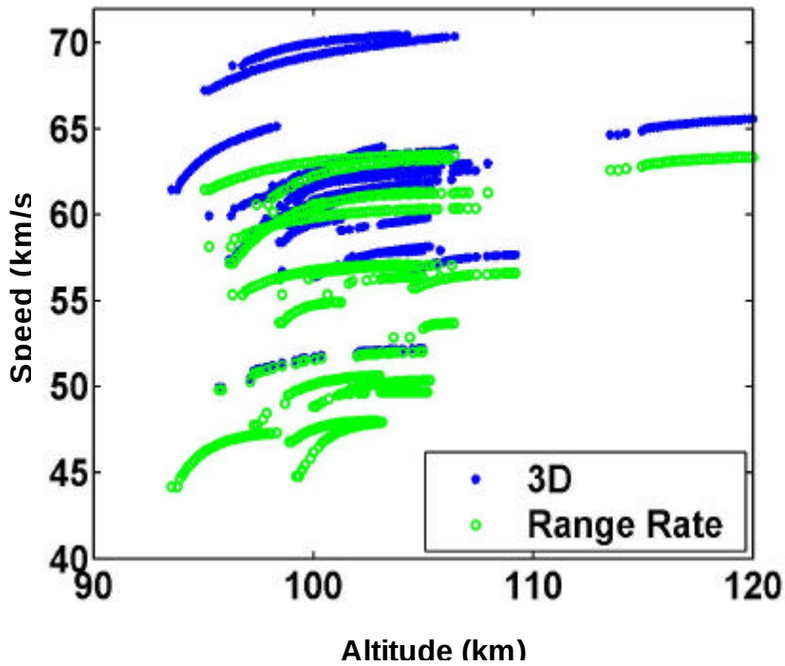

Figure 32. Speed as a function of altitude for 20 VHF head echoes detected during the Leonid 1998 shower, showing range rate and 3D speed.

Finally, we examine the difference between range rate and 3D speed for all of the well-behaved VHF data contained in the Perseid 1998, Leonid 1998 and Leonid 1999 showers. The mean difference between range rate and 3D speed during the Perseid 1998 shower is 22.8 km/s; specifically, the range rates vary from 4 km/s to 57 km/s, while the 3D speeds vary from 16 km/s to 101 km/s. During the Leonid 1998 shower, the mean difference between the measured VHF range rate and 3D speed is 11.8 km/s, while the mean difference during the Leonid 1999 shower at VHF is 14.3 km/s. The Leonid 1998 shower has well-behaved range rates between 7 km/s and 70 km/s, and well-behaved 3D speeds between 12 and 132 km/s. The Leonid 1999 shower has well-behaved range rates between 2 km/s and 70 km/s, while the well-behaved 3D speeds are between 11 km/s and 111 km/s.

We extract the maximum 3D speed from 239 Perseid VHF head echoes. Speed typically decreases as altitude decreases, so the maximum speed from each head echo is usually equivalent to the meteoroid's speed prior to a significant amount of atmospheric deceleration, or said differently, the first detected pulse along an entire ionization streak. The maximum speeds, in histogram format, from 239

Perseid 1998 head echoes are plotted in Figure 33. The mean and median speeds from this histogram are 59 km/s and 60 km/s.

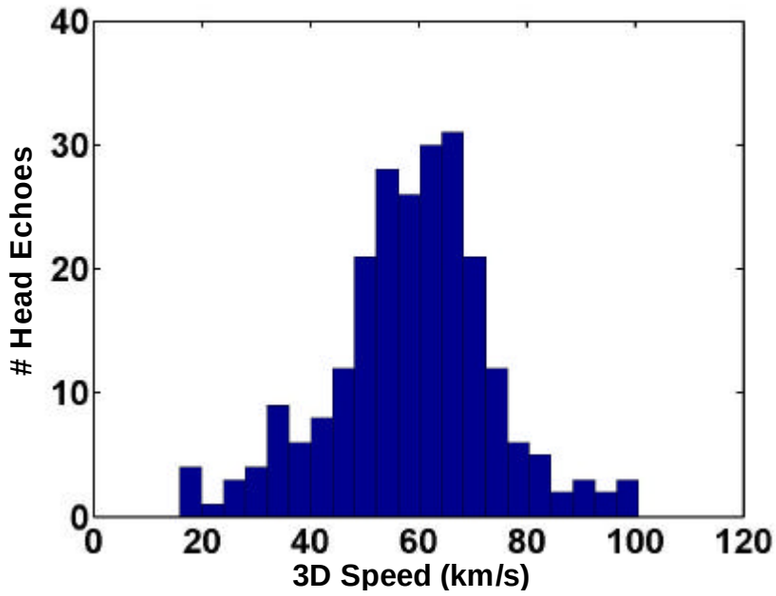

Figure 33. 3D speed histogram from the Perseid 1998 shower, which includes 239 VHF head echoes.

Next, we examine the maximum 3D speeds from the Leonid 1998 shower. The maximum range rates from 451 VHF and 174 UHF Leonid 1998 head echoes are plotted in Figure 34. The mean and median speeds from the VHF data are both 61 km/s. The mean and median speeds from the UHF data are 60 km/s and 61 km/s, respectively.

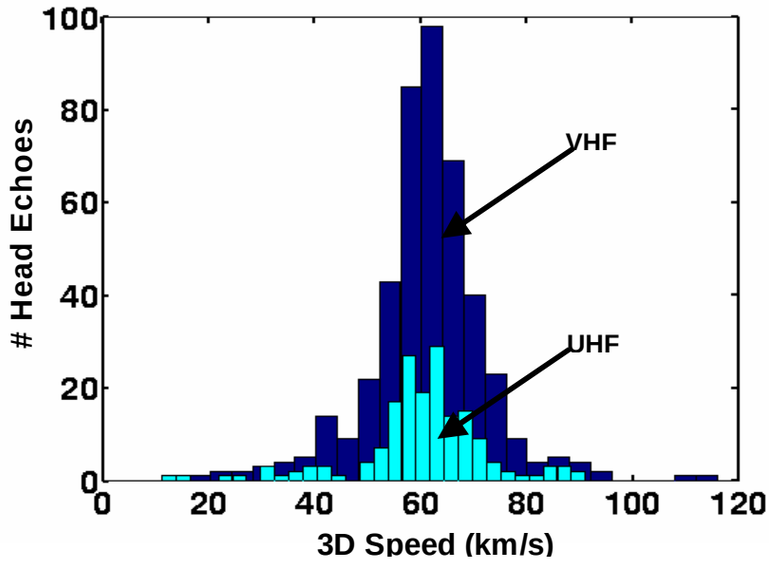

Figure 34. 3D speed histograms from the Leonid 1998 shower, which includes 451 VHF and 174 UHF head echoes.

The maximum 3D speeds from 223 VHF and 63 UHF Leonid 1999 head echoes are plotted in Figure 35. The mean and median VHF speeds are both 62 km/s, and the mean and median UHF speeds are 64 km/s and 61 km/s, respectively.

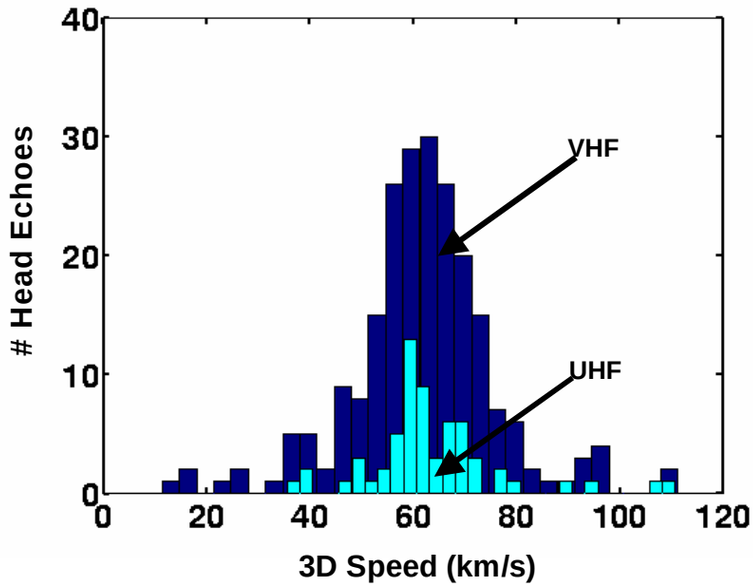

Figure 35. 3D speed histograms from the Leonid 1999 shower, which includes 223 VHF and 63 UHF head echoes.

As a final check to determine whether our monopulse, and hence 3D speed data, follow our physical intuition, we plot the duration of each head echo as a function of its aspect angle relative to ALTAIR boresite. Intuitively, we believe that longer-enduring head echoes should have smaller aspect angles, since a large aspect angle would preclude a lengthy detection. These data are contained in Figure 36 and do indeed follow this trend. The large amount of scatter seen at short durations reflects the idea that short durations can be attributed to either a large aspect angle, or to the meteoroid disintegrating while in the beam.

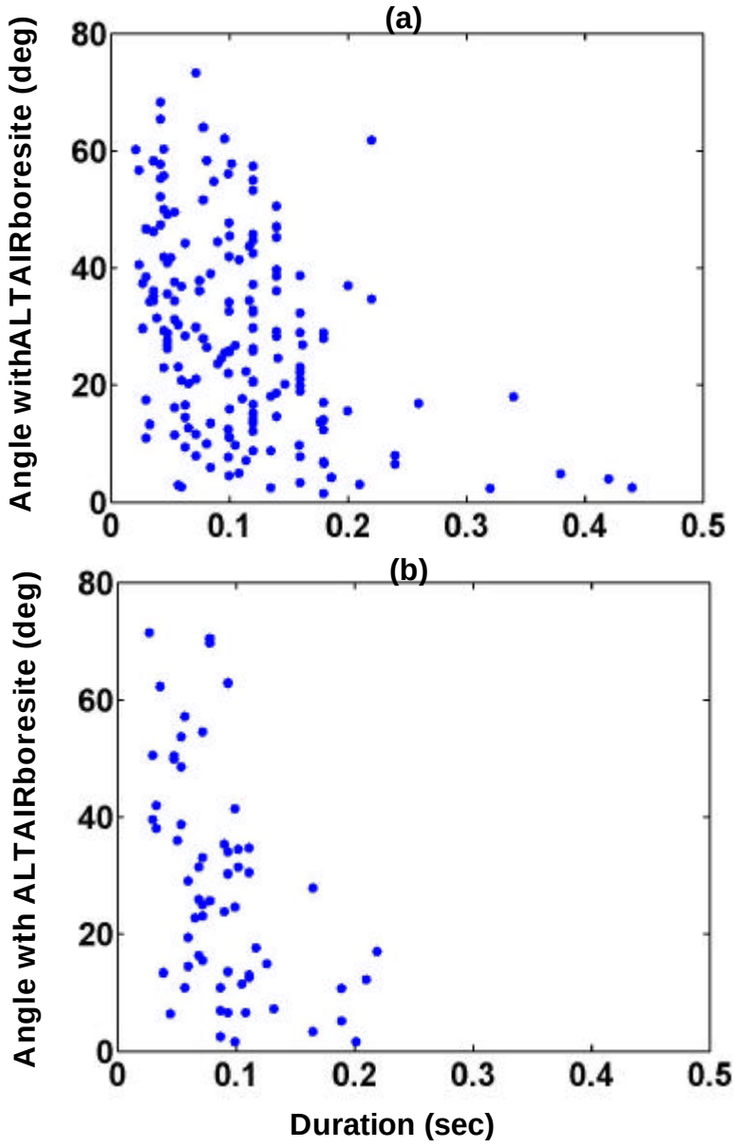

Figure 36. Duration vs. angle with boresite for UHF data collected during the (a) Leonid 1998 shower and (b) Leonid 1999 shower.

2.4.3 Deceleration

Head echo deceleration results from the interaction of a meteoroid with the background atmosphere. Head echo decelerations are proportional to the atmospheric drag and inversely proportional to the meteoroid mass. Therefore, decelerations are most pronounced for very small meteoroids and should increase as altitude decreases as a meteoroid loses mass.

We begin by extracting the maximum deceleration from each head echo streak, so that each deceleration corresponds to a single, and separate, meteoroid. The maximum deceleration from a head echo typically occurs when the head echo is at or near its lowest detected altitude, since deceleration should theoretically increase as atmospheric density increases. The maximum decelerations from 239 Perseid 1998 VHF head echoes are plotted in Figure 37. The minimum, median, and maximum VHF decelerations from this shower are 0.4 km/s^2, 7.6 km/s^2, and 24.3 km/s^2, respectively.

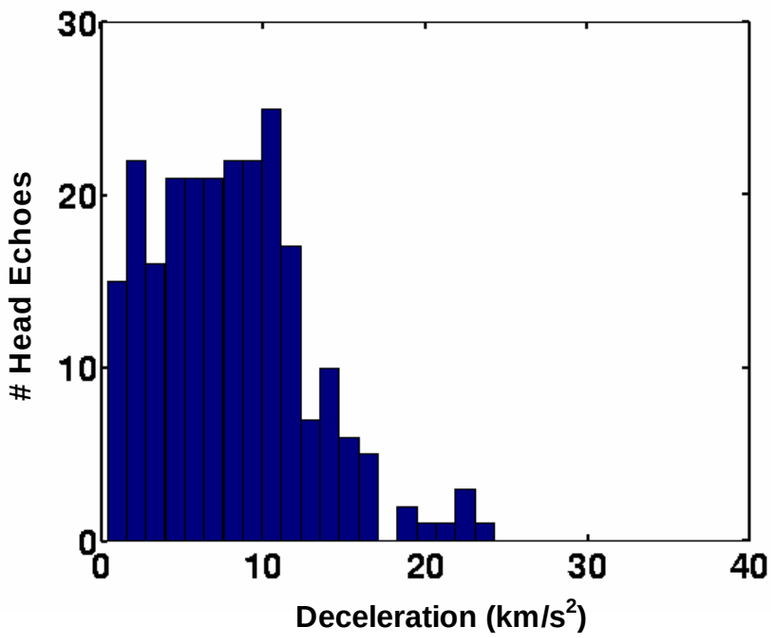

Figure 37. Deceleration histogram for the Perseid 1998 shower, which shows the maximum deceleration from each of the 239 VHF head echoes.

The maximum decelerations from 451 VHF and 174 UHF Leonid 1998 head echoes are plotted in Figure 38. The minimum, median, and maximum VHF decelerations from this shower are 0 km/s^2,

5.2 km/s^2, and 124.8 km/s^2, respectively. The minimum, median, and maximum VHF decelerations from this shower are 0 km/s^2, 5.9 km/s^2, and 38.2 km/s^2, respectively.

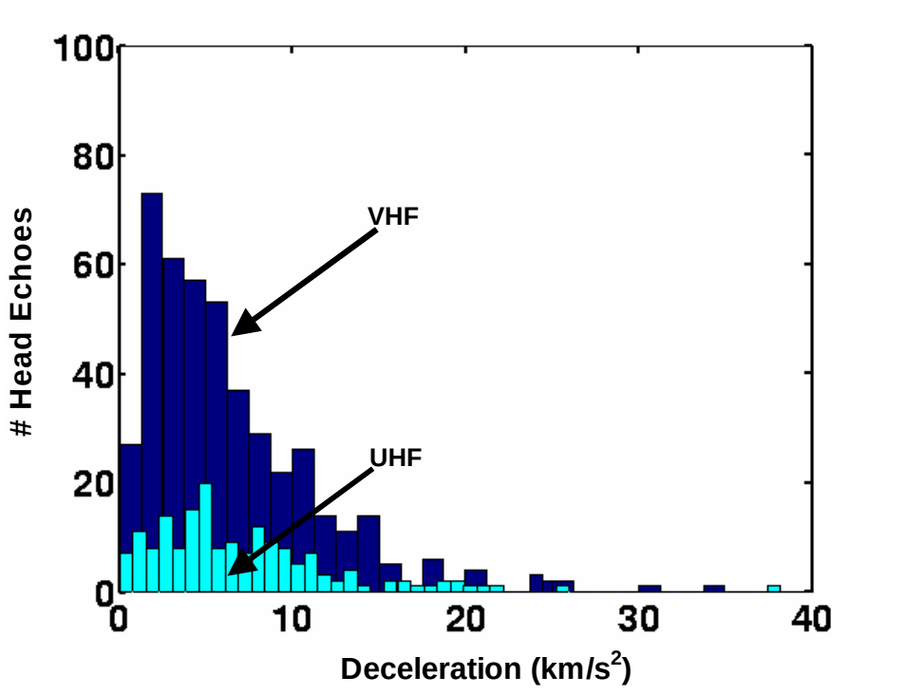

Figure 38. Deceleration histogram for the Leonid 1998 shower, which shows the maximum deceleration from each of the 451 VHF and 174 UHF head echoes.

The maximum decelerations from 223 VHF and 63 UHF Leonid 1999 head echoes are plotted in Figure 39. The minimum, median, and maximum VHF decelerations from this shower are 0 km/s^2, 3.1 km/s^2, and 24.3 km/s^2, respectively. The minimum, median, and maximum VHF decelerations from this shower are 0 km/s^2, 5.9 km/s^2, and 38.2 km/s^2, respectively.

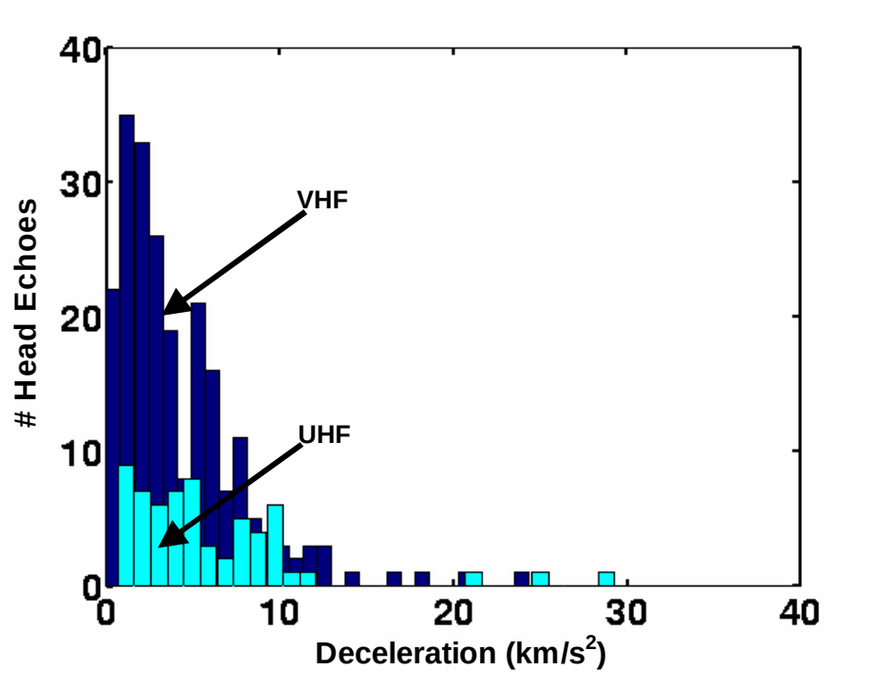

Figure 39. Deceleration histogram for the Leonid 1999 shower, which shows the maximum deceleration from each of the 223 VHF and 63 UHF head echoes.

2.4.4 Altitude

Head echoes detected using all available large-aperture, high-power radar data show altitude distributions that span 70 to 140 km altitude. This altitude dependence is clearly indicative of a meteoroid's interaction with the atmospheric neutral molecules. However, since a head echo is the reflection from meteoroid plasma, head echo detection altitude depends upon a meteoroid's physical parameters such as its size, mass and speed, as well as on plasma and radar detection criteria.

We begin by examining 239 VHF head echoes detected during the Perseid 1998 shower in order to determine the general altitude distribution at VHF; again the Perseid 1998 shower data was collected using only VHF. A histogram of the maximum altitude from each head echo collected during the Perseid shower is contained in Figure 40.

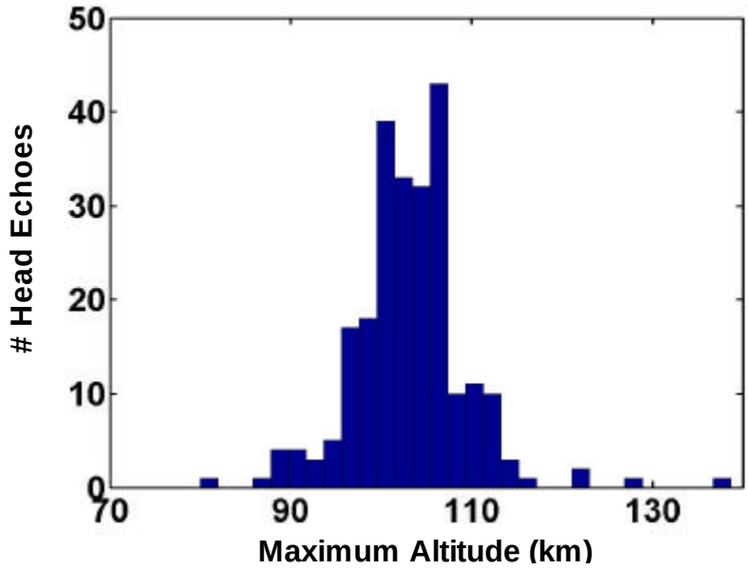

Figure 40. Histogram of the Perseid 1998 data showing the maximum altitude from each of the 239 VHF detected head echoes.

We also examine 451 VHF and 174 UHF head echoes detected during the Leonid 1998 shower and choose the maximum altitude of each head echo. These data are contained in Figure 41.

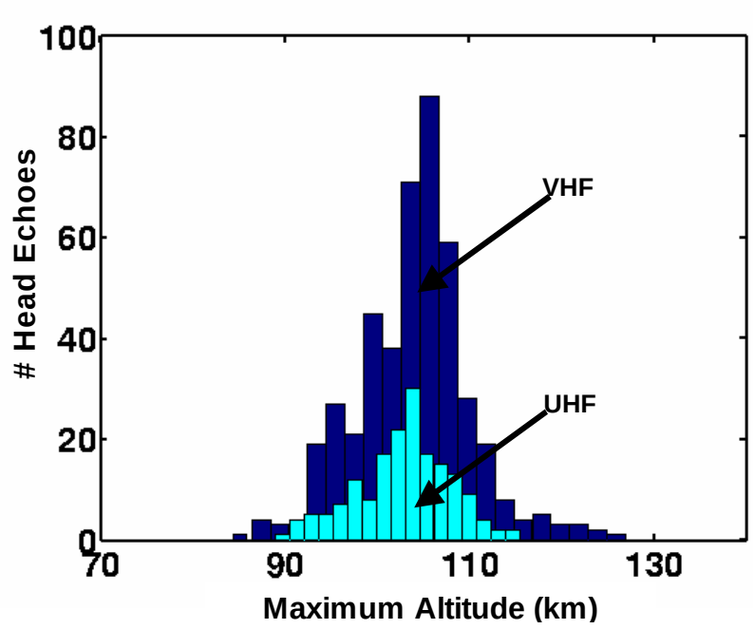

Figure 41. Histograms of the Leonid 1998 data showing the maximum altitude from each of the 451 VHF and 174 UHF detected head echoes.

We examine 223 VHF and 63 UHF head echoes detected during the Leonid 1999 shower and again calculate the maximum altitude of each head echo. The altitude histogram for the Leonid 1999 data is contained in Figure 42. Note that the Leonid 1999 data shows the highest altitude distributions from all three experiments.

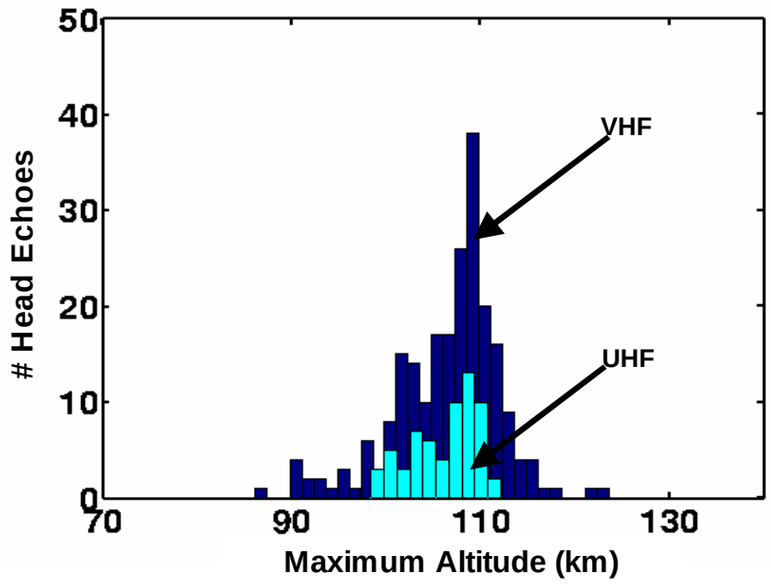

Figure 42. Histograms of the Leonid 1999 data showing the maximum altitude from each of the 223 VHF and 63 UHF detected head echoes.

We examine the relationship between head echo detection altitude and 3D speed using the VHF head echo data collected during the Leonid 1998 experiment. For each head echo, we extract its maximum speed and the maximum detection altitude. Next, we group these values into 1-km altitude bins, and subsequently calculate the mean speed in each altitude bin and plot these as a function of the mean altitude bin. We choose to plot the data in this fashion since we detect meteoroids with a wide range of masses and speeds. The variability in speed and meteoroid mass produces a more cluttered plot.

The maximum 3D speeds and altitudes from 451 VHF Leonid 1998 head echoes, binned into 1-km altitude bins, are plotted in Figure 43. We see that as altitude increases, head echo speed increases. The line represents the linear fit to the data and has a slope of .6986.

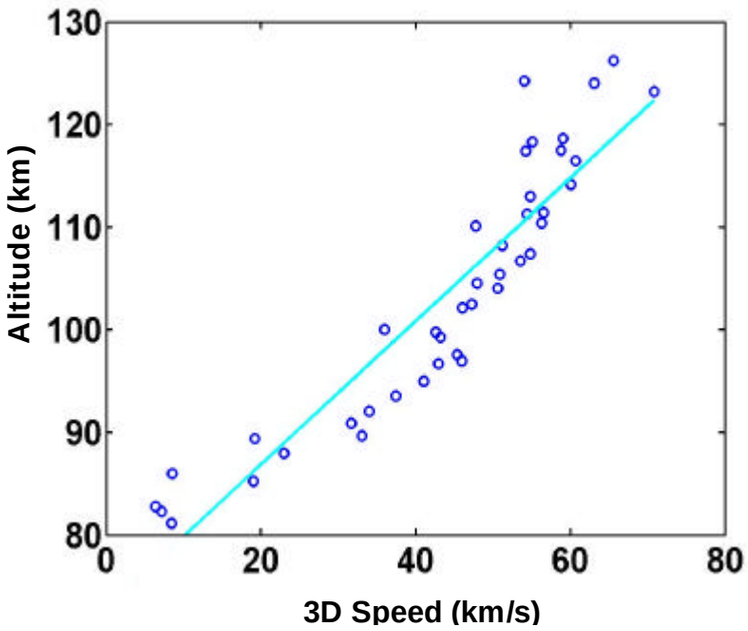

Figure 43. Maximum 3D speed as a function of maximum detection altitude using 451 well-behaved VHF head echoes detected during the Leonid 1998 shower.

Simple arguments about the nature of meteoroid ablation, atmospheric density, and head echo detection explain the dependence of speed on altitude. Meteoroid ionization rates are proportional to speed, therefore fast meteoroids will disintegrate sooner (i.e. at higher altitudes) than slow meteoroids. In addition, only the fastest meteoroids will have sufficiently high ionization rates to create plasmas detectable by radar at high altitudes where the atmospheric mean free path is large. Meteoroids penetrating deeper into the atmosphere encounter an exponentially increasing neutral density. Higher neutral densities may produce head echoes with higher plasma densities, which allows for the detection of slower (i.e. low altitude) meteoroids. Since head echo plasma production depends on both meteoroid speed and mass, radars will preferentially detect fast-moving meteoroids of a particular mass. Therefore, it is highly likely that our head echo data are preferentially detecting the faster-moving meteoroids and may not be detecting the slower meteoroid population.

2.4.5 Radar Cross Section (RCS)

The radar-cross-section (RCS) of a target is defined as the projected area that would be required to intercept, and radiate isotropically, the same power as the target radiates toward the radar receiver

[*Knott,* 1985]. In other words, the power scattered by a target is expressed as the product of an effective area and an incident power density. The radar target can be considered a "point scatterer" if the distance to the target is much larger than the dimensions of the target. In general, RCS (*?*) is not a constant.

We begin by defining the power intercepted by the target (i.e. head echo), as P_i, as

$$P_i \; ? \; \frac{P_t G_t ?}{4? R^2} \qquad \textbf{Eq. 1}$$

where P_t is the power output from the radar transmitter, G_t is the peak transmitter gain of the radar antenna and R is the distance to the target. We approach the problem as if the target intercepts P_i and radiates it isotropically, such that the power density at the radar receiver, P_d, is

$$P_d \; ? \; \frac{P_t G_t ?}{(4? \;)^2 R^4} \qquad \textbf{Eq. 2}$$

The power received by the radar is the power density times the effective capture area of the antenna, or in terms of antenna gain and capture area, A_c,

$$A_c \; ? \; \frac{G_r ?^2}{4?} \qquad \textbf{Eq. 3}$$

where G_r is the peak receiver gain and ? is the radar wavelength. Since $G_r = G_r = G_r$, the received power P_r becomes

$$P_r \; ? \; \frac{P_t G^2 ?^2 s}{(4p)^3 R^4} \qquad \textbf{Eq. 4}$$

This is the classical form of the radar range equation.

By using the SNR measurement, as well as the ALTAIR calibration constant, we can simplify the radar range equation and define the RCS of a head echo as

$$? \; _{meas} \; ? \; \frac{R^4 (SNR) C}{P_t} \qquad \textbf{Eq. 5}$$

where C is the radar calibration constant. The calibration constant is embedded in the ALTAIR system files and contains the Boltzmann constant, bandwidth, system noise temperature, antenna gain and radar wavelength. The RCS is always given relative to a metallic sphere with an area of 1 m^2. Thus a target with a 0 decibel-relative-to-a-square-meter (dBsm) is equivalent to the return from a 1 m^2 sphere. We

justify using the point scattering equation (Eq. 5) by citing both ALTAIR measurements of head echoes, as well as other high-power radar detections of head echoes. Head echoes are always contained within one pulse (typically 0.003 seconds) and do not extend in range and time, unlike specular and non-specular trails.

To illustrate a typical range of VHF LC RCS values associated with head echoes, we include the VHF LC RCS histogram from the Perseid 1998 shower. This plot, shown in Figure 44, is obtained by choosing the maximum RCS from each of the 239 detected head echoes. The mean and median RCS values are -27 dBsm and -28 dBsm, respectively. Unlike 3D speed, which is largest at the beginning of a head echo streak, or deceleration, which is usually largest at the end of a head echo streak, the largest LC RCS from each head echo streak does not necessarily occur at any particular point along the head echo. This illustrates the difficulty in characterizing head echo LC RCS, which undoubtedly depends upon both the head echo plasma characteristics, as well as the head echo position within the mainbeam of the radar. Specifically, the SNR of a target falls as you track, or detect, the target beyond the center of the mainbeam. As a target moves from the center of mainbeam of the radar towards the sidelobes, the SNR falls by approximately 30 dB. Therefore, a variation in measured RCS can arise from either the characteristics of the plasma, or the characteristics of the radar beam.

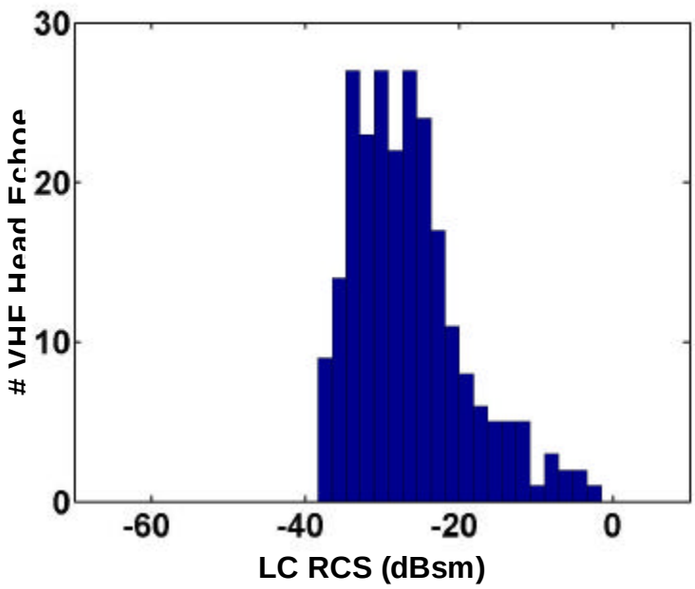

Figure 44. Maximum LC RCS extracted from each of the 239 VHF head echoes detected during the Perseid 1998 shower.

Head echo radar data show that as radar frequency increases, head echo RCS, including both LC and RC RCS, decreases. This is an expected result, since head echoes are plasmas and signal returns from plasmas decrease as radar frequency increases. Simply stated, this frequency dependence results from there being fewer electrons contained within a UHF wavelength relative to a VHF wavelength. To minimize the amount of figures, we examine only the LC RCS of each head echo, since the majority of head echoes have much higher LC signal returns relative to RC signal returns; we explore this phenomenon in the next sub-section. As an aside, we see the same frequency dependence and trends in the RC RCS data as well.

We examine the maximum LC RCS extracted from each of the 451 VHF and 174 UHF head echoes detected during the Leonid 1998 shower. These data are contained in Figure 45. The mean and median VHF LC RCS values are -27 dBsm and -28 dBsm, respectively. The mean and median UHF LC RCS values are -49 dBsm and -51 dBsm, respectively. The minimum LC RCS values at both VHF and UHF simply indicate the minimum sensitivity of the system. The median and maximum LC RCS values, however, clearly show the frequency dependence, where the median LC RCS values are approximately 23 dBsm stronger at VHF than at UHF. Recall that 23 dBsm corresponds to a difference of 1.99×10^2 m^2 in the LC data. We also examine the simultaneous detections, which total 101. The minimum difference between VHF and UHF RCS is 12 dBsm, and the maximum difference is 39 dBsm.

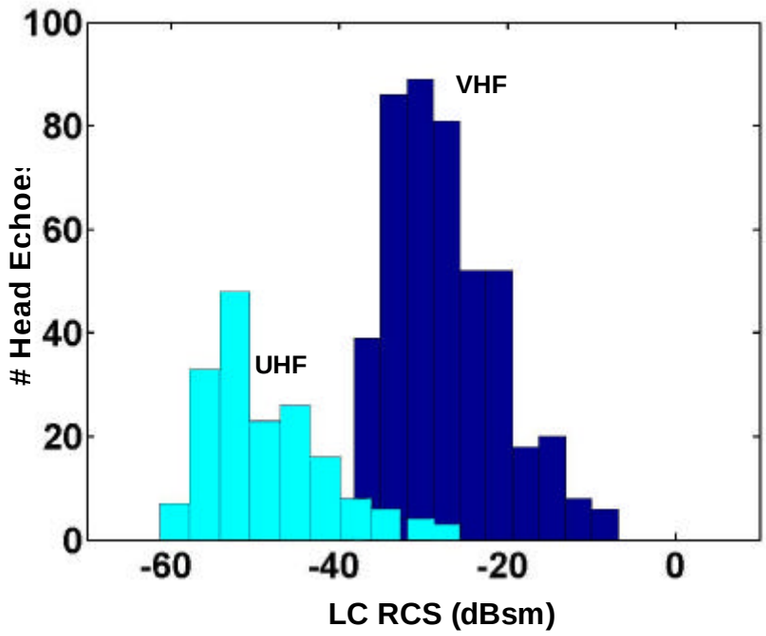

Figure 45. Maximum LC RCS extracted from each of the 451 VHF and 174 UHF head echoes that we processed from the Leonid 1998 shower. The higher frequency (VHF) head echoes always have a higher RCS.

We examine the maximum LC RCS from each of the 223 VHF and 63 UHF head echoes detected during the Leonid 1999 shower. These data are contained in Figure 46. The mean and median VHF LC RCS values are both -21 dBsm. The mean and median UHF LC RCS values are -48 dBsm and -49 dBsm, respectively. The minimum LC RCS values at both VHF and UHF again indicate the minimum sensitivity of the system, while the median and maximum LC RCS values clearly show the frequency dependence. The head echoes are approximately 28 dBsm stronger at VHF than at UHF. We also examine the simultaneous detections, which total 36. The minimum difference between VHF and UHF RCS is 18 dBsm, and the maximum difference is 34 dBsm.

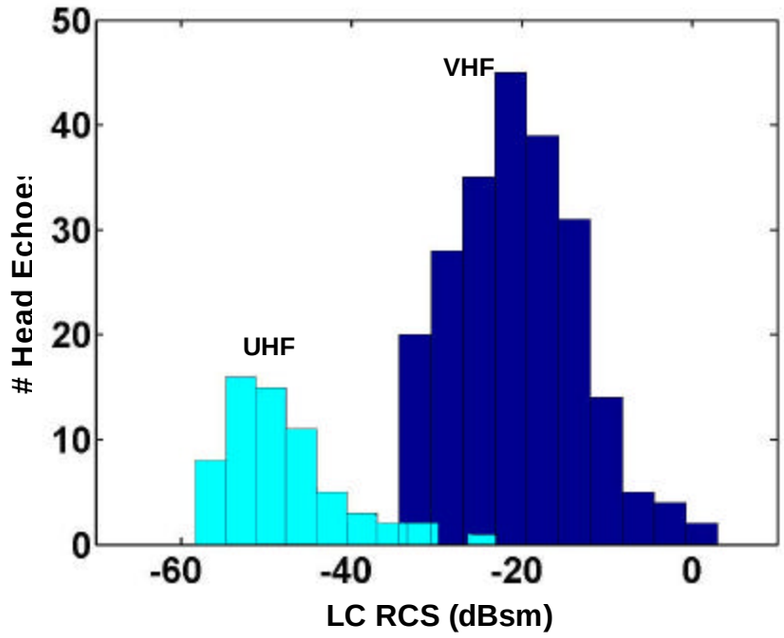

Figure 46. Maximum LC RCS extracted from each of the 223 VHF and 63 UHF head echoes that we processed from the Leonid 1999 shower. The higher frequency (VHF) head echoes always have a higher RCS.

As a final comparison, we examine a head echo detected simultaneously at three frequencies during the Leonid 1998 shower using both the ALTAIR and TRADEX radars. The maximum VHF head echo LC RCS is -10.6 dBsm at 95.75 altitude, the maximum UHF LC RCS is -25.8 dBsm at 95.59 km, and the maximum L-band LC RCS is -36 dBsm at 95.58 km. Note that RCS decreases with increasing frequency, and that the altitude of maximum detected RCS decreases as radar frequency increases.

On average, the VHF detections show RCS values that are 20-30 dBsm higher than the UHF RCS values [*Close et al*., 2002]. These values are consistent with *Mathews et al.* [1997] and *Zhou et al.* [1998]. Head echoes measured by ALTAIR appear most commonly as single frequency VHF measurements and, less frequently, as single frequency UHF and two-frequency detections; *Zhou et al.* [1998] also reports this result.

We believe that single-frequency UHF head echoes result from the minimum sensitivity of the VHF waveform (typically -45 dBsm after accounting for the noise threshold), since the UHF waveform is more sensitive than the VHF waveform. We examine the mean and maximum LC RCS values of the single and dual-frequency UHF detections to confirm this idea using the 101 simultaneous head echoes contained in the Leonid 1998 data set. The dual-frequency UHF detections have LC RCS values between -25 dBsm and -61 dBsm with a mean of -47 dBsm, however the single-frequency UHF detections have lower LC RCS values that range from -36 to -60 dBsm with a mean of -50 dBsm. The minimum UHF LC RCS values reflect the minimum sensitivity of the UHF system; however, the mean of the dual-frequency UHF detections is 3 dBsm higher than the dual-frequency detections, and the maximum of the dual-frequency UHF detections is 11 dBsm higher. This evidence suggests that the minimum detectable VHF LC RCS is the likely cause of the single-frequency UHF detections.

The single-frequency VHF head echo LC RCS values do not show a difference in RCS relative to the dual-frequency detections. The single frequency VHF detections have LC RCS values between -7 dBsm and -38 dBsm with a mean of -28 dBsm. The dual-frequency VHF detections range from -7 dBsm to -38 dBsm with a mean of -27 dBsm. There is a difference in the altitude distribution, however. The single-frequency VHF head echoes have altitudes between 86 km and 130 km, whereas the dual-frequency VHF detections have altitudes spanning 93 km to 116 km. This is a direct result from the smaller sampling window we used with the U150 waveform, which spanned altitudes between 90 and 110 km at UHF; recall that the altitude window was 70 to 140 km at VHF. In addition, there is a difference in the speed distribution. The single-frequency VHF head echoes have speeds between 12 km/s and 112 km/s, whereas the dual-frequency VHF detections have speeds from 32 km/s to 92 km/s. The difference in the speed distribution results from the dependence between speed and altitude, where head echo speed is proportional to head echo. As noted earlier, we detect high-speed head echoes at high altitudes where the atmospheric density is small; high ionization efficiencies, associated with high-speed head echoes, are needed in order to ionize the atmosphere at these high altitudes. Therefore, the single-frequency VHF detections have speeds that are both lower and higher than the dual-frequency head echoes, since the VHF altitude window was both lower and higher than the UHF altitude window.
In summary, single-frequency UHF detections result from the minimum sensitivity of the VHF waveform. Single-frequency VHF detections result from the larger altitude collection region (70-140 km) relative to the UHF collection region (90-110 km).

2.4.6 Polarization Ratio

ALTAIR transmits a right-circularly polarized wave and receives both right-circular (RC) and left-circular (LC) energy. The ratio of the LC to the RC SNR data is defined as the polarization ratio (*PR*), and is computed using

$$PR \; ? \; 10\log_{10}(\frac{LC}{RC}) \; ? \; dB(\frac{LC}{RC}) \qquad \textbf{Eq. 6}$$

+A high polarization ratio typically indicates reflection from a sphere or flat object, while a low polarization ratio indicates reflection from a cylinder- (or line-) like object. A de-polarized signal (transmit and receive only RC) pertains to a "bounce" off the target, such as from a corner reflector. We must caution that we typically apply these terms to highly reflective surfaces (orbiting satellites, for instance), and therefore may not be able to utilize these ideas when analyzing ionospheric reflections.

We use the polarization ratio data to determine the plasma profile perpendicular to boresite and, in conjunction with monopulse data, establish the head echo shape dependence on position and aspect angle. A specular overdense trail, which is detected perpendicular to boresite, is equivalent to reflection from a metallic cylinder or line. ALTAIR transmits RC energy, which can be resolved into two orthogonal, linearly polarized waves. Since the trail is elongated in one dimension, only half of the incident power is scattered by the trail, and the received signal will therefore be equally distributed in the left-circular and right-circular components. Figure 47a contains both the LC and RC power of a VHF head echo/*specular* trail pair, and Figure 47b shows the LC and RC power of a VHF head echo/*non-specular* trail pair. These plots correspond to the range-time-intensity images shown in Figure 47, respectively. In Figure 47a, the specular trail shows the LC and RC signal matching, which corresponds to a polarization ratio = 1, and indicates reflection from a cylindrical or wire-like object. The head echo LC and RC signal, in contrast, do not match. The higher head echo LC signals equates to a high polarization ratio (>10 dB), which indicates that head echoes are reflections from plasma with a more circular- or sphere-like cross-section. In Figure 47b, the head echo also shows a high polarization ratio (15 dB). The non-specular trail polarization ratio is equivalent to approximately 9 dB, and is higher than the specular-trail polarization ratio of 1 dB. Both specular and non-specular trails produce lower polarization ratios than head echoes.

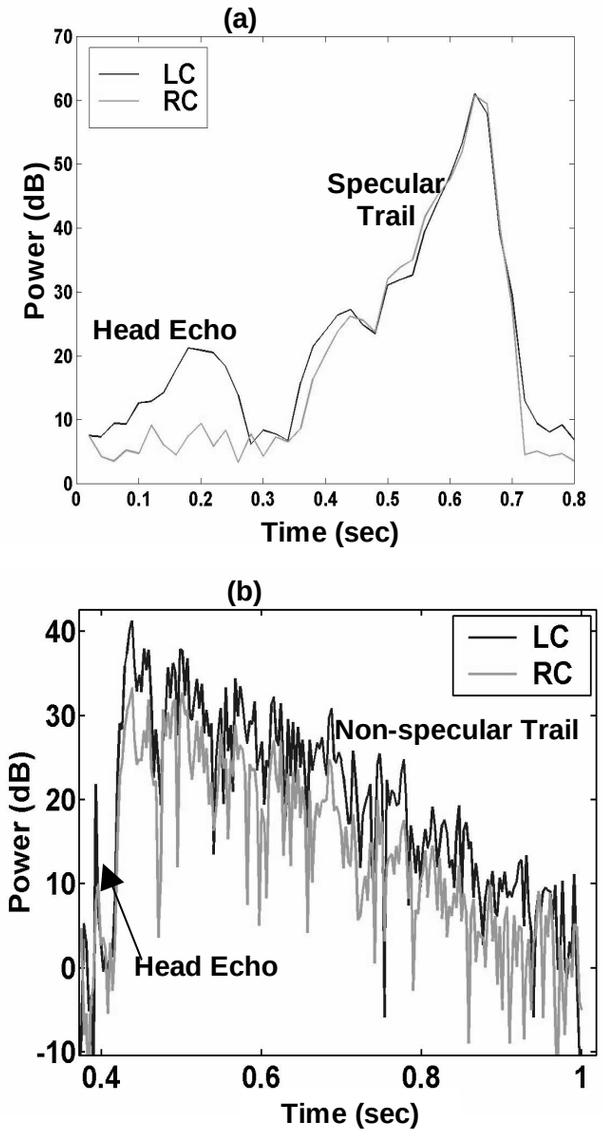

Figure 47. LC and RC signal return for a specular trail, non-specular trail and head echo detected by ALTAIR.

As stated above, reflections from perfect metallic spheres will have high polarization ratios, typically near 20-25 dB. This maximum polarization ratio, which in theory should be infinite, reflects the limiting capability of the system that arises from the slight ellipticity of the wave. High polarization ratios occur because the sphere acts as a perfect reflector, and while the transmitted signal is counter-clockwise (RC), the direction of the reflected signal returns as LC.

The mean polarization ratios of 451 VHF and 174 UHF Leonid 1998 head echoes show peak distributions near 18 and 17 dB, respectively. Although the peak polarization ratios are consistent with sphere-like objects (20 dB), the polarization ratios vary from 1 to over 30 dB. Therefore, we look for characteristics that would distinguish the low from the high polarization ratios. One possibility that can generate unusually low polarization ratios is the limiting sensitivity of the radar. If a head echo has a maximum LC SNR of 15 dB, the *maximum* polarization ratio can only be 10 dB if the noise floor is 10 dB; the minimum polarization ratio is of course still not bounded if the RC signal is above the noise or even exceeds the LC signal. After we normalized these data, the polarization ratios show a much tighter distribution around a mean polarization ratio of 20 dB.

We subsequently analyzed the dual-frequency normalized polarization ratios to determine if the high and low values correlate with one of the other head echo parameters. We examine the resultant dual-frequency head echoes with respect to aspect angle, altitude, and RCS, however we found absolutely no trend. Head echoes looked equally sphere-like regardless of whether ALTAIR was viewing them "head-on" or at some angle and regardless of detection altitude and RCS. We therefore conclude that head echoes are not sensitive to the off-specular angle and suggest at an isotropic scattering mechanism, which is consistent with *Jones and Webster* [1991].

2.5 Head Echo Scattering Theory

The goal of this section is to determine the head echo reflection coefficient so that we may derive the properties of meteoroid masses; this is the first time that plasma densities and meteoroid masses are calculated from head echo data. In general, we believe the front edge of the meteor head echo plasma is spherically distributed, such that the plasma density decreases with distance from the meteoroid; the density distribution is illustrated in Figure 48. As noted earlier, the measured head echo RCS is determined by the energy reflected by an object and is directly proportional to the head plasma reflection coefficient, which should depend upon both head plasma density as well as head plasma size. However, both plasma density and size (r_{max}) are unknown quantities. This section contains a description of two scattering theories that we develop for radar scattering from the plasma that creates a radar head echo, which we term "head plasma", in order to determine plasma density and size.

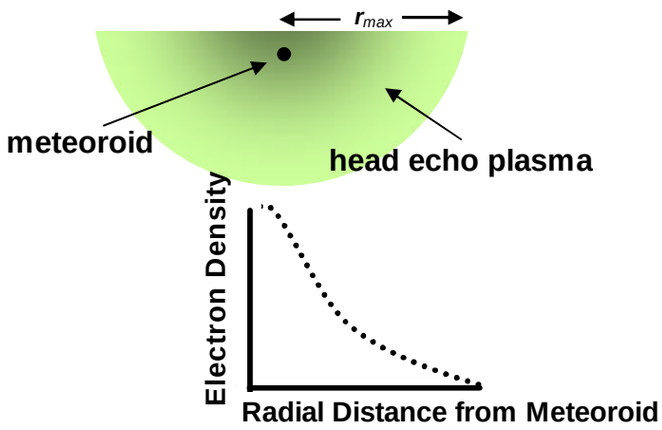

Figure 48. Illustration of how we believe the plasma density decreases with distance from the center of the head echo plasma (meteoroid).

Our first scattering model is termed the "overdense" model, and is a simplified approach to head echo scattering. The overdense model presumes that the head plasma is sufficiently dense to fully reflect the radar wave once it penetrates to a depth where the plasma frequency is equal to the radar frequency. The second model we term the "3D spherical" solution and is so-named for the coordinate system in which it is developed. This model does not assume metallic reflection, but instead develops the theory of electromagnetic wave scattering from plasma using a simplified geometry. We conclude this section with an in-depth analysis of the ALTAIR and TRADEX two- and three-frequency head echo data in order to validate our 3D scattering model.

2.5.1 Overdense Model

A simplistic model of head plasma scattering is the overdense model [*Wannberg et al.*, 1996] [*Close et al.*, 2002]. In the overdense model, the measured head echo RCS correlates to the head plasma's size. The head echo plasma density or plasma frequency is given by

$$f \; ? \; 9000\sqrt{n_{od}} \qquad \textbf{Eq. 7}$$

where f is the incident radar frequency and n_{od} is the overdense head plasma density in cm^{-3}. In this scenario, we assume that the radar wave penetrates the head plasma until it encounters a plasma frequency that is equal to the radar frequency. At this radius, the head plasma behaves approximately as a conducting sphere. The overdense plasma densities, using the ALTAIR and TRADEX radar frequencies, are equal to the following: $n_{od} = 3.2 \times 10^{14}$ m^{-3} at VHF, $n_{od} = 2.2 \times 10^{15}$ m^{-3} at UHF, and $n_{od} = 2.2 \times 10^{16}$ m^{-3} at L-band.

We relate the measured RCS to head plasma size by examining the Mie series. The exact solution for the cross-section of a sphere was first given by *Mie* [1912] and illustrates the dependence between the measured cross section and the physical size of the object. The Mie series can be broken down into three size regions, including objects that are much less than a wavelength (Rayleigh regime), objects that are of the order of the wavelength (resonance region), and objects that are much greater than a wavelength (optical region).

In the Rayleigh regime, where $0 < ka < 1$, the RCS is proportional to the square of the area of the body

$$\frac{?_{meas}}{?a^2} \; ? \; 9\left(\frac{2?a}{?}\right)^4 \qquad \textbf{Eq. 8}$$

where $?_{meas}$ is the head echo RCS, $k = 2?/?$, a is the head plasma radius, and $?$ is the incident wavelength. The resonant scattering regime occurs when $½ < ka < 10$ and is characterized by undulations of $?_{meas}$ caused by the addition of a specular reflection from the front of the sphere with a creeping wave that traverses its shadowed sides. The specular reflection and creeping wave go in and out of phase due to the difference in their path lengths. Finally, the optical region, where $ka > 10$, gives rise to RCS values that approximate the physical cross section, or $?_{meas} = ?a^2$, where a is the physical radius. This Mie series also applies to dielectric spheres, although the scattering is more complicated since the incident energy may enter the body and incur several internal reflections before emerging [*Blake,* 1986]. For a dielectric sphere that is large compared to the incident wavelength, the RCS of the sphere decays gradually with increasing size. A small dielectric sphere exhibits an RCS that increases with increasing size.

We examine 20 head echoes detected simultaneously at VHF and UHF, and one head echo detected simultaneously at VHF, UHF and L-band, in order to understand head plasma density dependence on plasma radius. These data, collected during the Leonid 1998 shower, are contained in Figure 49, where 0 m corresponds to the center of the head plasma at the position of the meteoroid. We obtain these results by inputting the LC RCS values into the Rayleigh formula (Eq. 8). Although the general trend appears intuitive (i.e. density decreases with radial distance from the center of the head plasma) there is a variation between head echoes which manifests as crossing lines in Figure 49.

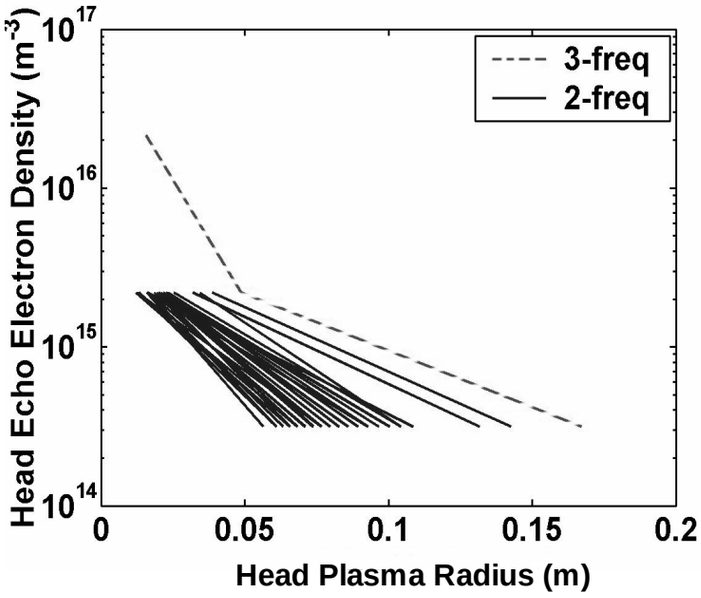

Figure 49. Head plasma density vs. radius for 1 three-frequency and 20 two-frequency head echo detections collected during the Leonid 1998 shower. The critical density is calculated using the overdense formula and is therefore constant at each frequency.

The overdense model is based on the idea that head plasma density decreases with radial distance from the center of the head plasma. While we believe this to be true, the overdense model is an overly simplified approach to head echo scattering for two reasons. The first reason is that this model presumes that all head plasmas have plasma frequencies that exceed the radar frequency, which may or may not be true. Secondly, and more importantly, this model neglects the idea that a plasma can only technically be considered overdense if its dimensions are larger than a wavelength. Overdense refers to total reflection, which means that the radar wave must travel a sufficient distance into the plasma to become completely attenuated, which can not happen if the plasma size is very small relative to a radar

wavelength. While the overdense model does provide the basis for a more rigorous approach, it is clear that we need to derive scattering equations from head plasma that do not include any assumptions about plasma density.

2.5.2 3D Spherical Model

We now derive a 3D spherical scattering model to be applied to head echo scattering. By definition, our spherical model uses a spherical coordinate system to derive scattering solutions for head plasmas. We base our theory on the equations derived for scattering from a sphere with a uniform dielectric constant, which is given by *Mie* [1912], and *Stratton* [1941], as well as the equations for scattering from a cylindrical meteor trail with a non-uniform dielectric constant, which is shown in *Kaiser and Closs* [1951], *Jones and Jones* [1991], and *Poulter and Baggaley* [1977]. We combine these methods to derive a new equation for scattering from head plasma and assume the following: 1) the head plasma is approximated as a sphere with a peak plasma frequency either smaller or greater than the radar frequency; 2) the density and dielectric constant depends only on r; 3) the head plasma is a non-absorbing medium and 4) the head plasma radius depends upon altitude and scales with the atmospheric mean free path and meteoroid speed.

We begin our spherical calculation by describing the time dependence of the steady state fields using the factor $e^{-i\omega t}$. Maxwell's equations in cgs units reduce to

$$\nabla \cdot (\varepsilon \mathbf{E}) = 0; \qquad \nabla \cdot \mathbf{H} = 0;$$
$$\nabla \times \mathbf{E} = \frac{i\omega}{c}\mathbf{H} = k_2 \mathbf{H}; \qquad \nabla \times \mathbf{H} = \frac{-i\omega\varepsilon}{c}\mathbf{E} = -k_1 \mathbf{E} \qquad \textbf{Eq. 9}$$

and are valid both inside and outside the head plasma, which is assumed to have $\mu = 1$. The solutions to Eq. 9 are represented by the superposition of two linearly independent fields, referred to as the transverse magnetic fields ($^{e}\boldsymbol{E}$, $^{e}\boldsymbol{H}$) and the transverse electric fields ($^{m}\boldsymbol{E}$, $^{m}\boldsymbol{H}$). The transverse magnetic field solution is where $H_r = 0$ (hence the superscript "*e*"); the transverse electric field solution is where $E_r = 0$ (hence the superscript "*m*").

We first consider the transverse magnetic component, where $H_r = 0$. Since $\nabla \cdot \mathbf{H} = 0$ according to Maxwell's equation, we can write both $^{m}H_\psi$ and $^{m}H_\psi$ in terms of a scalar function, ψ, such that

$$ {}^{e}H_{?} \; ? \; ? \frac{1}{\sin ?} \frac{? {}^{e}?}{??}; \qquad {}^{e}H? \; ? \frac{? {}^{e}?}{??} \qquad . \qquad \textbf{Eq. 10} $$

Also, since $E \; ? \; ? \frac{1}{k_1} ? \; ? H$, we determine that

$$ {}^{e}E_{?} \; ? \; \frac{1}{k_1 r} \frac{? {}^{2}(r {}^{e}? \;)}{? r??}; \qquad {}^{e}E? \; ? \; \frac{1}{k_1 r \sin ?} \frac{? {}^{2}(r {}^{e}? \;)}{? r??} \qquad . \qquad \textbf{Eq. 11} $$

We derive the scalar potential equation for the transverse magnetic component by first noting that $? \; ? \; ? \; ? A ? k^2 A ? k_1 {}^{e}?$ where $\boldsymbol{A}$ is a vector potential and $k^2 = (-k_1 k_2)$. Then, using a Lorentz gauge, $? \; ? A ? k_1 ?$, the scalar Helmholtz equation becomes

$$? {}^{2}({}^{e}? \;) ? \frac{? \, k_1}{k_1 r} \frac{? (r {}^{e}? \;)}{? r} ? {}^{e}? \, k^2 \; ? \; 0 \quad . \qquad \textbf{Eq. 12} $$

This equation provides the radial component of the electric field, or

$$ {}^{e}E_r \; ? \; \frac{1}{k_1} (r {}^{e}? \, k^2 ? \frac{? \, k_1}{k_1} \frac{? (r {}^{e}? \;)}{? r} ? \frac{? {}^{2}(r {}^{e}? \;)}{? r^2}) \quad . \qquad \textbf{Eq. 13} $$

Next we consider the transverse electric component, where $E_r = 0$. Here we use $? \; ? (? E) ? \; ?? \; ? E ? E ?? ? \; ? \; 0$. However, since $?$ is only a function of r and $E_r = 0$, we may drop the second term, such that $?? \; ? E ? \; 0$. Again, we can write both ${}^{m}E_{?}$ and ${}^{m}E_{?}$ in terms of a scalar function, or

$$ {}^{m}E_{?} \; ? \; \frac{1}{\sin ?} \frac{? {}^{m}?}{??}; \qquad {}^{m}E_{?} \; ? \; ? \frac{? {}^{m}?}{??} \quad . \qquad \textbf{Eq. 14} $$

To complete the equations, we use $H \; ? \; \frac{1}{k_2} ? \; ? E$, which provides

$$ {}^{m}H_{?} \; ? \; \frac{1}{k_2 r} \frac{? {}^{2}(r {}^{m}? \;)}{? r??}; \qquad {}^{m}H_{?} \; ? \; \frac{1}{k_2 r \sin ?} \frac{? {}^{2}(r {}^{m}? \;)}{? r??} \quad . \qquad \textbf{Eq. 15} $$

The scalar Helmholtz equation for the transverse electric component becomes

$$? {}^{2}({}^{m}? \;) ? {}^{m}? \, k^2 \; ? \; 0 \qquad \textbf{Eq. 16} $$

which provides the radial component of the magnetic field, or

$$^{m}H_r = \frac{1}{k_2}(r^{m} k^2 + \frac{\partial^2(r^{m})}{\partial r^2}) \qquad \textbf{Eq. 17}$$

Note that the transverse electric component of the Helmholtz equation (Eq. 16) is similar to the Schrodinger equation.

For the case of an inhomogeneous scatterer, we solve Eq. 12 using the standard method of separation of variables [*Jackson*, 1975] by defining $^{e}\Pi = {}^{e}R(r)\Theta(\theta)\Phi(\phi)$. Therefore, the radial part of Eq. 12 satisfies the differential equation

$$R'' + R\frac{2}{r} + \frac{\partial}{\partial}\frac{\partial}{\partial} + R k^2 + \frac{\partial}{\partial r} + \frac{n(n+1)}{r^2} = 0 \qquad \textbf{Eq. 18}$$

where the prime denotes differentiation with respect to *r*.

We return to the problem of an incident plane wave polarized in the *x*-direction, propagating in the *z*-direction, and incident upon spherical plasma (head plasma) embedded in a homogeneous medium. The incident plane wave in the radial direction may be represented by

$$E_{inc}(z,t) = \hat{a}_x E_o e^{-ikz+i\omega t} = \hat{a}_x E_o e^{-ikr\cos\theta+i\omega t} \qquad \textbf{Eq. 19}$$

where *r* is the radius vector, $k = \omega/c$, ω is the frequency and $\hat{a}_x$ is the direction vector given by

$$\hat{a}_x = \sin\theta\cos\phi\,\hat{i} + \cos\theta\cos\phi\,\hat{j} - \sin\phi\,\hat{k} \qquad \textbf{Eq. 20}$$

where θ and ϕ are the spherical angles and $\hat{i}, \hat{j}$ and $\hat{k}$ are unit vectors in the *r*, θ and ϕ directions, respectively. We expand the incident wave in terms of spherical harmonics by using the wave transformation

$$e^{ikr\cos\theta} = \sum_{n=0}^{\infty} i^n(2n+1)j_n(kr)P_n(\cos\theta) \qquad \textbf{Eq. 21}$$

where j_n is the *n*th order Bessel function of the first kind and $P_n(\cos\theta)$ is the *n*th order Legendre function.

The time-independent incident electric field is now characterized using spherical Bessel functions, and in the radial direction is given by

$$E_{r\_inc} \propto E_o \sin\theta \cos\theta e^{-ikr\cos\theta} \propto E_o \frac{\cos\theta}{ikr} \frac{\partial}{\partial\theta}(e^{-ikr\cos\theta}) \quad \textbf{Eq. 22}$$

which becomes

$$E_{r\_inc} \propto -\frac{iE_o\cos\theta}{kr} \sum_{n=1}^{\infty} i^n (2n+1) j_n(kr) P_n^1(\cos\theta) \quad \textbf{Eq. 23}$$

where $P_n^1(\cos\theta)$ is the associate Legendre function; we now start the summation with $n = 1$ because $P_0^1(\cos\theta) = 0$. Likewise, the time-independent reflected electric field in the radial direction becomes

$$E_{r\_ref} \propto -\frac{iE_o\cos\theta}{kr} \sum_{n=1}^{\infty} i^n R_n (2n+1) h_n^1(kr) P_n^1(\cos\theta) \quad \textbf{Eq. 24}$$

where R_n is the reflection coefficient, and $h^1{}_n$ is the nth order Hankel function of the first kind. The penetrating electric field inside the head plasma in the radial direction is given by

$$E_{r\_pen} \propto -\frac{iE_o\cos\theta}{k_p r} \sum_{n=1}^{\infty} i^n c_n (2n+1) j_n(k_p r) P_n^1(\cos\theta) \quad \textbf{Eq. 25}$$

where k_p is the wavelength associated with the head plasma, and c_n is a coefficient associated with the field inside the head plasma.

The total field external to the head plasma, $E_{r\_ext} = E_{r\_inc} + E_{r\_ref}$, now using the Hankel function of the second kind, is

$$E_{r\_ext} \propto -\frac{iE_o\cos\theta}{kr} \sum_{n=1}^{\infty} i^n P_n^1(\cos\theta)(2n+1)\left[j_n(kr) + R_n(2j_n(kr) + h_n^2(kr))\right] \quad \textbf{Eq. 26}$$

We can write Eq. 26 as a transverse magnetic potential, $^e\Pi_{ext}$, which satisfies Eq. 10 through Eq. 17, and is shown to be

$$^e\Pi_{ext} \propto -\frac{E_o k\cos\theta}{\theta} \sum_{n=1}^{\infty} \frac{i^n (2n+1) P_n^1(\cos\theta)}{n(n+1)} \left[j_n(kr) + R_n(2j_n(kr) + h_n^2(kr))\right] \quad \textbf{Eq. 27}$$

For a sphere with a uniform dielectric constant, we can solve for the reflection coefficient and c_n by equating the sum of the incident and reflected electric (and magnetic) fields (Eq. 26) with the penetrating field (Eq. 25). In other words, a single transition radius means the fields are continuous at $r = r_{max}$ and will produce the typical Mie scattering curve for a sphere with an arbitrary size and an incident radar wave of arbitrary wavelength. However, because we have head plasma with a dielectric constant that depends upon radial distance from the meteoroid, we cannot use a uniform dielectric

constant. Our approach will be to compare the form of the potential in Eq. 27 with the electrostatic solution, derived from Laplace's equation, in order to solve for the head plasma density.

We now consider Laplace's equation in order to determine how the potential varies as a function of radial distance from the center of the head plasma. For a spherical plasma distribution with a dielectric dependent upon *r*, Laplace's equation is given by

$$? ? ?? V ? ?? ^2V ? 0 \qquad \textbf{Eq. 28}$$

where ? is the head echo's dielectric and *V* is the potential. In spherical coordinates, the potential function is

$$V ? \cos? \overset{?}{\underset{n?1}{?}} V_n P_n^1(\cos?) \qquad \textbf{Eq. 29}$$

where V_n is the solution of the radial component of Laplace's equation, or

$$\frac{d}{dr}(?r^2 \frac{dV_n}{dr}) ? n(n ? 1)?V_n. \qquad \textbf{Eq. 30}$$

The solution to Eq. 30 in regions of constant ? is given by

$$V_n ? A_n r^n ? B_n r^{?(n?1)} \qquad \textbf{Eq. 31}$$

where A_n and B_n are coefficients determined by boundary conditions.

Eq. 30 gives a solution to the full electromagnetic wave system when the dominant scattering mechanism results from electrostatic scattering in a manner similar to that described for cylindrical meteor trail scattering by *Kaiser and Closs* [1951]. The electrostatic form of the potential in Eq. 30 has the same form of the exact electromagnetic potential given in Eq. 18, if we stipulate that $|(kr)^2 - r?'/?| << n(n+1)$. This assumption limits us to cases where the radar wavelength is usually greater than the size of the head plasma, but allows us to use the more convenient form of the potential given by Eq. 31.

To obtain the reflection coefficient, R_n, we combine Eq. 29 and Eq. 31 and compare the result to Eq. 27. Our derivation gives

$$? \frac{1}{R_n} ? 2 ? \frac{nh_n^2(kr)A_n r^{2n?1}}{(n ? 1) j_n(kr) B_n}. \qquad \textbf{Eq. 32}$$

Eq. 30 has two singularities which we must address, including at the center of the head plasma ($r = 0$), as well as where $? = 0$ (for sufficiently dense plasmas), which we will define to be at $r = r_0$. The singularity at the center can be dealt with by requiring that V_n be well-behaved at the origin; the singularity at the boundary ($? = 0$) requires complex integration because the dielectric constant can be negative inside the head plasma but positive outside, which means that it passes through a zero point. We can address this singularity by considering a thin region (smaller than a radar wavelength) at $r = r_0$ and setting $x = r^n$ into Eq. 30, which gives

$$\frac{d}{dx}(? \frac{dV_n}{dx}) \; ? \; ? \frac{(n \; ? \; 1)}{n} ? \frac{d}{dx}(\frac{V_n}{x}) \qquad \textbf{Eq. 33}$$

which in this region is approximately

$$\frac{d}{dx}(? \frac{dV_n}{dx}) \; ? \; ? \frac{(n \; ? \; 1)}{n} \frac{?}{r_0^n} \frac{dV_n}{dx} \qquad \textbf{Eq. 34}$$

meaning

$$\text{a} \; ? \frac{dV_n}{dx} \; ? \; const. \; ? \; C_n \qquad \text{or} \qquad ? \frac{dV_n}{dr} \; ? \; C_n \qquad \textbf{Eq. 35}$$

when $|r- r_0|<<r_0$. To solve this differential equation, we use the form of the plasma density given in Eq. 53 and expand the corresponding dielectric constant in a power series around $(r- r_{max})$, such that

$$? \; ? \; (r \; ? \; r_0)? \; '(r_0) \qquad \textbf{Eq. 36}$$

where $?'$ is the derivative of Eq. 55 at $? = 0$. The physical significance of $?'r_0$ corresponds to the value $?$ would have at the center of the head plasma if the gradient of $?$ in the thin boundary region had been continued into the center of the head plasma. We then use contour integration on Eq. 35 to obtain

$$V_{nB} \; ? \; V_{nA} \; ? \; \frac{C_n}{? \; '(r_0)} [\ln \left| \frac{? \; _B}{? \; _A} \right| \; ? \; i? \;] \qquad \textbf{Eq. 37}$$

where V_{nA} and $?_A$ are the potential and dielectric constant inside the head plasma, and V_{nB} and $?_B$ are the potential and dielectric constant outside of the head plasma. We must still solve for the constants A_n and B_n in Eq. 32, which can be determined either numerically or analytically. We expound upon both techniques in the next two sub-sections.

2.5.2.1 Approximate Analytical Technique

In order to derive an analytical solution for the ratio A_n/B_n, we invoke the Herlofson model described in *Herlofson* [1951], which is an approximation to our dielectric constant, Eq. 55, which is shown in Figure 50a. The Herlofson approximation is shown in Figure 50b and will now be used to solve for the constants A_n and B_n. *Herlofson* [1951] and *Kaiser and Closs* [1951] developed this method in cylindrical coordinates to characterize scattering from a meteor trail, and we apply their techniques to head plasma scattering by changing their equations to accommodate a spherical coordinate system.

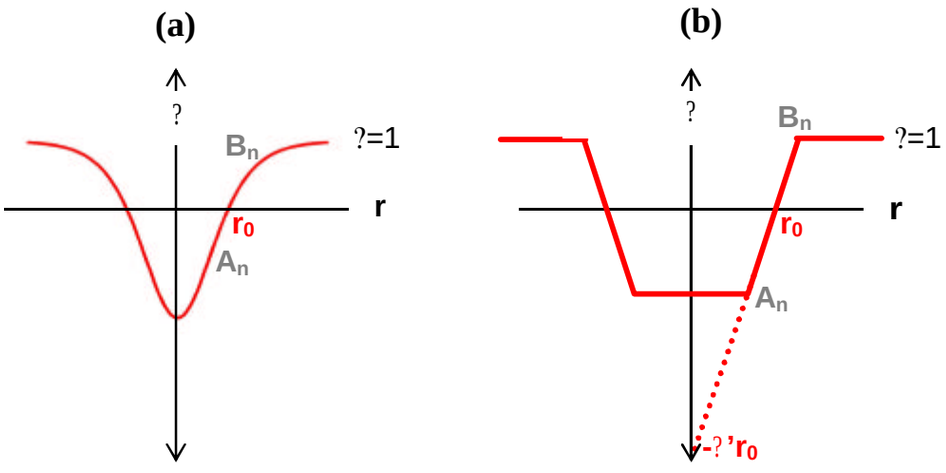

Figure 50. (a) Illustration of the actual parabolic exponential dielectric function, and (b) the Herlofson approximation to this model, where the head plasma is modeled as a homogeneous plasma at its center with a thin region of increasing dielectric.

Within the homogeneous region (A_n in Figure 50b), we set $V_{nA} = r^n$ which allows us to solve for the constant in Eq. 35, $C_n = ?nr_0^{n-1}$, the potential in Eq. 37, V_{nB}, and also the derivative of the potential with respect to r, V_{nB}', or

$$V_{nB} ? r_0^n ? \frac{n?r_0^n}{r_0?'(r_0)}[? \ln|?_A| ? i?] \qquad \textbf{Eq. 38}$$

$$r_0 V'_{nB} ? n?_A r_0^n \qquad \textbf{Eq.39}$$

We can solve for the coefficients A_n and B_n by comparing Eq. 31 and the derivative of the potential in Eq. 31 at $r = r_0$

$$V_{nB} ? A_n r_0^n ? B_n r_0^{?(n?1)} \qquad \textbf{Eq. 40}$$

$$r_0 V'_{nB} = nA_n r_0^n + (n+1)B_n r_0^{-(n+1)} \tag{41}$$

with Eq. 38 and Eq. 39. Specifically, we add and subtract Eq. 38 with Eq. 40, and Eq. 39 with Eq. 41 to solve for the coefficients, which gives

$$\frac{A_n}{B_n} = \frac{(n+1)}{n r_0^{2n+1}} \frac{\left[1 + \frac{\varepsilon_A n}{n+1} + \frac{\varepsilon_A n}{\varepsilon'(r_0) r_0}(i\varepsilon - \ln|\varepsilon_A|)\right]}{\left[1 - \varepsilon_A + \frac{\varepsilon_A n}{\varepsilon'(r_0) r_0}(i\varepsilon - \ln|\varepsilon_A|)\right]} \tag{42}$$

where ε_A is a constant. The mode (n) to which we must sum depends upon the altitude (head plasma radius) and the incident wavelength. Typically, we must sum to higher modes for large head radii.

2.5.2.2 Numerical Technique

To determine the ratio A_n/B_n numerically, we use the technique of *Kaiser and Closs* [1951] and integrate Eq. 30 using a piecewise linear approximation to solve for the potential at each increment. First, we define the variable $\rho = r/r_{max}$ so that Eq. 30 becomes

$$\frac{d}{d\rho}\left(\rho^2 \frac{dV_n}{d\rho}\right) = n(n+1)\rho V_n \tag{43}$$

where the variables are defined as before. We begin at $\rho = 0$ and divide the head plasma radius into small segments until we reach $\rho = 1$. We then evaluate the potential in each segment, keeping in mind that the dielectric constant varies as a function of radius as well, using a method of successive approximations. Therefore, if we know the potential at $\rho = \rho_1$, we can determine the potential at $\rho = \rho_2$, using $\rho_2 = \rho_1 + \Delta\rho$.

We begin by integrating Eq. 43

$$\rho^2 \frac{dV_n}{d\rho} = n(n+1)\int_0^{\rho} \rho V_n d\rho \tag{44}$$

where the integration is carried out by stepping in small segments of ρ. We need to know both V_n and $dV_n/d\rho$ at ρ_1, as well as guess at a solution for V_n at ρ_2 in order to begin the numerical integration. We determine V_n and $dV_n/d\rho$ at ρ_1 by noting that when $\rho \ll 1$ (at the center of the head plasma), $\rho' = 0$.

Therefore, integration of Eq. 44 for $\varepsilon \ll 1$ gives $V_n = \varepsilon^n$ and $dV_n/d\varepsilon = n\varepsilon^{n-1}$, which are the values to be used at ε_1.

Now, by applying the successive approximation technique, we determine $dV_n/d\varepsilon$ at ε_2 using

$$(\varepsilon^2 \frac{dV_n}{d\varepsilon})_2 = (\varepsilon^2 \frac{dV_n}{d\varepsilon})_1 + \frac{\varepsilon}{2} n(n-1)\varepsilon(V_n)_1 + (\varepsilon V_n)_2 \quad \textbf{(45)}$$

where the subscripts 1 and 2 refer to the values of the potential and dielectric constant at ε_1 and ε_2. By definition,

$$V_n = \int_0^{\varepsilon} \frac{dV_n}{d\varepsilon} d\varepsilon \quad \textbf{(46)}$$

which, using the numerical approximation, is

$$(V_n)_2 = (V_n)_1 + \frac{\varepsilon}{2}[(\frac{dV_n}{d\varepsilon})_1 + (\frac{dV_n}{d\varepsilon})_2] \quad \textbf{(47)}$$

and provides us with another guess for V_n at ε_2 to be used in Eq. 45. We now repeat the calculations (Eq. 45 and Eq. 47) until $dV_n/d\varepsilon$ at ε_2 no longer changes. Note that these equations can only be used if ε does not pass through a singularity.

To integrate through the singularity at $\varepsilon = 0$ (i.e. for head plasmas with plasma frequencies above the radar frequency), we use Eq. 38 to solve for the potential (V_{nB}), which we now write as

$$V_{nB} - V_{nA} = \frac{\varepsilon[dV_n/d\varepsilon]}{\varepsilon'(r_0)}[\ln\left|\frac{\varepsilon_B}{\varepsilon_A}\right| - i\pi] \quad \textbf{(48)}$$

where $\varepsilon'(r_o)$ is the derivative of ε at $\varepsilon = 0$. We evaluate the real and imaginary parts of Eq.48 separately around the singularity, and then continue using Eq. 45 and Eq. 47 to determine the potential once the dielectric constant becomes positive again.

Finally, to determine the coefficients A_n and B_n outside the head plasma at $\varepsilon = 1$, we use Eq. 31 with ε, or

$$V_n = A_{n\varepsilon}\varepsilon^n + B_{n\varepsilon}\varepsilon^{-(n+1)} \quad \textbf{(49)}$$

where $A_{n\varepsilon}$ and $B_{n\varepsilon}$ are defined as

$$A_n = \frac{A_{n-1}}{r_{\max}^{n}} \qquad \text{and} \qquad B_n = B_{n-1} r_{\max}^{n-1} \tag{50}$$

and r_{max} is defined by Eq. 54. Hence, using the final values of the potential and the derivative of the potential at $\rho = 1$ ($dV_n/d\rho$ and V_n) calculated using the numerical technique, we determine the coefficients A_n and B_n using

$$A_{n-1} = \frac{1}{2n-1}\left[V_n - \rho^{-n}(n-1)\frac{dV_n}{d\rho} r^{-n-1}\right] \tag{51}$$

and

$$B_{n-1} = \frac{nr^{n-1}}{2n-1}\left[V_n - \frac{dV_n}{d\rho}\frac{r}{n}\right] \tag{52}$$

with Eq. 50 for use in Eq. 32.

2.5.2.3 3D Spherical Solution

Head echo RCS depends of course upon the density of the head plasma distribution. We choose this distribution using a physically plausible approximation and then derive the expected RCS from this model using our spherical scattering theory just described. We approximate the head plasma density as a Gaussian function, or

$$n(r) = n_0 \exp(-(r / r_{\max})^2) \tag{53}$$

where n_0 is the maximum electron density for each head plasma (near the meteoroid's position at the center of the head plasma), r is the radial distance from the center of the head plasma, and r_{max} defines what we call the "physical size" of the head plasma and is given by

$$r_{\max} = (.023)*(2.845\cdot 10^{18} v^{-.8} / n) \tag{54}$$

where v is the 3D speed of the head echo in km/s and n is the background number density at the head echo detection altitude in m^{-3} [*Jones*, 1995] Therefore, the dielectric constant in spherical coordinates, varies as

$$\frac{\varepsilon(r)}{\varepsilon_o} = 1 - \frac{\omega_p^2}{\omega^2} = 1 - \frac{n(r)e^2}{\varepsilon_o m \omega^2} \tag{55}$$

where ε_o is the permittivity in free space, ω_p is the plasma frequency, ω is the radar frequency, e is the electron charge, m is the electron mass, and $n(r)$ is the plasma density defined by Eq. 53.

We relate the measured scattering cross section, σ_{meas}, to the reflection coefficient using

$$\sigma_{meas} = \sum_n \frac{\pi\lambda^2 (n + 1/2)^2}{\pi} |R_n|^2 \quad \textbf{(56)}$$

where λ is the radar wavelength [*Jackson*, 1975] [*Morse and Feshbach*, 1953] and σ_{meas} is the measured head echo RCS. We convert the spherical reflection coefficient, using Eq. 32 and the Herlofson approximation, to cross section, σ_{meas}, using Eq. 56 and plot these data as a function of r_{max} and maximum head plasma frequency in Figure 51 for a theoretical array of maximum head plasma frequencies (plasma densities) detected using the VHF frequency; the solid line denotes the VHF frequency. When the plasma frequency approaches the radar frequency, the cross sections approach 0 dBsm for large radii. The smallest cross-sections correspond to head plasmas with small radii and low plasma frequencies.

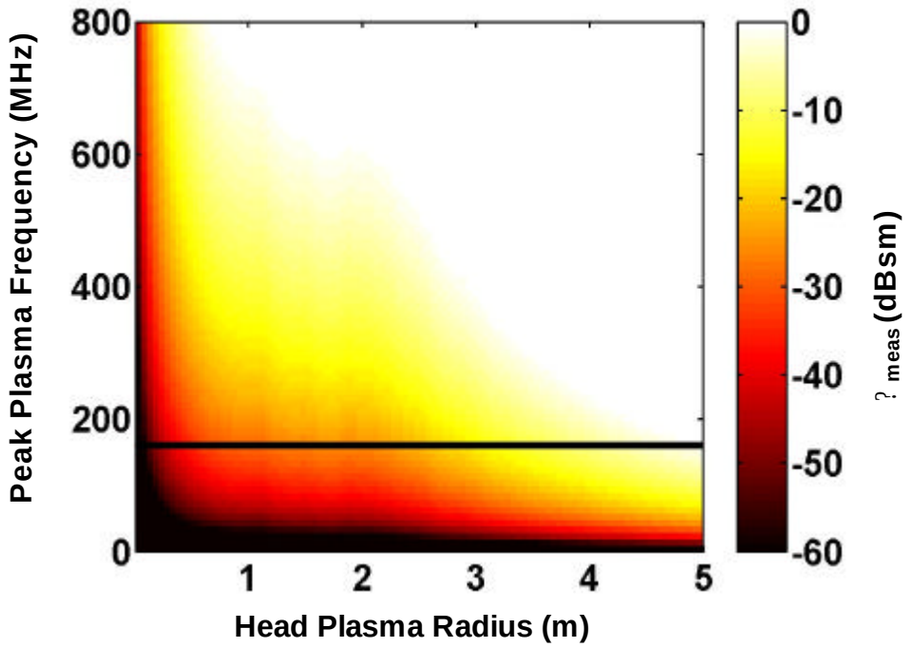

Figure 51. VHF head echo cross-section in dBsm, converted from reflection coefficient, calculated by applying the spherical scattering method to a theoretical array of peak head plasma frequencies and head plasma radii. The solid black line denotes the VHF frequency.

2.5.2.4 3D Spherical Solution Validation

As stated earlier, we need to determine not just the profile of the head plasma, but also its size. By using two-frequency detections, we vary the head plasma size until the peak plasma density

approximately matches at both frequencies. We choose the size of the optimum head plasma to be approximately one mean free path with a dependence upon head echo speed. Specifically, we use the modified Jones formula (Eq. 54) to define the head plasma radius; this formula is approximately 0.023 times the Jones' formula [1995], which incorporates head echo speed. Therefore, the head echo's altitude provides the head plasma radius. Using head plasma radius, as well as measured LC RCS, we subsequently interpolate on Figure 51 to find the maximum plasma density, n_o, for each VHF head echo, and use the corresponding wavelength-dependent figures for the higher frequency (UHF, L-band) head echo measurements.

We validate the spherical scattering solution by examining head echoes detected simultaneously at multiple frequencies. As we previously noted, the LC RCS observations are highly dependent on radar frequency, however the head plasma density should obviously be independent of radar frequency. Therefore, if we obtain the same maximum head plasma density using simultaneous multi-frequency observations, we can claim that our head echo scattering theory is self-consistent.

We use three methods to validate our theories. First, we compare the maximum head plasma densities, derived using our new 3D scattering solution, for 22 head echoes detected simultaneously at VHF and UHF. Second, we examine the head plasma density dependence on altitude at VHF and UHF to assess whether the dependence agrees using both frequencies. Third, we compare the maximum head plasma density for a head echo detected simultaneously at VHF, UHF and L-band using the TRADEX radar. These results show that our model is providing consistent results across frequencies and a reasonable estimate of the maximum head plasma density and line density.

Figure 52 shows the maximum LC RCS extracted from 22 head echoes detected simultaneously at VHF and UHF during the Leonid 1998 shower. We use only the maximum RCS from each head echo streak, so that each head echo streak is represented by only one point, regardless of how extended it is in range and time. The average difference between VHF and UHF LC RCS for these 22 head echoes varies from 12.2 to 24.6 dBsm, which is equivalent to a difference of 16.6 to 2.9×10^2 m^2 between the VHF and UHF data; the VHF frequency always correlates to the higher RCS.

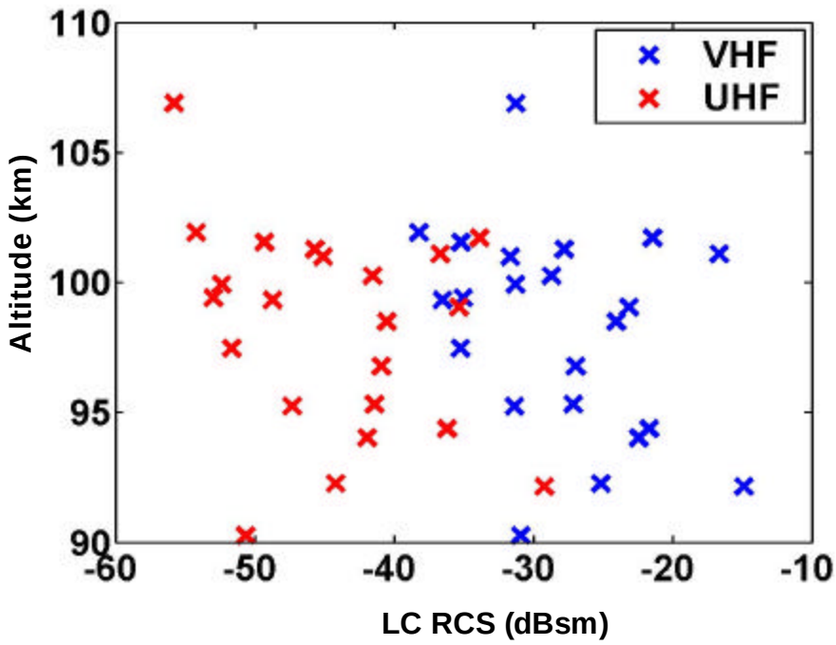

Figure 52. The maximum measured RCS from 22 head echoes detected simultaneously at VHF and UHF during the Leonid 1998 shower.

We now convert the maximum LC RCS measurements, shown in Figure 52, to maximum head plasma density by utilizing our new 3D spherical model. We utilize both the Herlofson analytical approximation as well as the numerical integration technique in the spherical model in order to compare our results. The head plasma densities output from both solutions are plotted in Figure 53 and show that the spherical solutions produce approximately the same density using the VHF and UHF frequencies. As expected, the numerical technique produces densities that are more similar between VHF and UHF relative to the Herlofson analytical approximation. The median ratio of the VHF and UHF densities using the numerical technique is only 1.2, whereas the median ratio using the approximation technique is 1.7. As expected, the numerical technique, which does not approximate the dielectric constant as uniform in the center of the head plasma, produces more similar plasma densities and is therefore a better method for calculating head plasma density.

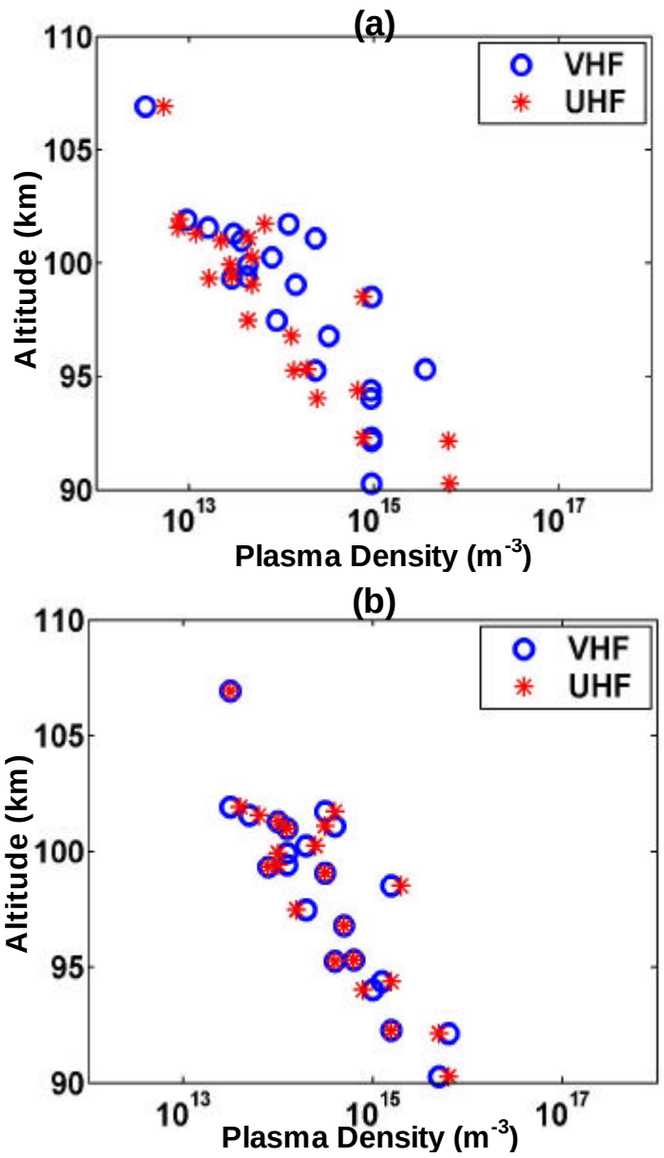

Figure 53. The maximum LC RCS from 22 head echoes, detected during the Leonid 1998 shower, converted to plasma density by using the 3D spherical scattering method with (a) the Herlofson approximation and (b) the numerical integration technique.

We examine the ratio of the maximum plasma density to the minimum plasma density using 101 simultaneous detections detected during the Leonid 1998 shower. The minimum ratio is 1 using both the numerical and analytical spherical methods. The largest ratio is approximately $7x10^2$ using the approximation technique, and $1x10^2$ using the numerical technique. The median ratios using the

analytical and numerical methods are 2.5 and 1.5, respectively. These results again show that the numerical spherical solution best approximates the head plasma density.

In order to understand the dependence of head plasma density on altitude, we next apply our scattering methods to the maximum RCS extracted from 451 VHF and 174 UHF head echoes detected during the Leonid 1998 shower. Intuitively, we believe that for a single head echo streak, plasma density should increase as altitude decreases, and then subsequently fall-off sharply as the meteoroid disintegrates at the lowest detected altitude. However, by extracting only the maximum plasma density from each head echo streak, we believe that the maximum head plasma density from each streak should increase as detection altitude decreases, since the atmospheric density increases as altitude decreases and larger mass meteoroids will survive to lower altitudes.

We use the numerical spherical solution to determine the maximum plasma densities and plot these as a function of altitude. These data are shown in Figure 54 for both the VHF (a) and UHF (b) measurements. Once again, head plasma density decreases as head radius (and altitude) increases; the UHF data show a cut-off at 110 km altitude because of the smaller altitude extent. The spherical solution produces densities from 10^{12} to 10^{17} m^{-3}, which span densities that are underdense [*Mathews et al.*, 1997] as well as overdense. The spherical densities decrease continuously as altitude increases, as our intuition suggests.

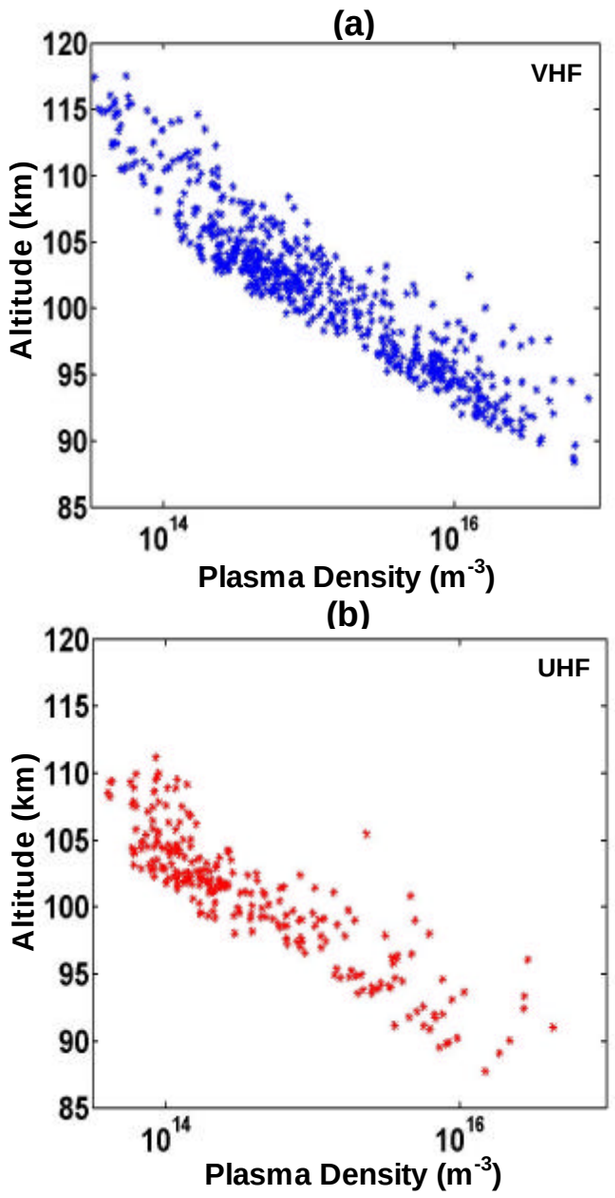

Figure 54. Plots of maximum plasma density, calculated using the spherical solution, as a function of altitude that show that density increases as altitude decreases. Each data point corresponds to the maximum measured LC RCS from (a) 451 VHF and (b) 174 UHF head echoes detected during the Leonid 1998 shower.

As a final validation of our new 3D scattering model, we use the first head echo detected simultaneously at three frequencies, including VHF, UHF and L-band; the TRADEX radar detected the L-band head echo. For this measurement, the meteoroid traversed the main beam of the TRADEX L-

and S-band system, as well as the ALTAIR UHF and VHF system. While the head echo was clearly located in the mainbeam of both the TRADEX L- and S-band beams, there was no S-band detection. Radars using C-, Ka- and W-bands also illuminated this meteor, but received no returns. The maximum VHF head echo LC RCS is -10.6 dBsm at 95.75 km altitude. A second VHF peak of -8.6 dBsm occurred at 100.1 km, however this is outside the beam width of the TRADEX system and is neglected. The maximum UHF LC RCS is -25.8 at 95.59 km, and the maximum L-band LC RCS is -36 dBsm at 95.58 km. The average 3D speed of this meteoroid is 66.5 km/s. After applying the numerical spherical model to the VHF, UHF and L-band RCS values, we obtain the following plasma densities: 1.14×10^{17} m^{-3} using VHF, 7.39×10^{16} m^{-3} using UHF, and 1.17×10^{17} m^{-3} using L-band. Note the strong agreement between the VHF and L-band plasma densities; the UHF density is less than a factor of 2 different.

2.6 Meteoroid Mass Determination

For the first time, we calculate the mass of a meteoroid using head echo data. We achieve this new result by converting head echo RCS to electron line density using both the overdense and the new spherical scattering theory just described. This section shows the dependence between meteoroid mass, detection altitude and electron line density.

First, we determine the line density, q, by using the peak plasma density that is output from the 3D spherical solution. For meteor trails, q is constant at a given altitude. For head echoes, however, q depends strongly on r and varies as a function of r up to its maximum radius, r_{max}. We therefore use the average line density for subsequent use in our calculations, which is given by

$$q = \frac{1}{N} \sum_{r=0}^{r=r_{max}} n(r) \cdot r^2 \qquad \textbf{(57)}$$

where $n(r)$ is the plasma density at radius r, r_{max} is given by Eq. 54, and N is the number of steps between $r = 0$ and $r = r_{max}$. The plasma density $n(r)$ is calculated using Eq. 53, where n_o is output from the spherical solution.

We also determine the line density using the overdense model. Recall that in the overdense model, we use the measured RCS in the Rayleigh equation to determine the radius of the plasma, r, at the pre-determined overdense density, n_{od}. The line density is therefore given by

$$q \propto n_{od} \alpha r^2 \quad \textbf{(58)}$$

The line densities, calculated using either method, are then input into the standard meteoroid mass-loss equation to determine meteoroid mass

$$m \propto \int \frac{q \alpha v}{\beta} dt \quad \textbf{(59)}$$

where m is the meteoroid mass, μ is the mean molecular mass, which is approximately 20 amu for stony meteoroids dominated by 60% oxygen and 25% silicon, v is the head echo 3D speed and β is the ionization probability, which depends upon the speed and scales approximately as $v^{2.8}$ [*Jones*, 1997]. Alternatively, we could use the ionization probability equation given by *Lebedinets et al.*, [1973] or *Bronshten* [1983], however these equations for β typically only change the meteoroid mass by less than a factor of 2. For the remainder of this section, we use only the 3D spherical model to compute meteoroid mass.

We examine a single head echo detected simultaneously by ALTAIR at VHF and at UHF during the Leonid 1998 shower. First, we correct the LC RCS for position within the ALTAIR beam using the monopulse-offset values. Specifically, we find the position of the head echo within the beam using the monopulse data, and then determine the reduction in SNR at that position by approximating the SNR distribution of the ALTAIR beam pattern. We then adjust the head echo RCS accordingly to remove any beam pattern effects. The corrected LC RCS is plotted as a function of altitude in Figure 55 for both the VHF and UHF detected head echoes. On average, the VHF RCS is 20 dBsm higher than the corresponding UHF RCS. We must stipulate that our approximation of the SNR distribution of the ALTAIR beam pattern takes the SNR as a function of elevation and maps it to azimuth, which creates a symmetric grid in both azimuth and elevation. This simplistic mapping was necessary due to an upgrade in the VHF feed and a lack of data on the old (i.e. 1998 and 1999) VHF hardware. In future data collections, we hope to obtain more precise beam patterns and therefore, more accurately correct the ALTAIR RCS measurements.

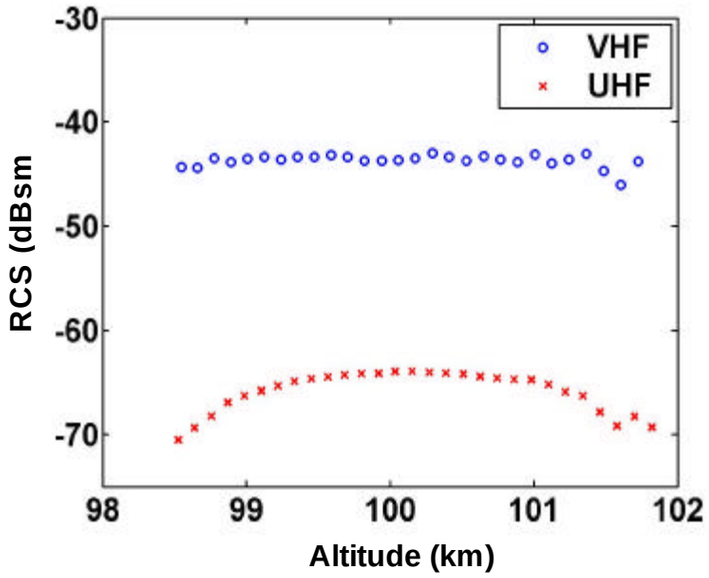

Figure 55. A single head echo, detected simultaneously at VHF and UHF during the Leonid 1998 shower, showing RCS as a function of altitude.

We now use the numerical spherical method to calculate the maximum plasma density of each head echo pulse using this head echo streak at both VHF and UHF. Next, we input these densities, one per altitude bin, into Eq. 57 to calculate electron line density, and then input the line density as well as the head echo 3D speed into Eq. 59 to calculate meteoroid mass, using both the VHF and UHF data. The line density and meteoroid mass should be the same regardless of detection frequency, since the object creating both the VHF and UHF head plasma, i.e. the meteoroid, is the same. These data are plotted in Figure 56 and Figure 57 and show the electron line density and meteoroid mass as a function of altitude at both frequencies. The average measured LC RCS shows a 20 dBsm difference between VHF and UHF, yet the electron line densities, as well as the meteoroid masses, are approximately the same at VHF and UHF. There is a slight offset between the VHF and UHF line densities and masses at the highest altitudes. We attribute this offset to either error in the monopulse data, which affects both the LC RCS correction and 3D speed, or to error in the numerical spherical calculation. Nevertheless, the difference between VHF and UHF is extremely small (less than a factor of 2), which once again gives confidence in the spherical scattering solution.

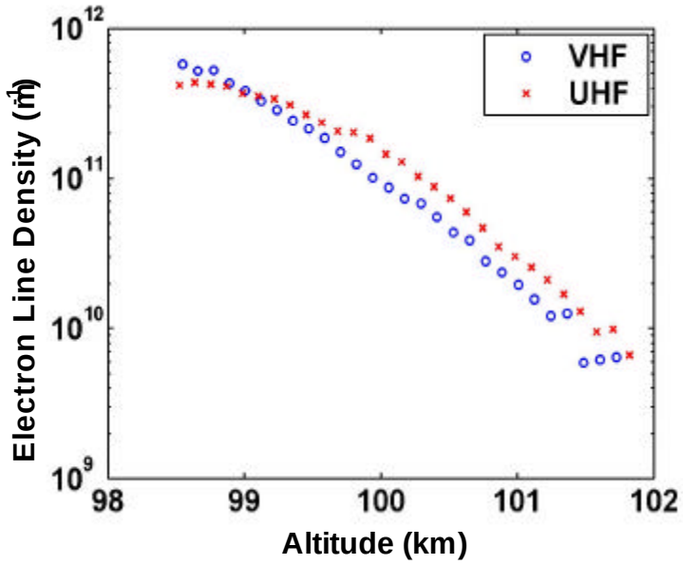

Figure 56. The electron line density calculated using the numerical spherical model applied to the LC RCS data contained in Figure 55.

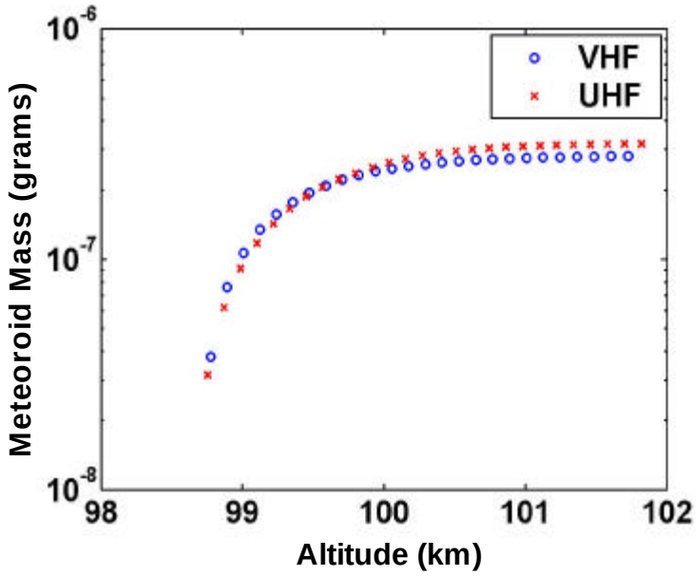

Figure 57. The meteoroid mass calculated using the electron line density shown in Figure 56.

We also examine all of the well-behaved head echoes detected simultaneously at VHF and UHF during the Leonid 1998 shower, in order to determine the differences between the VHF and UHF masses derived with our new scattering solution. These data total 90 head echoes. The ratio of VHF to UHF

mass ranges from 0.01 to 42.5, which a mean of 4 and a median of 2.2. These results illustrate the consistency of this new method for calculating meteoroid mass.

We proceed to calculate meteoroid masses for the 20 head echoes shown in Figure 32. These data are shown in Figure 58 and reveal the meteoroid mass as a function of altitude. Note how the meteoroids lose mass as altitude decreases, as expected, and that the highest mass loss rates occur at the lowest altitudes where the air densities are greatest. We also see a trend such that the highest mass meteoroids are located in the upper left portion of the plot, which corresponds to low altitudes. Since only the most massive meteoroids can penetrate to low altitudes, our new mass determination method appears consistent. Using the initial mass from each meteoroid, the median mass over all 20 meteoroids is 3.2×10^{-6} grams. We must be cautious in using the initial mass, however, as there exists a discrepancy between the low and high mass meteoroids. Specifically, the initial mass of the high-mass meteoroids, located at the lower altitudes, is probably correct since we see that the mass is hardly changing as a function of altitude, i.e. the curve is flat where we calculate the initial mass. The low mass meteoroids, however, show a distinct curvature at our first detected altitude. Therefore, we are undoubtedly underestimating the mass of the low-mass/high-altitude meteoroids.

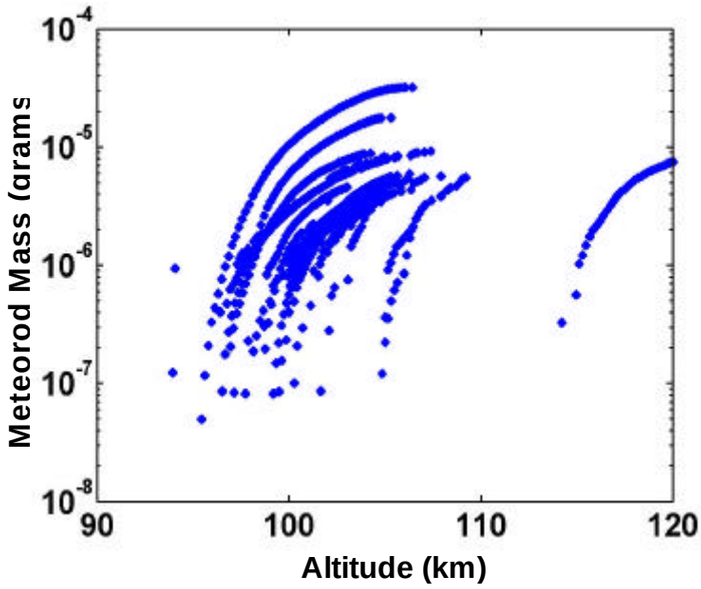

Figure 58. Meteoroid mass as a function of altitude for 20 VHF head echoes detected during the Leonid 1998 shower. These data use the 3D speed data shown in Figure 45.

We next compare how meteoroid mass, head echo speed and head echo electron line density depends upon altitude. We derive this dependence by using both the output from a single-body ablation model and the ALTAIR VHF data. First, electron line densities are modeled using the three-equation mass ablation model. *Hunt et al*. [2004] numerically integrated the meteoroid ablation model to illustrate the relationship between the initial mass, speed, and plasma production of meteoroids as a function of altitude. He used a constant meteor mass density of 2.5 g/cm^3 to produce modeled electron line densities for meteoroids with masses between 10^{-10} g and 10^{-4} g, and speeds between 11 and 72 km/s. First, the peak electron line density from each meteoroid streak is extracted and plotted as a function of altitude and speed, so that each point represents a single and separate meteoroid. Next, the peak electron line density is plotted as a function of altitude and meteoroid mass. These results are contained in Figure 59 and Figure 60 and are given in *Hunt et al.* [2004]. In Figure 59 we see that speed increases from the lower left (low altitudes) of the plot to the upper right (high altitudes). The dotted line represents the estimated sensitivity limit of the ALTAIR system, such that meteoroids to the left of that line will be undetectable by ALTAIR; we see this result in Figure 61. The results shown in Figure 59 are consistent with our earlier analysis, where we found that high-speed head echoes are detected at high altitudes. In Figure 60, we see that large-mass meteoroids are detected at altitudes that are lower than small mass meteoroids, which is an expected result since we believe that only the most massive meteoroids survive to reach the lower altitudes. In addition, higher mass meteoroids produce larger electron line densities than lower mass meteoroids, which is also intuitive since the amount of kinetic energy available for producing large electron line densities scales with meteoroid mass.

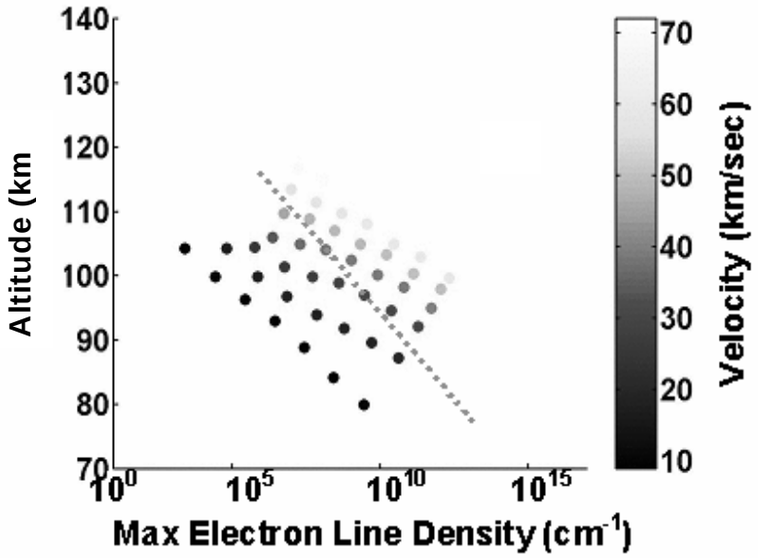

Figure 59. Electron line density as a function of altitude and meteoroid speed using the peak line density that is output from the single-body ablation model. The line denotes the sensitivity limit of the ALTAIR system.

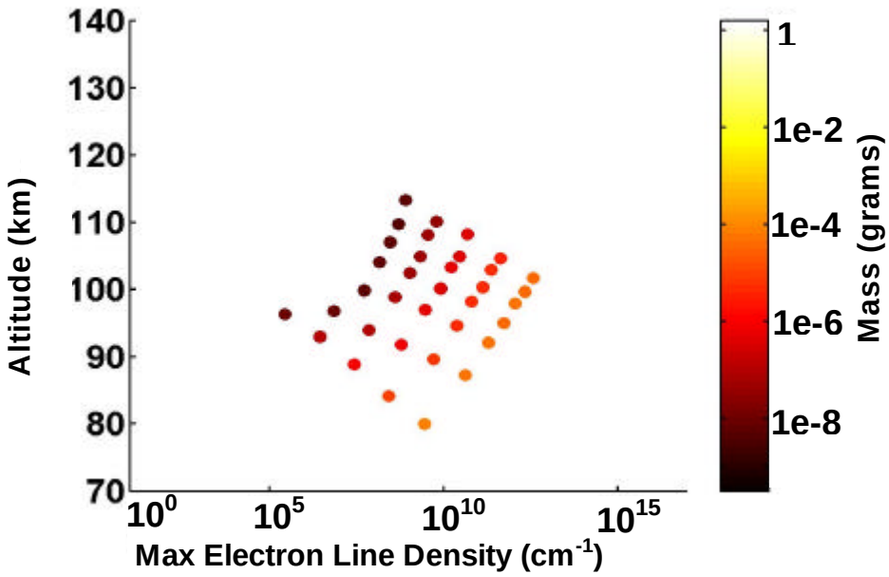

Figure 60. Electron line density as a function of altitude and meteoroid mass using the peak line density that is output from the single-body ablation model.

We now determine the dependence of meteoroid mass, 3D speed, and electron line density on altitude using 451 VHF head echoes collected by ALTAIR during the Leonid 1998 experiment. We

calculate the electron line densities by using the spherical solution to determine the maximum head plasma density from each head echo; we then apply Eq. 57 to the plasma density to determine line density. We calculate the meteoroid masses by using the electron line densities in Eq. 59, along with the measured 3D speeds. We emphasize that the spherical solution is applied only to the peak RCS of each of the VHF head echoes, and therefore each head echo streak (each meteoroid) is represented by only one data point. The measured line density dependence on altitude and 3D speed is given in Figure 61, and the measured line density dependence on altitude and meteoroid mass is given in Figure 62 [*Close et al.*, 2004]. It is clear that the general trend between Figure 59 and Figure 61 is the same, as well as the trend between Figure 60 and Figure 62. As mass and speed increases the electron line density increases. The smallest electron line densities correspond to meteoroids with low masses and low velocities, where the lowest masses are located in the upper left portion of Figure 60 (and Figure 62). Again, the spherical solution appears valid since it matches the theory described by the single-body ablation model rather well. More importantly, we are able to see clearly the radar selection effect of head echo detection. Radars are much less likely to detect meteoroids with low velocities and low masses because they create low electron line densities, and hence have low SNRs.

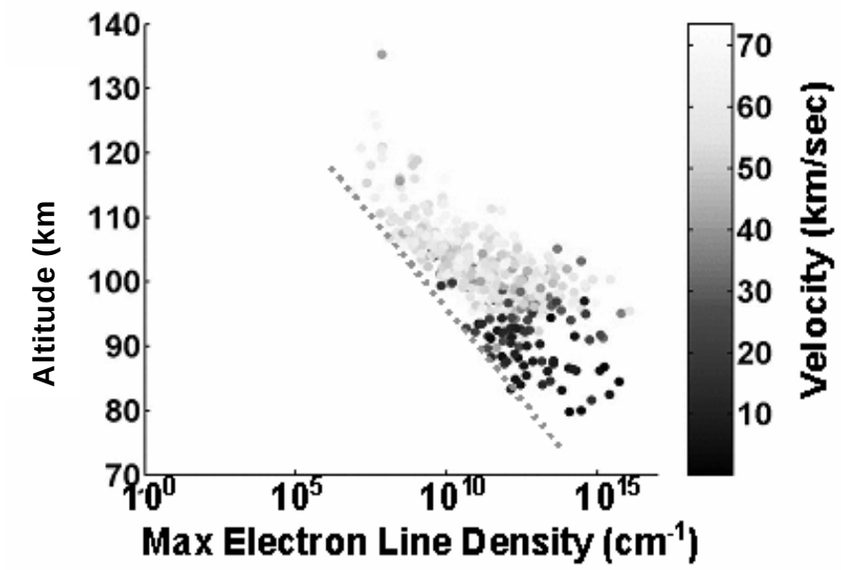

Figure 61. Electron line density calculated using the spherical model as a function of altitude and meteoroid mass using the peak RCS from 451 VHF head echoes from the Leonid 1998 shower. The line shows the sensitivity limit of the ALTAIR system.

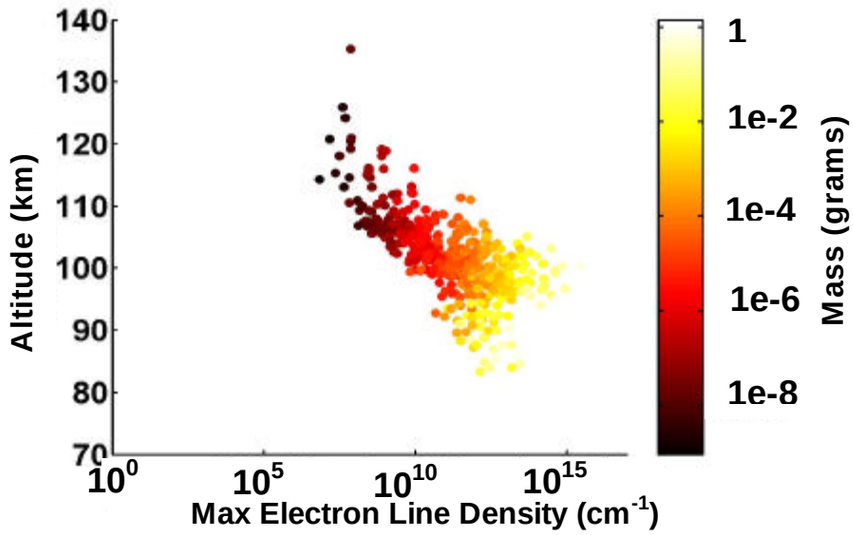

Figure 62. Electron line density calculated using the spherical model as a function of altitude and 3D speed using the peak RCS from 451 VHF head echoes from the Leonid 1998 shower.

We now examine the mass from each of the well-behaved head echoes detected during the Leonid 1998 and Leonid 1999 showers. We convert the maximum RCS value from each head echo to plasma density and then line density. We next convert line density to meteoroid mass using the 3D speed; therefore, the mass from each head echo is associated with the point of maximum RCS along that head echo streak. The histogram of meteoroid masses, calculated using the well-behaved VHF head echoes from the Leonid 1998 data set, is contained in Figure 63; these data include 451 points. The mean and median VHF meteoroid masses are 1×10^{-5} and 4.3×10^{-6} grams, respectively. The maximum meteoroid mass from all of the head echoes is 2.9×10^{-4} grams, and the minimum detected meteoroid mass is 1.4×10^{-7} grams.

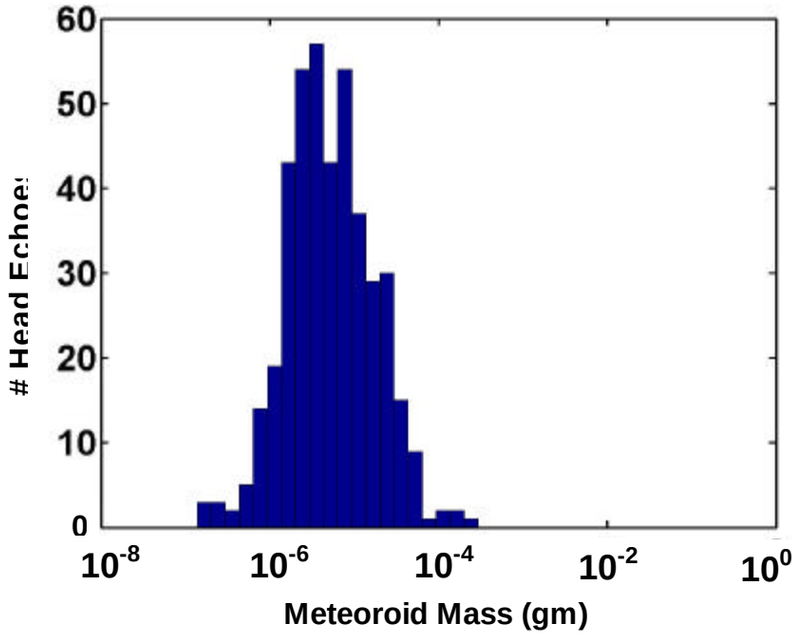

Figure 63. Histogram of maximum meteoroid mass calculated from 451 well-behaved VHF head echoes detected during the Leonid 1998 shower.

The histogram of maximum meteoroid mass associated with 223 well-behaved Leonid 1999 VHF head echoes is contained in Figure 64. The mean and median VHF meteoroid masses calculated using the Leonid 1999 data are 2.6×10^{-3} and 1.2×10^{-5} grams, respectively. The maximum meteoroid mass is 0.3 grams, while the minimum detected meteoroid mass is 2.1×10^{-7} grams.

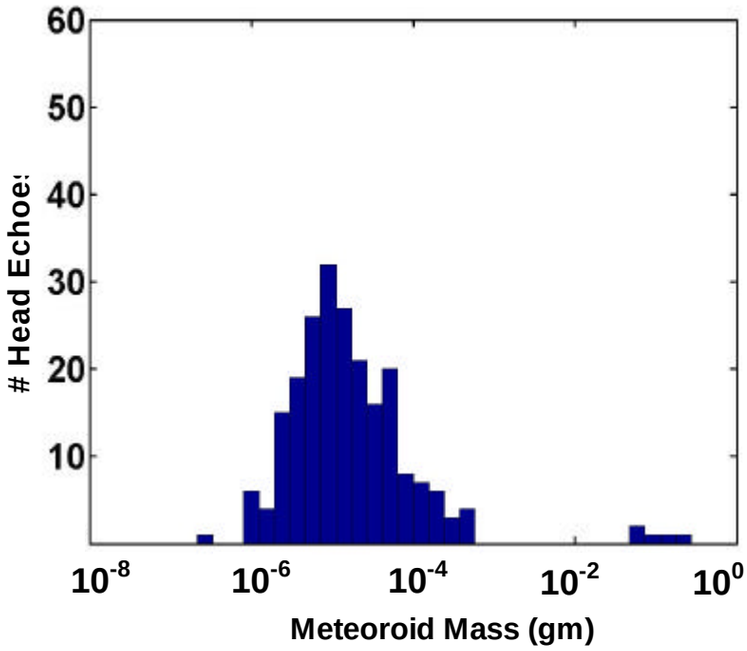

Figure 64. Histogram of maximum meteoroid mass calculated from 223 well-behaved VHF head echoes detected during the Leonid 1999 shower.

We conclude this section by determining the meteoroid masses using the 20:20 VHF GMT data file collected during the Leonid 1998 experiment. This data file, which was collected while pointing off-radiant, contains an unusually high number of particles traveling with 3D speeds that are > 73 km/s; these meteoroids comprise over 20% of the total number of well-behaved streaks, and over 11% of all of the head echo streaks. The 3D speeds, altitudes and meteoroid masses for these 34 meteoroids are plotted in Figure 65. These data indicate that the meteoroids with speeds > 73 km/s, which include 7 meteoroids, typically create head echoes at high altitudes; this result supports our earlier claim that high speed head echoes are created at high altitudes. These data also reveal that the high-speed meteoroids have relatively low masses, ranging from 10^{-6} to 10^{-9} gm. In addition, some of these particles did not create a simultaneous UHF head echo, even for those head echoes detected at an altitude lower than 110 km (limit of the UHF system in the Leonid 1998 experiment). When we examine the line densities of the interstellar particles, we find that the average interstellar line density is two orders of magnitude lower than the average line density from this file. These low line densities are no doubt due to the small masses of these interstellar particles and would preclude a UHF detection, regardless of detection altitude.

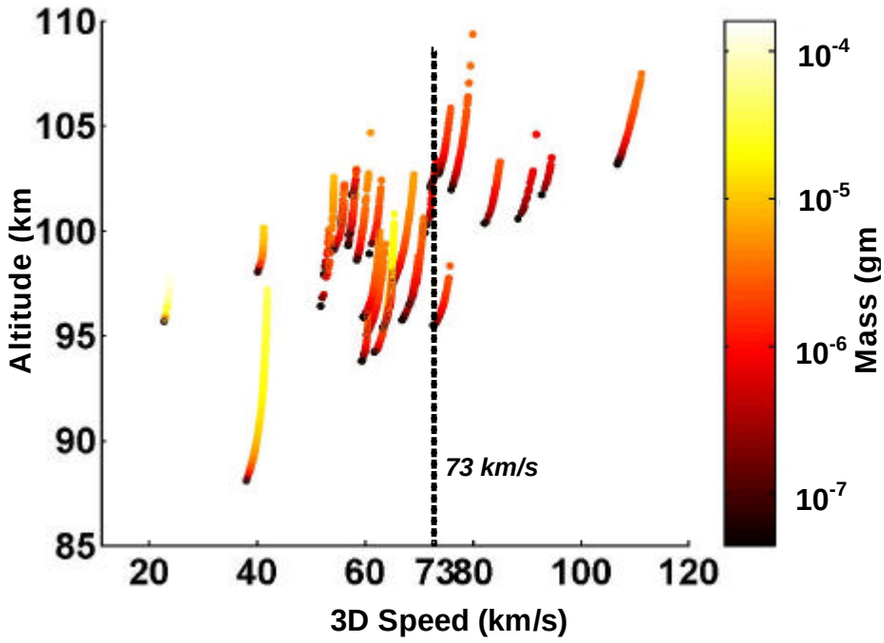

Figure 65. Meteoroid mass and 3D speed as a function of altitude using the Leonid 1998 VHF data collected at 20:20 GMT. The solid line corresponds to 73 km/s.

2.6.1 Ionization Probability

We now compare various ionization probabilities in order to determine its effect on meteoroid mass. As noted earlier, we use the Jones' formula for ionization probability, which scales as approximately $v^{2.8}$ [*Jones*, 1997] In comparison, the Lebedinets' formula [*Lebedinets et al.*, 1973] scales as $v^{3.5}$, and the Bronshten formula [*Bronshten*, 1983] scales as $v^{3.42}$. On average, we find that the Lebedinets and Jones formulas closely match and are typically less than a factor of 2 different. The Bronshten formula, in contrast, varies from a factor of 5 difference in mass, to over a magnitude difference. A comparison of the 3 formulas using two UHF head echoes detected during the Leonid 1998 shower is contained in Figure 66. The top head echo has a mean 3D speed of 30 km/s, and the bottom head echo has a mean 3D speed of 60 km/s. We found no correlation between head echo speed and error in the ionization probability formulas, i.e. the Lebedinets and Jones formulas always provided very similar masses.

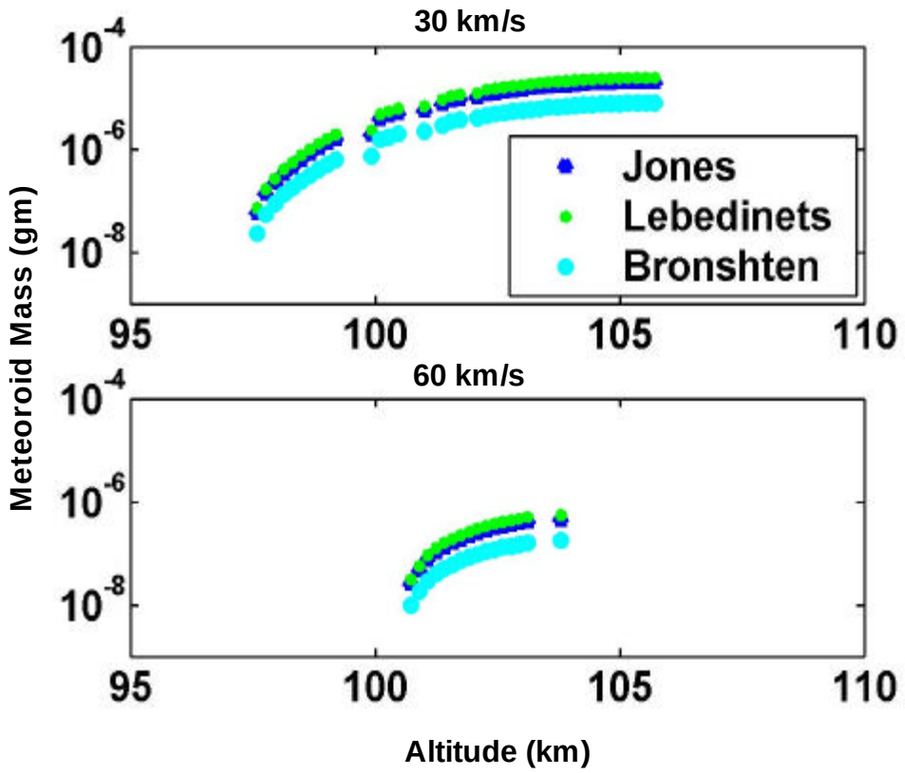

Figure 66. Meteoroid mass vs. altitude for a UHF head echo moving at 30 km/s, and a UHF head echo moving at 60 km/s. Data were collected during the Leonid 1998 shower.

2.6.2 Comparison with Masses Derived using the Ballistic Parameter Equation

As a meteor descends through earth's atmosphere, it encounters an air mass dm equal to $A?_{air}vdt$ [*Opik*, 1958] in the interval dt, where A is the meteoroid's physical cross section, v is the meteoroid speed, and $?_{air}$ is the mean atmospheric density, which we calculate here using the MSIS-90 atmospheric model. We ignore any fragmentation of the meteoroid body. Therefore, the meteoroid momentum reduction per unit time is

$$\frac{dv}{dt} ? \frac{A??_{air}v^2}{m} \qquad \textbf{(60)}$$

where dv/dt is the meteoroid deceleration, m is the meteoroid mass and $?$ is the dimensionless drag coefficient, which we typically set as one. The speed is further defined by

$$v \approx \frac{dh/dt}{\cos \zeta} \tag{61}$$

where h is the altitude, dh/dt is the derivative of altitude with respect to time, and ζ is the elevation angle. By substituting Eq. 61 into Eq. 60, we obtain the ballistic parameter,

$$\frac{m}{A} \approx \frac{v^2 \cos \zeta}{dv/dh} \tag{62}$$

where dv/dh is the change in meteoroid speed with altitude. The meteoroid's ballistic parameter, which is the ratio of the meteoroid mass to cross-section, can be used to estimate meteoroid masses by assuming meteoroid density. However, as noted by *Evans* [1966], as well as *D. Janches* [private communication], this formula will sometimes produce unphysical results. For instance, if we examine a single head echo streak, the ballistic parameter of the meteoroid will often increase and then decrease, instead of consistently decrease as it penetrates further down in altitude, as we would expect. We attribute this anomalous behavior either to fragmentation processes, which we ignore in the single-body theory used to derive the ballistic parameter equation, or to excluding the second-order terms in the equation, which may be important.

We now include a comparison of mass determination using our new scattering method (i.e. "scattering mass") with mass determination using the ballistic parameter equation (i.e. "deceleration mass") in order to evaluate the methods. We extract 10 UHF head echoes detected during the Leonid 1998 shower with well-behaved 3D speeds and compute mass using both methods. Again, in order to compute deceleration mass using the ballistic parameter equation, we must assume the meteoroid's density. We choose the meteoroid densities to be 1.4 gm/cm^3, which we derived using our scattering model for the Leonid 1998 data; this density is also consistent with the density of a cometary particle. These data are plotted in Figure 67 and Figure 68 and are grouped according to agreement between the two mass-determination methods. Figure 67 contains head echoes that agree, on average, to within a factor of 5, and Figure 68 contains head echoes that agree, on average, to within a factor of 50. Using all 10 head echoes, the mean ratio of scattering to deceleration mass is 9.6, with the scattering method typically producing the higher mass. Two general points are worth noting when examining these figures. The first is that the deceleration masses often do not intuitively follow our physical intuition, where we believe highest mass-loss rates should occur at the lowest altitudes. Specifically, many of the deceleration masses are straight lines. Second, the deceleration masses do not follow the same trend

with altitude as the scattering masses, where higher mass meteoroids are detected at progressively lower altitudes.

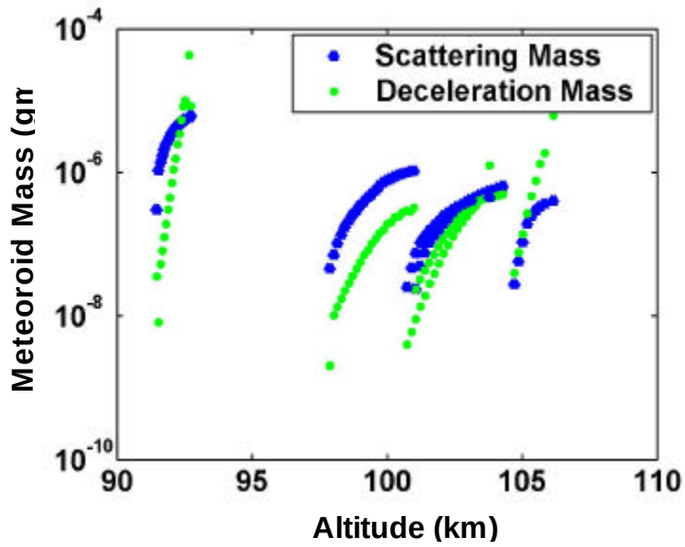

Figure 67. Five UHF head echoes detected during the Leonid 1998 shower showing scattering and deceleration mass. The average ratio between the scattering and the deceleration mass for these five head echoes ranges between 1.4 to 4.9.

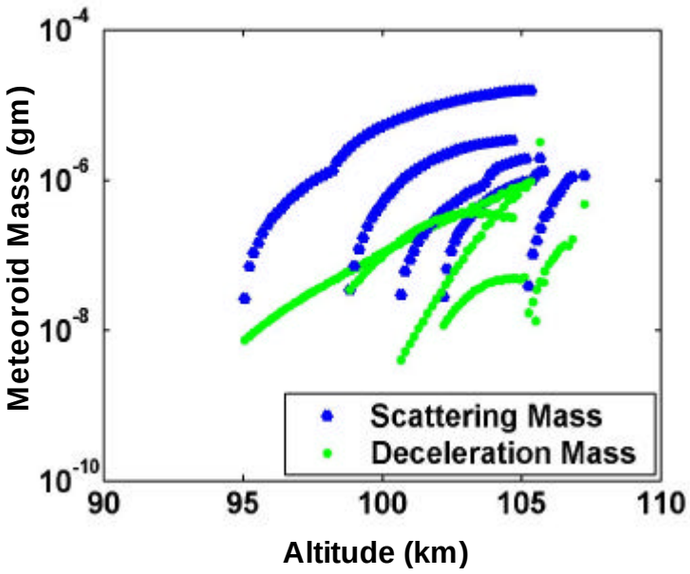

Figure 68. Five UHF head echoes detected during the Leonid 1998 shower showing scattering and deceleration mass. The average ratio between the scattering and the deceleration mass for these five head echoes ranges between 5.6 to 50.

2.7 Discussion and Caveats

We have mentioned a number of caveats that we must consider when analyzing and utilizing these data. For the purpose of clarity, we revisit these issues.

First, the monopulse data, which allows us to calculate 3D velocity and deceleration, has errors that are higher than the other measured parameters, such as range rate or RCS. This is mainly because we kept the boresite stationary and allowed head echoes to travel through the main beam and sidelobes, which is outside the linear regime where the calibration constants are valid. In addition, head echoes are distributed plasmas, unlike satellites, which may pose a problem for the amplitude-comparison method used to calculate monopulse data. Therefore, the errors on the 3D velocities are higher than on the range rates.

Second, we utilize the monopulse data and the beam pattern data to correct the measured head echo's RCS for location within the beam. However, a combination of error on the monopulse, and the lack of a complete beam pattern, means that our RCS correction is sometimes in error. Recall that we utilize RCS to determine plasma density, which is used to determine meteoroid mass.

Third, the high ionization efficiencies associated with high-speed head echoes causes these fast particles to be detected at high altitudes; recall that we found speed to scale with height. This, in addition to our pointing primarily at the North Apex source, means we are much more likely to detect high-speed meteoroids. Concurrently, our altitude sampling at VHF, which spanned 70 to 140 km, was greater than our sampling at UHF, which spanned 90 to 110 km (using the U150 waveform). Therefore, we are more likely to detect fast particles at VHF than at UHF. All of these issues mean we must be cautious in utilizing these data to estimate a speed distribution for the entire meteoroid population.

Fourth, as we have shown through our analysis, there exists a strong dependence between a meteoroid's speed, mass, line density, and altitude. Specifically, fast/small meteoroids will be detected at high altitudes, while slow/large meteoroids will be detected at low altitudes. High line densities, which correlate to high RCS values, are associated with large and high-speed particles. Due to the nature of head echo detection, we are therefore much more likely to sample particles with high speeds and large masses, since these particles will produce RCS values above the radar's minimum sensitivity.

Finally, while we believe that we have developed the most precise method for determine meteoroid mass from head echo data, there remains a few areas that can be improved. We must estimate an ionization probability in order to determine meteoroid mass, yet there is no clear evidence supporting one method over another. Also, we must assume that the meteoroid deposits all of its ionization while we are detecting it in order to calculate a meteoroid mass, yet it is clear that meteoroid mass loss most probably occurs prior to and after the head echo is detected by ALTAIR. This would result in an underestimation of mass for low-mass particles.

Bibliography

Blake, L. V.: "Radar Range-Performance Analysis." Artech House, Norwood, Mass, 1986.

Bronshten, V. A.: "Physics of Meteor Phenomena." D. Reidel Publ. Co., Dordrecht, Holland, 1983.

Brown, P., S. Hunt and S. Close: Astronomical and physical data for meteoroids recorded by the ALTAIR radar. *Proceedings of the Meteoroids 2001 Conference*, ESA SP-495, 2001.

Campbell, M.: private communication.

Close, S., M. Oppenheim, S. Hunt and A. Coster: A technique for calculating meteor plasma density and meteoroid mass from radar head echo scattering. *Icarus*, (**168**):43-52, 2004.

Close, S., S. Hunt, M. Minardi and F. McKeen: Characterization of Leonid meteor head echo data collected using the VHF/UHF Advanced Research Projects Agency Long-Range and Tracking Radar. *Radio Sci.*, 37, 2002.

Close, S., S. Hunt, M. Oppenheim and L. Dyrud: Scattering characteristics of high-resolution meteor head echoes detected at multiple frequencies. *J. Geophys, Res.*, 107, 2002.

Close, S., S. Hunt, M. Minardi and F. McKeen: Analysis of Perseid meteor head echo data collected using ALTAIR. *Radio Sci.*, (**35):**1233-1240, 2000.

Evans, J. V.: Radar observations of meteor deceleration. *J. Geophys. Res.*, (**71**):171-188, 1966.

Herlofson, N., Plasma resonance in ionospheric irregularities, *Arkiv for Fysik*, 247-297, 1951.

Hunt, S. M., M. M. Oppenheim, S. Close, P.G. Brown, F. M. McKeen and M. Minardi: Determination of the meteoroid speed distribution at the Earth using high-gain radar. *Icarus*, (**168**):34-42, 2004.

Jackson, J. D.: "Classical Electrodynamics." John Wiley & Sons, Inc., 1975.

Janches, D.: private communication.

Jones, W.: Theoretical and observational determinations of the ionization coefficient of meteors. *Mon. Not. R. Astron. Soc*, (**288**):995-1003, 1997.

Jones, J., and W. Jones: Oblique-scatter of radio waves from meteor trains: calculations. *Planet Space Sci*, (**9**):1289-1296, 1991.

Jones, J., and A. R. Webster: Visual and radar studies of meteor head echoes. *Planet Space Sci.*, (**39**): 873-878, 1991.

Kaiser, T. R. and R. L. Closs: Theory of radio reflections from meteor trails. I, *Journal of Theoretical Experimental and Applied Physics*, 43, 1951.

Knott, E. F., J. F. Shaeffer and M. T. Tuley: "Radar Cross Section." Artech House, Inc., 1985.

Lebedinets, V. N., A. V. Manochina and V. B. Shushkova: Interaction of the lower thermosphere with the solid component of the interplanetary medium. *Planet Space Sci*., (**21**):1317-1332, 1973.

Levanon, N.: "Radar Principles." John Wiley & Sons, Inc., 1988.

Mathews, J. D., D. D. Meisel, K. P. Hunter, V. S. Getman, and Q. Zhou: Very high resolution studies of micrometeors using the Arecibo 430 MHz radar. *Icarus*, (**126**):157-169, 1997.

McIntosh, B. A.: On the end point of fireballs. *J. Roy. Astron. Soc. Ca*., (**64**):267-281, 1970.

Mie, *Ann. Physic*, (**37**):511, 1912.

Morse, P. M. and H. Feshbach: "Methods of Theoretical Physics, Part II." McGraw-Hill, Inc., 1953.

Opik E. J.: "Physics of Meteor Flight in the Atmosphere." Interscience Publishers Inc., 1958.

Poulter, E. M. and W. J. Baggaley: Radiowave scattering from meteoric ionization. *Journal of Atmospheric and Terrestrial Physics*, (**39**):757-768, 1977.

Sherman, S. M.: "Monopulse Principles and Techniques." Artech House, 1984.

Slolnik, M. I.: "Introduction to Radar Systems." McGraw-Hill, 344, 2001.

Stratton, J. A.: "Electromagnetic Theory." McGraw-Hill Book Company, 1941.

Toomay, J. C.: "Radar Principles for the Non-Specialist." SciTech Publishing, Inc., 102, 1998

Wannberg, G., A. Pellinen-Wannberg, and A. Westman: An ambiguity-function-based method for analysis of Doppler decompressed radar signals applied to EISCAT measurements of oblique UHF-VHF meteor echoes. *Radio Sci*. (**31**):497-518, 1996.

Zhou, Q.-H., P. Perillat, J.Y.N. Cho, and J.D. Mathews: Simultaneous meteor echo observations by large aperture VHF and UHF radars. *Radio Sci.*, (**33**):1641-1654, 1998.

3. ORBIT AND BULK DENSITY ANALYSIS BACKGROUND

It is generally accepted that sporadic meteors are the products of the disintegration of cometary nuclei which have been dispersed to the point of no longer being associated with their respective parent cometary body (cf. Jacchia 1963). Asteroidal particles may also contribute some unknown fraction of the total meteoroid population (cf. Grogan et al., 2001). Cometary theory developed by Whipple (1950, 1951) describes comets by the so called ‘dirty snow ball’ or ‘icy dust ball’ model. According to this model cometary nuclei are conglomerates of ices (H_2O, NH_3, CH_4, CO) and meteoric material (Whipple 1950). Based on this cometary model, Jacchia (1955) developed what has come to be known as the dustball theory of meteoroids. According to this model, meteoroids have a composite structure of grains embedded in a matrix of lower boiling point material, often referred to as the ‘glue’ (Hawkes and Jones 1975). Independent modeling of interstellar dust grains has produced a similar physical picture as summarized by Greenberg and Hage (1990). Figure 69 shows the resulting physical model for interstellar dust grains, the basic form of which is expected to also apply to cometary meteoroid grains, since these are believed to be formed from largely unprocessed volatile condensates (including interstellar grains) from the early solar nebula.

Hawkes and Jones (1975) further developed an ablation model based on the dustball theory of meteors. In this model, when a meteoroid enters the atmosphere it is heated via collisions with air molecules. When the surface temperature of the meteoroid reaches that of the boiling point of the matrix material, the ‘glue’ can evaporate. In the absence of the ‘glue’, the meteoroid is a very porous collection of dust grains, up to 50% of its volume may be taken up by air (Gustafson, 1994) which can then fragment. During fragmentation dust grains will be ejected from the meteoroid which will then ablate according to the classical physical theory of meteors (Beech 1984).

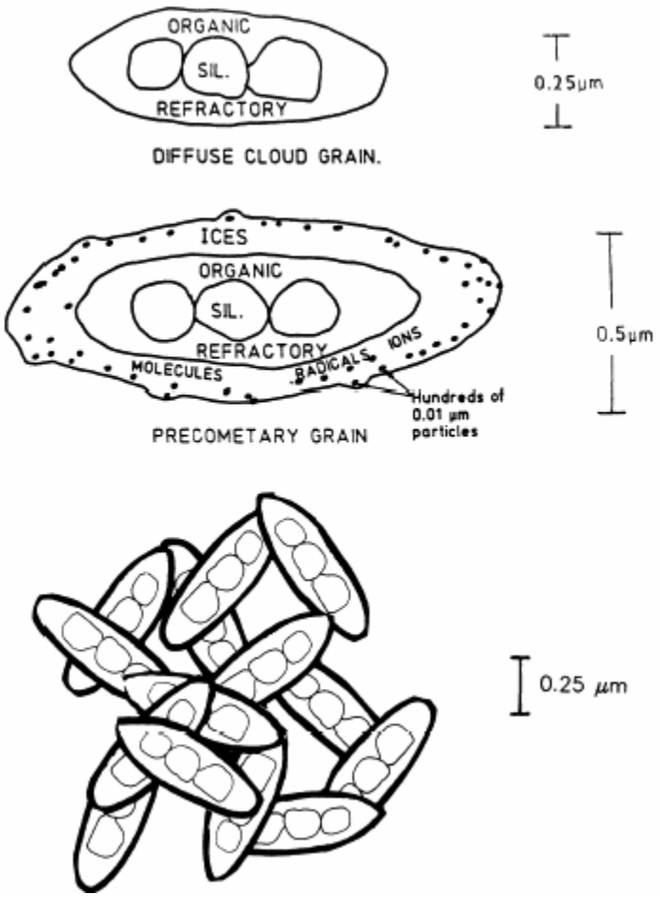

Composite grain “dustball” meteoroid

Figure 69. Greenberg model of an interstellar dust grain. This physical model is also expected to apply to cometary meteoroids, believed to be made of interstellar grain and ice materials.

3.1 The Classical Physical Theory of Meteors

The classical physical theory of meteors, which describes the motion and ablation of meteoroids via a series of differential equations, is based on aerodynamic ballistics and plausible assumptions about atomic collisions and light-emission processes (McKinley 1961). The equations treat meteoroids as single, solid bodies and are also known as the equations of single body theory. The principal equations of this theory describe the deceleration, mass loss, luminosity and ionization that occur for a meteoroid when it enters the earth’s atmosphere. One assumption of the classical physical theory of meteors is that

the coefficients of drag, heat transfer, luminosity and ionization are constant and that the meteoroid ablates as a single, monolithic object.

The drag equation describes the deceleration of the meteoroid as a result of collisions with air molecules. It is derived by equating the momentum lost by the meteoroid with that gained by the impinging air molecules.

$$\frac{dv}{dt} = -\Gamma A \rho_d^{-2/3} \rho_a m^{-1/3} v^2 \quad \textbf{(63)}$$

where Γ is the dimensionless drag coefficient, A is the dimensionless shape factor, ρ_d is the bulk density of the meteoroid, ρ_a is the atmospheric density, m is the meteoroid mass, and v is the meteoroid velocity. The drag coefficient Γ describes what fraction of momentum of the oncoming flow is converted into the deceleration of the meteoroid (Bronshten 1983). The case when $\Gamma < 1$ corresponds to an incomplete transfer of momentum, whereas the case when $\Gamma > 1$ corresponds to the situation when the momentum of either the air molecules rebounding off of the meteoroid or of the ablated meteoric molecules becomes appreciable (Bronshten, 1983). For smaller meteoroids $\Gamma < 1$ generally holds.

The mass loss equation is derived by equating the rate of mass loss of the meteoroid with the kinetic energy transferred to the intercepted air mass.

$$\frac{dm}{dt} = -\frac{\Gamma A}{2\xi}\left(\frac{m}{\rho_d}\right)^{2/3} \rho_a v^3 \quad \textbf{(64)}$$

where Γ is the heat transfer coefficient, ξ is the energy necessary for ablation of a unit mass, A, ρ_d, ρ_a m, and v are defined above in the drag equation.

The ionization equation finds the number of free electrons produced per unit path length. It is derived using the assumption that the power required for ionization production is proportional to the kinetic power lost by the ablated atoms.

$$q = -\beta_q \frac{\Gamma A}{4\xi}\left(\frac{m}{\rho_d}\right)^{2/3} \rho_a v^4 \quad \textbf{(65)}$$

where q is the electron line density (m^{-1}), t_q is the ionization efficiency factor, ? is the mean ionization potential per atom involved, ? , A, ?, $?_d$, ?, m, and v are all defined as above.

The shape of the meteoroid is not necessarily constant over its atmospheric flight. The shape factor which appears above in the drag, mass loss, and ionization equations describes the instantaneous geometrical shape of the meteoroid.

$$A ? Sm^{?2/3} ?_d^{2/3} \quad \textbf{(66)}$$

where S is the cross-sectional area of the meteoroid. The shape factor of a sphere is

$$\left(\frac{9?}{16}\right)^{1/3}$$

(McKinley 1961) or approximately 1.21.

As stated earlier, it is generally accepted that the majority of meteoroids are of the crumbling dustball type. The ‘neoclassical’ physical theory of meteors is based on the equations of classical physical theory (McKinley 1961), and incorporates the crumbling nature of meteoroids. However, it has not been sufficiently developed into a convenient form for use in this analysis. To do so requires additional parameters and assumptions about the properties of the constituent grains before deeper analysis is possible.We have, however, tried to empirically account for fragmentation through fitting of the parameter of shape-variation (?) as described below.

3.2 Theory

This analysis begins with the drag equation (63). By rearranging for bulk density and letting

$$v ? \frac{dv}{dt} \quad ,$$

we find

$$?_d ? \frac{v^3}{m^{1/2}} \left(? \frac{?A?}{v}\right)^{3/2} \quad \textbf{(67)}$$

We assume that the initial shape of the meteoroid is spherical and it is allowed to change throughout its atmospheric flight in a dynamic manner.

$$A = A_0 \left(\frac{m}{m_0} \right)^{\mu} \tag{68}$$

where A_0 is the initial shape factor of the meteoroid, with a value of 1.21, m_0 is the initial mass of the meteoroid, and μ is the parameter of shape variation. If the meteoroid (assumed to be spherical to start with) remains self-similar as it ablates, μ has a value of 2/3; if the meteoroid is flattened such that its midsection increases faster than the axis along the line of flight as mass is lost (a situation referred to as 'pancaking') then $\mu < 1$ (Bronshten 1983). The parameter μ corresponds physically to a parameter which accounts for the change in shape during ablation. This is normally applicable to larger meteoroids. Here we interpret μ as a parameter which is used to account for fragmentation processes. By minimizing the pulse-by-pulse residuals in density through variation in μ, we can attempt to empirically account for fragmentation, as suggested by Levin (1956).

It is also assumed that the momentum transfer from the oncoming air flow to the meteoroid is complete, thus G = 1. By substituting (6) and G = 1 into equation (67), we find

$$\rho_d = \rho A_0 \left(\frac{m}{m_0} \right)^{\mu} \left(\frac{\rho}{v} \right)^{3/2} m^{-1/2} v^3 \tag{69}$$

Bulk density is calculated at each radar pulse return and the parameters which are needed for these calculations are mass, air density, velocity and acceleration. To perform an independent measure of the bulk density at each radar return we need to measure the velocity, change in velocity (deceleration), estimate the air density and independently recover mass without using deceleration measurements (so called dynamic mass, cf. Ceplecha et al. (1998)). The detailed procedure followed to accomplish this and thus solve eq (7) is described below.

3.3 Data Analysis

Processing begins by first extracting raw data as calibrated by the Lincoln Lab group (see earlier section of report). Data arrives in the form of an ASCII text file with thirty three columns of data and one line of data for each radar pulse return. Note that the radar produces 333 pulses per second. Typical meteor head echoes last <100 ms in the beam and hence we have a few dozen pulsed returns to measure for a portion of the trail. In most cases the data which are used in this analysis are: the time of each radar

pulse return, meteoroid position components, velocity components, electron line density and meteoroid masses. The latter two quantities are computed from the RCS of the head echo based on the scattering theory and overdense theory as described in the Section 2 of the report.

The time of each radar pulse return arrives in the form of seconds since midnight on the day of observation and is adjusted so each meteor begins at time zero. The meteoroid position components are given in Cartesian coordinates, where x is in km east of ALTAIR, y is in km north of ALTAIR, and z is in km above ALTAIR. The meteoroid velocity components are given, where $\frac{dx}{dt}, \frac{dy}{dt}, \frac{dz}{dt}$ are the x, y and z components of velocity. Two masses are given for each meteoroid at each radar pulse return, one derived using the three dimensional full wave scattering theory, the other using overdense scattering theory.

Each meteor is then analyzed as follows. A linear least square fit of meteoroid position data is made. The residual, the distance from the data point to the fitted meteoroid path, is calculated for each data point, as well as the standard deviation of the residuals. The first criterion for the rejection of data points is the magnitude of the residuals. Data points whose residuals are greater than three times the standard deviation are rejected. After data rejection the linear least squares fit is redone, and the meteoroid path vector is determined.

The instantaneous velocity is calculated for each radar pulse return using

$$v ? \sqrt{? \frac{dx}{dt} ?^2 ? ? \frac{dy}{dt} ?^2 ? ? \frac{dz}{dt} ?^2} \quad \textbf{(70)}$$

and a polynomial fit is made to this function. Though the instantaneous velocity is often quite well behaved, making a fit to these data serves to minimize errors due to ALTAIR's range resolution. Figure 70 shows the fit to the instantaneous velocity. From the polynomial fit an analytic expression is found for velocity as a function of time. This analytic expression is evaluated at the time of each radar pulse return and the value is used for the velocity component (v) in the the bulk density calculation, equation (69). The strength of this fit is that it uses all good data points to find the best-fit representation for the change in velocity with time. Note, in particular, that we find substantial deviation from linear deceleration for most of the echoes detected in contrast to the results found from Arecibo measurements

(Janches et al.,2000). We suggest that this is because Arecibo sees a much smaller portion of the overall trails than ALTAIR and hence it “sees” only a small linear portion of the deceleration profile.

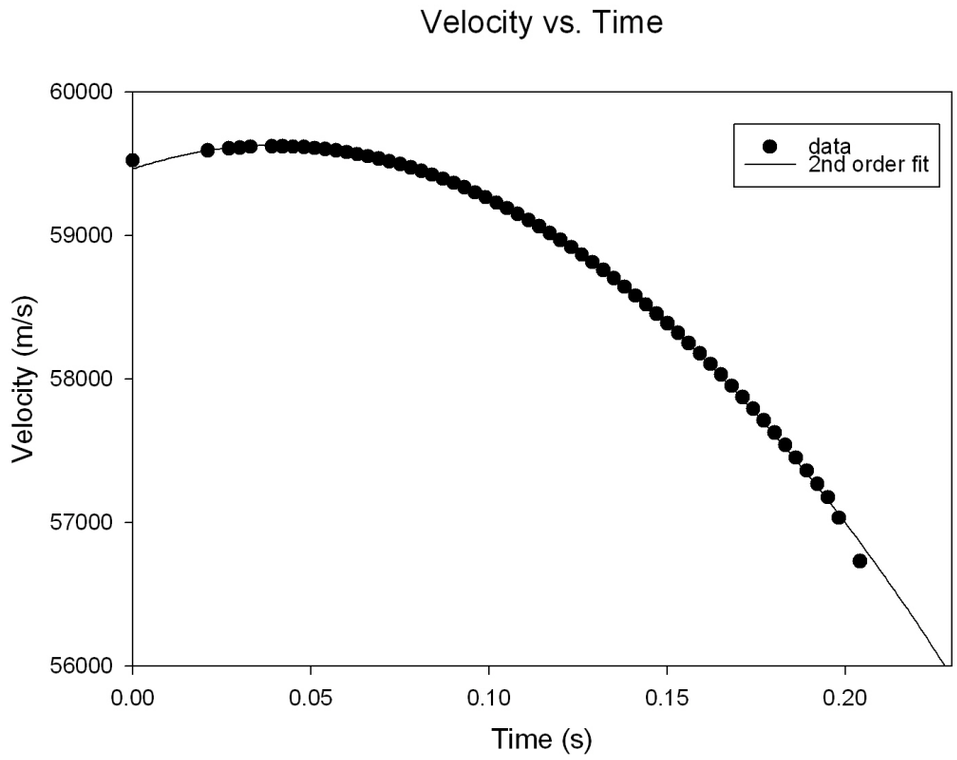

Figure 70. Instantaneous velocity and second order fit to data.

An analytic expression for meteoroid acceleration is found by differentiating the analytic expression for velocity as a function of time. Like velocity, this equation is evaluated at the time of each radar pulse return, and the value is used for the acceleration component (dv/dt) in the bulk density calculation, equation (69). A second criterion applied to data before densities are measured is based on the sign of the acceleration of the meteoroid. As the meteoroid enters the atmosphere, collisions with air molecules will cause the meteoroid’s acceleration to decrease. However, many head echoes show an apparent initial increase in acceleration before the expected decrease. This effect has been observed for head echoes by Close (2004) in approximately 10% of ALTAIR observations. We interpret this effect as being un-physical, possibly related to the delay in formation of the scattering center for the head echoes at high altitudes. The data points which correspond to increasing meteoroid acceleration are rejected before further processing occurs.

In addition to the kinematic data measured for each head echo, atmospheric density is required to infer bulk density. Atmospheric data files were used to provide air density at 1 km height increments from both the Marshall Engineering Thermosphere (MET) model, and the Global Reference Atmospheric Model (GRAM) (cf. Justus and Johnson, 1997 for details of these models). A separate atmosphere file was generated for each observation period. The average value of the two models at each height was used in all calculations. Air density plotted as a function of height is an exponential curve which we linearize by making a polynomial fit to the log(air density) vs. height. Again an analytic expression is found for the logarithm of air density as a function of height from which the atmospheric density at the height of each radar pulse return can be evaluated and used for the air density component (?) in the bulk density calculation, equation (69).

The parameter of shape variation (μ) is treated as a free mathematical parameter. All of the calculated and known quantities, A_0, m_0, m, v, V, and ? are substituted into the equation for bulk density, equation (69), and μ is varied between -2 and 2 in increments of 0.01. Bulk density is calculated for each radar pulse return of the meteor, and the standard deviation of these densities is determined. The optimal μ is chosen such that the standard deviation in the densities from point to point for the entire observed trail is a minimum. The overall bulk density of the meteoroid is taken to be the average bulk density from all the radar pulse returns. This procedure is designed to minimize the effects of fragmentation on the density determination. Figure 71 shows the effect on the density residuals as a function of time, of variation in μ.

The final parameter needed to evaluate equation (69) is meteoroid mass. Masses were found using the 3D full-wave scattering theory and a simplified overdense scattering treatment as described in detail in section 2 of this report based on the RCS measurement of each head echo return pulse.

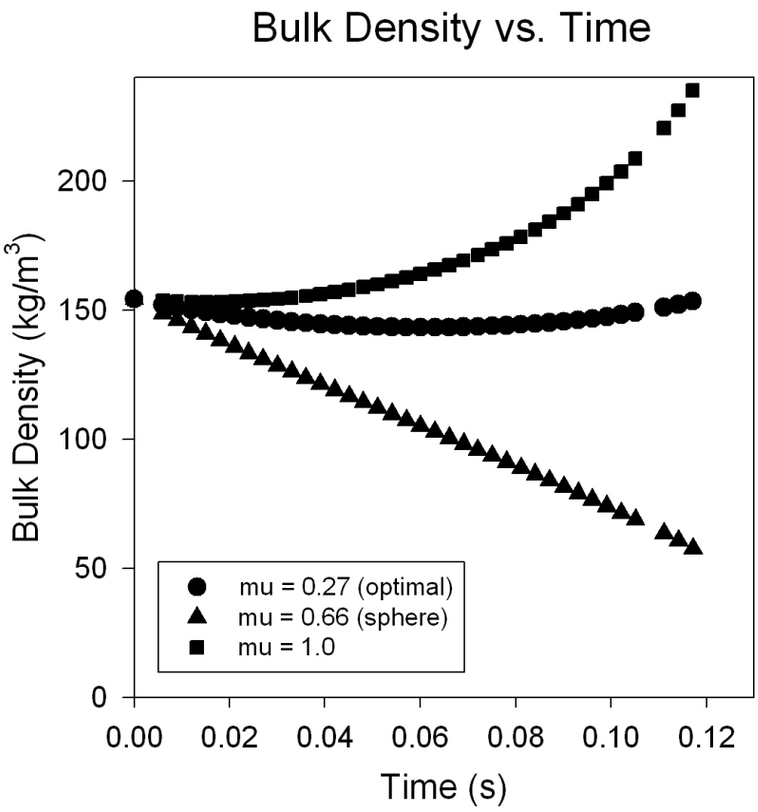

Figure 71. Bulk density calculated using three values of μ.

With all the unknown parameters in equation (69) now determined (on a per pulse basis) the final measure for density (again on a per pulse basis) is then computed.

3.4 Analysis – Orbits

A Fortran program based on the approach of Ceplecha (1987) is used to calculate meteoroid orbits. The parameters which are used as input to this program are: the date and time of observation, geographic latitude, longitude and height above sea level of observation site, pre-atmospheric velocity of the meteoroid, average velocity along the visible portion of the trail of the meteoroid, and the equatorial coordinates of the apparent radiant.

The pre-atmospheric velocity is our measured velocity with a small correction applied to account for deceleration by the atmosphere in the earliest portion of the trajectory. The precise form of this

correction is highly uncertain as virtually no measurements on known initial velocities (ie shower meteors) at the particle sizes probed by ALTAIR have been made. Thus we apply an approximate correction using the theoretical approach described by Baggaley et al. (1994). This correction is calculated by applying a correction to the velocity at the point on the meteoroid's path where electron line density is a maximum. The form of the correction is:

$$v_? \; ? \; \sqrt{v^2_q \; ? \; 0.81 v_q^{\;1.6}} \qquad \textbf{(71)}$$

where $v_?$ is the pre-atmospheric velocity of the meteoroid, and v_q is the instantaneous velocity of the meteoroid at the point of maximum electron line density.

The horizon coordinates (altitude and azimuth) of the meteor's apparent radiant are readily determined with the meteor path unit vector. These are then converted into equatorial coordinates (right ascension and declination). The 3D trajectory is determined through use of a 3D linear least-squares fitting routine applied to the original x,y,z data with an outlier rejection routine set to reject point which are more than 3 standard deviations from the mean path.

3.5 Results and Discussion

In total, densities were determined for 1029 meteoroids, 203 meteors were observed with UHF and 826 with VHF. This data, which was collected on 21 separate pointings constituting approximately 36 minutes of UHF data and 70 minutes of VHF data.

Some unphysically high densities were calculated, which greatly skew the standard deviation of the densities. The bulk densities calculated using the masses determined by full wave scattering theory (3D densities) were found to have a mean value of 6000 ± 13000 kg/m^3 for the 203 UHF meteors and a mean value of 7000 ± 55000 kg/m^3 for 826 VHF meteors. The bulk densities calculated using the masses determined from overdense scattering theory (Ovr densities) were found to have a mean value of 5000 ± 12000 kg/m^3 for the 203 UHF meteors and a mean value of 6000 ± 46000 kg/m^3 for the 826 VHF meteors.

It is clear that the few extremely high densities are unrealistic. The most common “dense” material which we might remotely expect a meteoroid to be wholly (or more likely partially) composed is Nickel-Iron. Pure Ni-Fe has a density near 8000 kg/m3. On physical grounds, we can safely assume that anything higher than this value is much more likely to be an error (probably with the monopulse measurements). In particular, the low number of data points makes a very low value in deceleration to be registered in error.

Figures (72) and (73) clearly show a correlation between the extreme high density values and low number of data points within the dataset of 203 UHF and 826 VHF observations respectively. Densities calculated using masses from the three dimensional full-wave scattering theory are represented by 3D Mass, densities calculated using masses from overdense scattering theory are represented by Overdense Mass.

Note that by virtue of the scattering processes involved, the UHF echoes are all observed for a much smaller portion of the total trail length and thus we expect to observe much less deceleration than is the case at VHF frequencies. This is the basic cause of the systematically higher UHF densities than VHF. We suggest that the most physically realistic estimates of bulk density are provided by the VHF data for this reason. To more realistically examine the bulk densities in light of these physical arguments, we removed all events with bulk densities greater than the sum of the mean and 3 standard deviations. The mean density and standard deviation were then re-calculated. This process was repeated until all of the densities fall within the range of the mean density + 3 standard deviations. This required 5 and 6 iterations for the UHF 3D densities and Ovr densities respectively. The VHF data required 12 and 11 iterations of this rejection routine for 3D densities and Ovr densities respectively.

After this process was complete, 83% of the original 3D data set (181 UHF and 674 VHF) and 82% of the original Ovr data set (179 UHF and 669 VHF) remain. These results are summarized in Table 18, where the mean bulk density is represented by ρ_d, 3D and Ovr represent which masses are used in the calculation and s represents the standard deviation.

Figures (74) and (75) show the distribution of densities after the application of the outlier rejection routine as described above. Figure 75a shows the initial mass distributions of the VHF

population. Our results are most applicable to masses ~1 ?g. We will only analyse VHF data as most physically pertinent (for the reasons described earlier). It is clear that the mean, median and mode for VHF densities measured using either mass technique is roughly in the range 700-900 kg/m^3, though the distribution has a substantial higher density tail (as exemplified by the large standard deviation) which we believe to be genuine. While our rejection routine removed all of the higher (>3000 kg/m^3) meteoroids at VHF, we cannot rule out the possibility that some small portion of the population does have somewhat higher densities. It is, however, clear that the vast majority of the population have very low densities, most consistent with highly porous objects and inconsistent with solid stoney objects comparable in bulk properties to recovered chondritic meteorites or asteroids, the mean densities for which are shown in Figure 76.

In contrast, the bulk densities we derive are very similar to those determined for cometary nuclei, which have been variously measured to be in the range 200 – 900 kg/m^3 (cf. Sagdeev et al, 1988; Davidsson et al., 2004; Sirono and Greenberg, 2000) and aggregate IDPs (Rietmeijer and Nuth, 2002) (~700 kg/m^3) which are believed to come from comets. Note that the cometary nuclei density measurements may be misleading in that they may have a rubble-pile structure and hence some portions of the comet nucleus could be much denser than the bulk density alone indicates.

Table 18. Summary of density calculations for UHF and VHF meteors.

	$?_{d(3D)} \pm s$ (kg/m^3)	Median (kg/m^3)	$?_{d\,(Ovr)} \pm s$ (kg/m^3)	Median (kg/m^3)
UHF	2700 ± 2100	2232	2800 ± 2100	2076
VHF	800 ± 600	634	900 ± 600	743

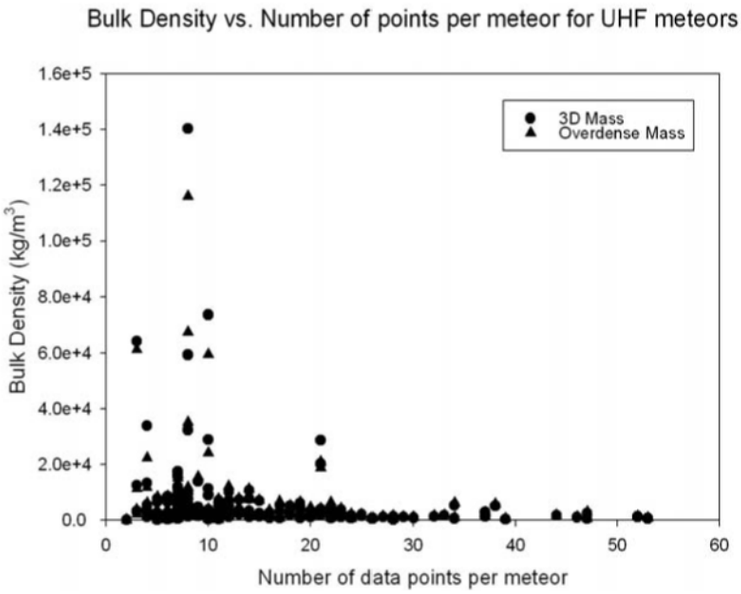

Figure 72. Bulk density vs. number of points for UHF meteors.

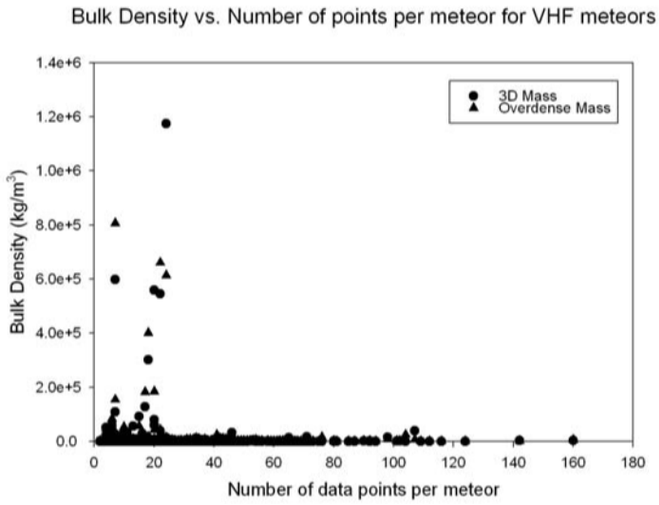

Figure 73. Bulk density vs. number of points per meteor for VHF meteors.

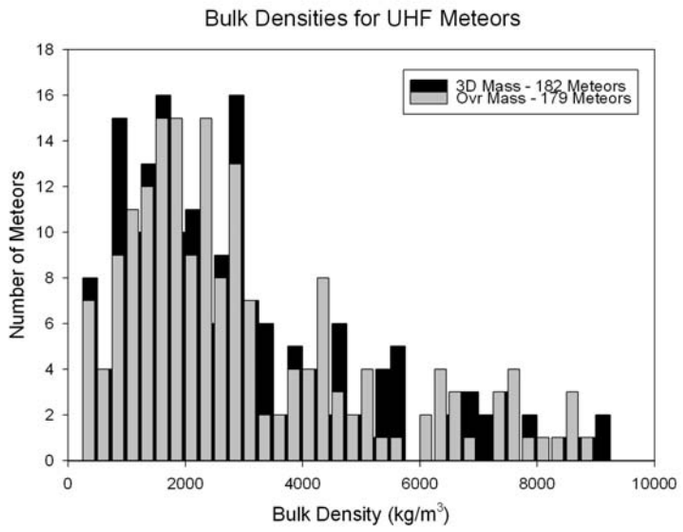

Figure 74. Bulk density for final dataset of head echoes observed at UHF.

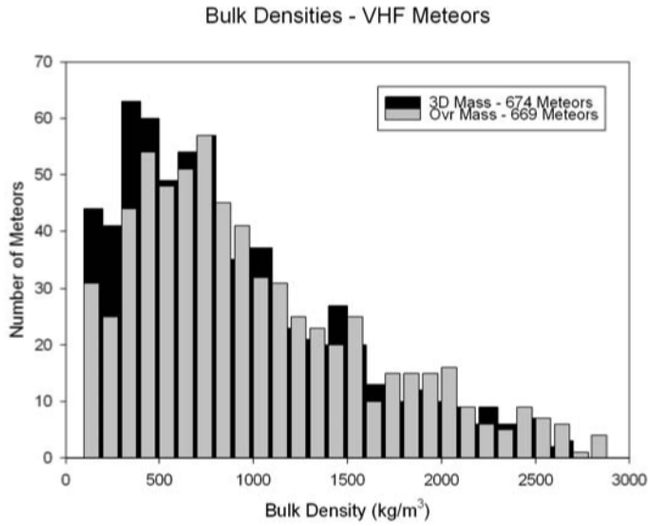

Figure 75. Bulk density for final dataset of head echoes observed at VHF.

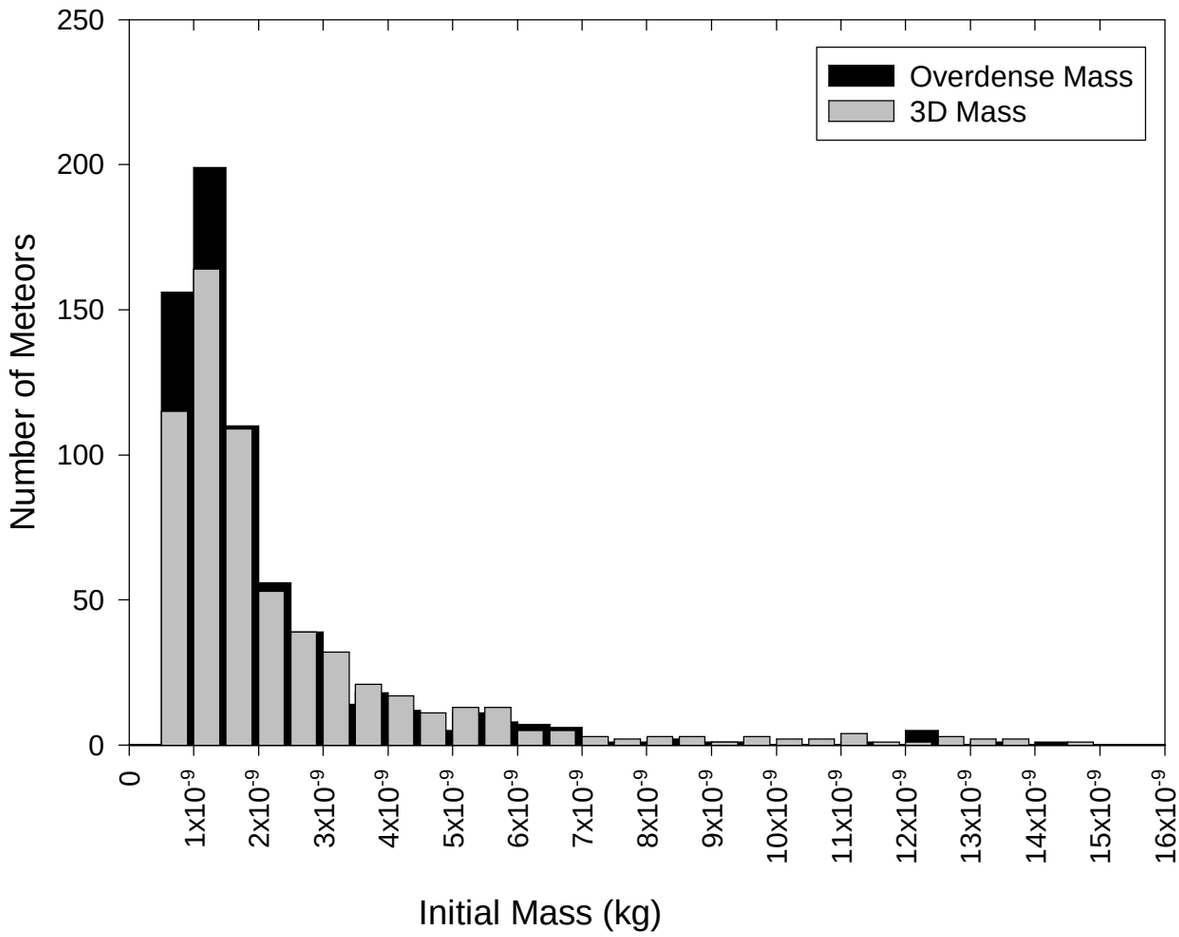

Figure 75 a. Initial masses for the VHF meteoroids.

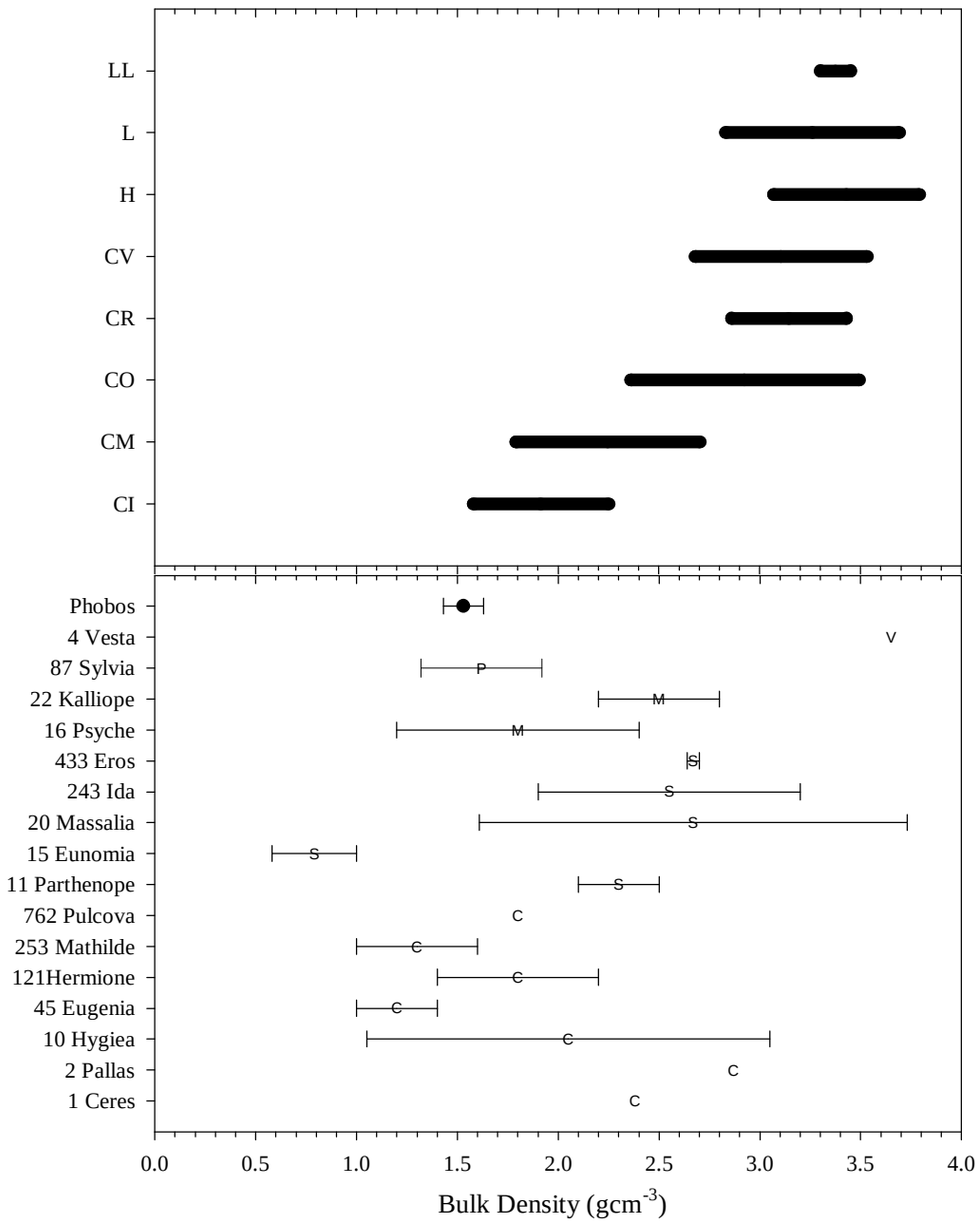

Figure 76. The range of measure bulk densities for meteorites of various chemical types (top plot) as derived from data given in Britt and Consolmagno (2000). Inferred bulk densities for various asteroids is shown in the lower plot as derived from various source (cf. Hilton, 2002).

3.6 Previous Studies

The methods which have been employed to determine meteoroid densities are as varied as the results they have obtained. An overview of previous investigations into this topic is presented here, and summarized in Table 19.

3.6.1 Non-Fragmenting Methods

Verniani (1964) applies single body theory to faint super-schmidt photographic meteors at the height of maximum light of the meteor to determine meteoroid bulk density. Doing the analysis at one single point of the meteor path eliminates the need for information about decelerations. This method is applied to 284 sporadic meteors observed by Hawkins and Southworth. In addition, meteoroid densities are calculated directly from the drag equation for 247 meteors observed, but unpublished by Jacchia. The result of this investigation is a mean bulk density of 0.22 ± 0.02 g/cm^3 for the Hawkins and Southworth data and 0.21 ± 0.01 g/cm^3 for the Jacchia data. Verniani (1969) also arrives at similarly low values for bulk densities analyzing a different set of Super-Schmidt meteors. The masses for these meteoroids are between 10^{-5} to 10^{-2} kg.

Jose-Trigo et al. (2002) applies the equations of single body theory to 285 sporadic photographic meteors catalogued by Jacchia et al. (1967). The catalogued data was observed using a Super-Schmidt camera, whose rotating shutter enables velocities and decelerations to be determined. Of the 285 sporadic meteors, 204 were found to be well described by the equations of single body theory. The mean density of these sporadic meteors was found to be 810 kg m^{-3}.

3.6.2 Methods Including Fragmentation

Babadzhanov (2002) incorporates quasi-continuous fragmentation which is a gradual release of the smallest fragments from the surface of a parent meteoroid and their subsequent evaporation. This method involves modeling light curves using the equations of quasi-continuous fragmentation and using a variety of bulk densities. Bulk density is then determined from the simulated light curve which best matches the actual light curve. This study includes 39 sporadic meteoroids all with masses greater than 0.01g and determines a bulk density of 2.2 ± 0.3 g /cm^3. In a similar investigation, Babadzhanov (1993) determined a mean density of 4.1 g/cm^3 for 24 sporadic meteors.

3.6.3 Direct Measurement Methods

McDonnell and Gardner (1998) use impact data to infer the density of interplanetary dust particles. In this study thin foils and thick targets are exposed to the same flux of interplanetary dust particles. Two types of targets are used as impact physics shows that particles have different impact mechanisms based on the type of target. The impacted targets are compared with simulations. The impacting bodies were determined to have densities in the range 2.0 - 2.4 g/cm^3 and masses in the range 10^{-15} - 10^{-9} kg

Love et al. (1994) determined densities for 150 interplanetary dust particles harvested in the stratosphere. The interplanetary dust particle masses are determined using X-ray techniques. Volumes are estimated using cross sections, measured with a scanning electron microscope and heights measured with differential focus methods. The average interplanetary dust particle density is found to be 2 g/cm^3 with densities ranging from 0.3-6.2 g/cm^3.

The results of the methods discussed are summarized below.

Table 19. Summary of previous studies into meteoroid bulk densities.

Author		Density	Mass Range	No. of Measurements
Babadzhanov	(2002)	2.2 ± 0.3 g /cm^3	>0.01 g	39
Rubio	(2002)	810 kg/m^3	10^{-5}-10^{-2} kg	204
M^{c}Donell	(1998)	2.0 - 2.4 g /cm^3	10^{-15} - 10^{-9} kg	Na
Love	(1994)	2.2 g /cm^3	Na	150
Babadzhanov	(1993)	4.1 g /cm^3	Na	24
Verniani	(1969)	0.28 ± 0.02 g /cm^3	10^{-5}-10^{-2} kg	220
Verniani	(1964)	0.22 ± 0.02 g /cm^3	Na	284
		0.21 ± 0.01 g /cm^3	Na	247

3.7 Orbital Characteristics of the Observed Population

In an effort to further define the population of meteoroids observed by ALTAIR, orbits for each meteoroid whose bulk density was measured was also made as described earlier. It is critical to note that the pointing direction for the ALTAIR beam throughout the data collection was directed largely at the North Apex sporadic source (cf. Jones and Brown, 1993). Figure 77 shows the sporadic sources in sun-centered coordinates along with the pointing directions for all 21 data collects showing this bias. The North Apex source has been previously shown to be populated by material released from long period comets. Thus we would expect, a priori, to sample only meteoroids released from this comet population.

Figure 78 shows the orbital inclination for all VHF meteors. It is clear that the vast majority are in high inclination orbits, most consistent with this cometary interpretation. Figure 79 shows the semi-major axis distribution for the population. As with the broader Apex population orbital distribution (shown in the left panel in figure 79), the orbits do not generally have the very large semi-major axis of the long period comet population. Much of these meteoroids have very small semi-major axes. One possibility is that this is due to orbital evolution under the influence of radiation effects (like the Poynting-Robertson effect) which has shrunk the initial large semi-major axes relative to the parent orbits. More likely this is an observational bias – we are much more likely to encounter meteoroids with semi-major axis which are small (similar to the Earth) and so this is a "selected" sub-population, representative of a much larger total population of high inclination particles. Similarly, the velocity interval which produces a given semi-major axis range scales as 1/a; hence the region populated by a given velocity interval in semi-major axis space becomes much larger at large a's. We also note that high ejection velocities opposite the cometary velocity vector could greatly reduce the semi-major axis of an initially large orbit, as, for example, might occur for a small proportion of the dust ejected by sun-grazing comets. It is also worth noting that ~25% of all VHF head echoes were hyperbolic, so some larger semi-major axis portion of the population may remain, or some error in measurement of the true velocity may be present. Figure 80 shows the eccentricity distribution. This plot highlights the large number of hyperbolic meteoroids (HMs) (every orbit with $e>1$ is hyperbolic) in the sample. Our sampled mass regime is of the same order of magnitude as that measured by the AMOR radar (Baggaley et al., 1994). The AMOR system detects ~2% of the total population as being potentially interstellar (Baggaley 2000) which is difficult to reconcile with our ~25% value even allowing for biases associated

with our pointing at the North Apex source direction. We also note that Baggaley (2000) does not see a significant excess of potential HMs toward the Earth apex direction.

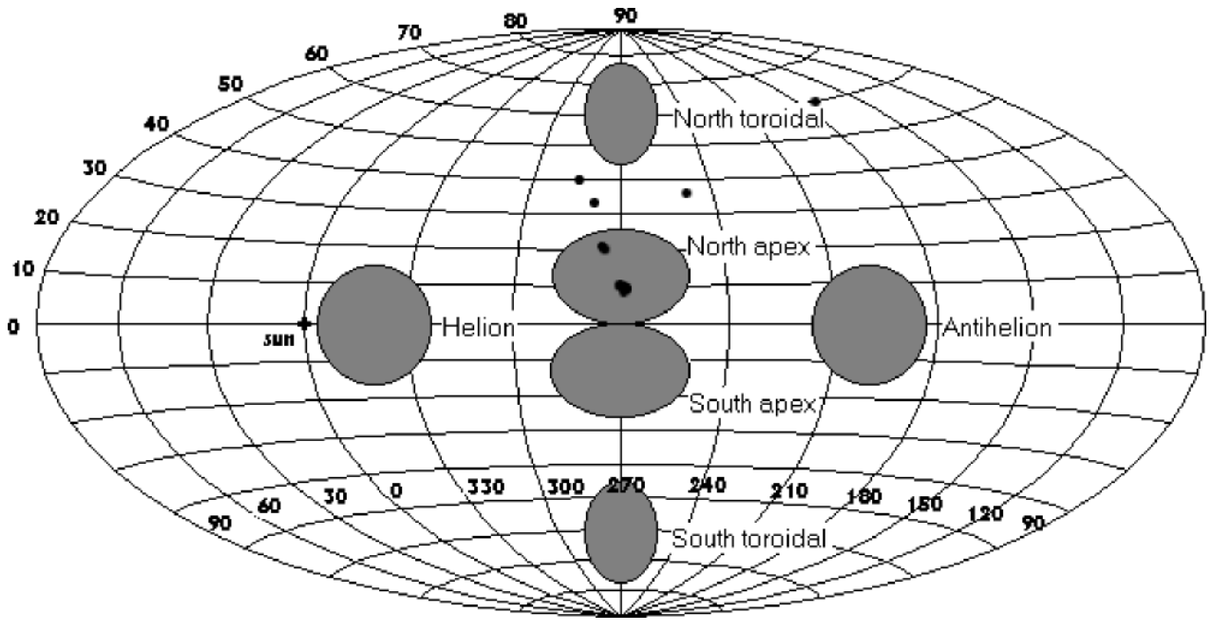

Figure 77. ALTAIR beam pointing directions in heliocentric coordinates.

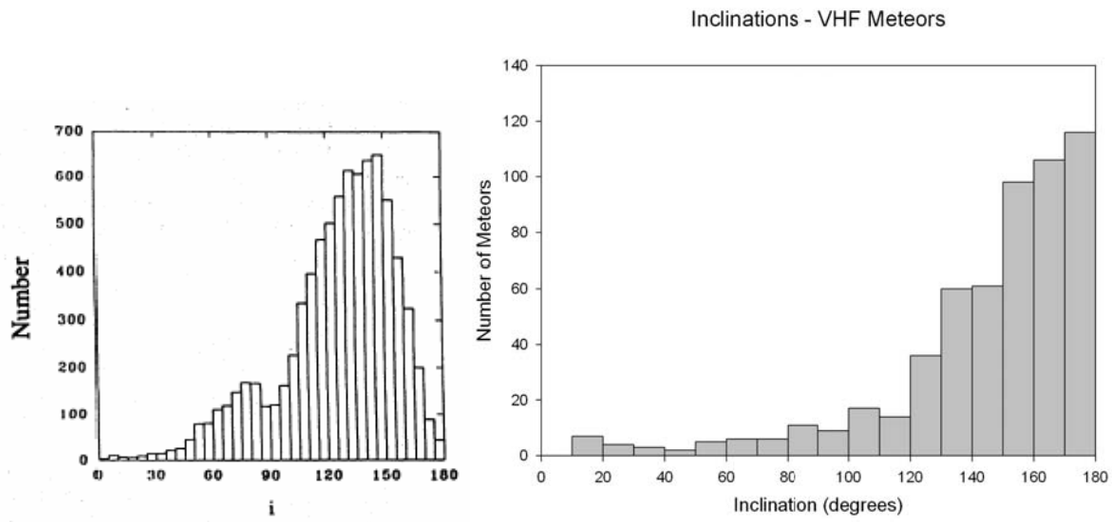

Figure 78. Orbital inclinations for VHF meteors (right). The inclination distribution for the North Apex source more broadly defined by various orbital surveys as summarized in Brown and Jones (1994) is shown at left.

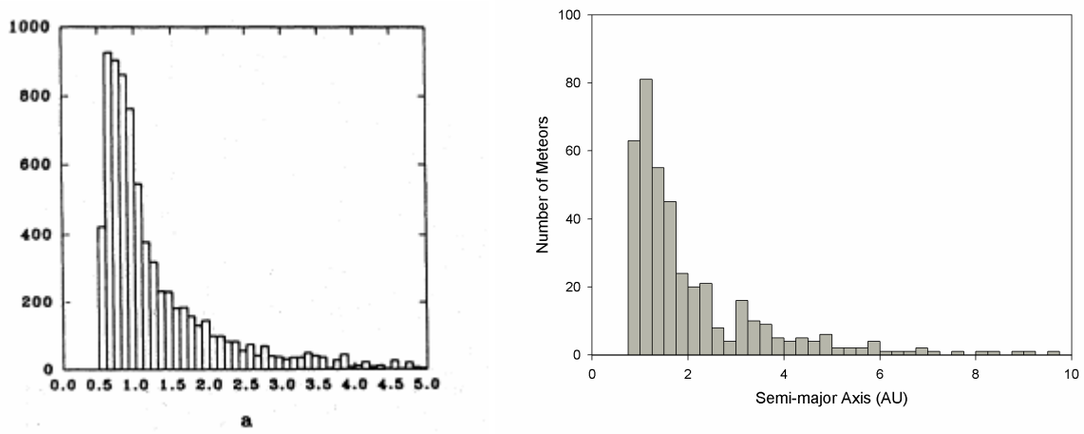

Figure 79. Semi-major axis distribution for VHF meteors (right). The semi-major axis distribution for the North Apex source more broadly defined by various orbital surveys as summarized in Jones and Brown (1993) is shown at left.

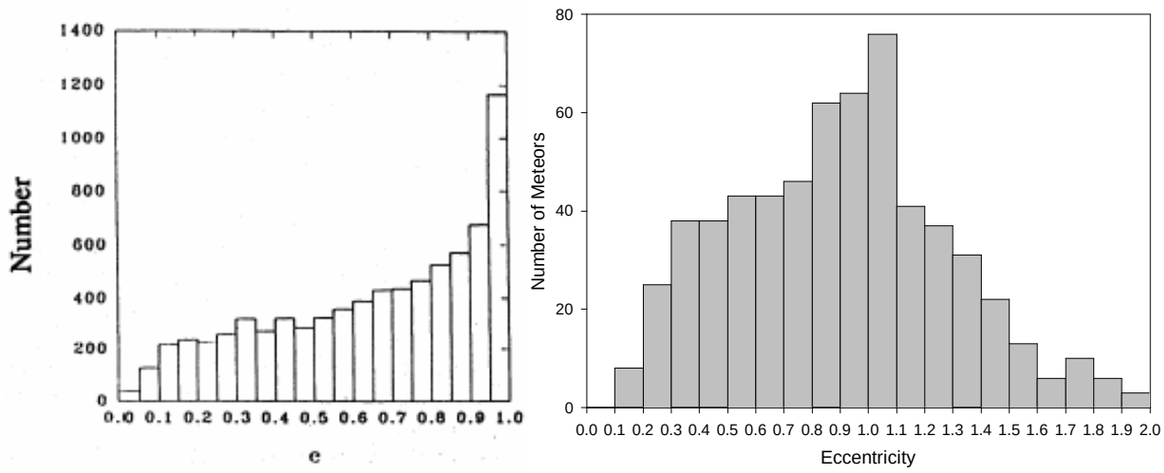

Figure 80. Eccentricity distribution for VHF meteors (right). The eccentricity distribution for the North Apex source more broadly defined by various orbital surveys as summarized in Brown and Jones (1993) is shown at left.

Bibliography

Babadzhanov., P. B.: Densities of meteoroids. In *Meteoroids and their Parent Bodies*, pp. 295-302, 1993.

Babadzhanov. P. B.: Fragmentation and densites of meteoroids. *Astronomy and Astrophysics*, (384):317-321, 2002.

Baggaley, W. J., R. G. T. Bennett, D. I. Steel, and A. D.Taylor: The advanced meteor orbit radar facility - AMOR. *Royal Astronomical Society, QUARTERLY JOURNAL*, (**35**):293-320, September 1994.

Baggaley, W. J.: Advanced meteor orbit radar observations of interstellar meteoroids. *Journal of Geophysical Research*, (**105**):10353-10362, 2000.

Beech. M.: The structure of meteoroids. *Monthly Notices of the Royal Astronomical Society*, (**211**):617-620, December 1984

Britt, D. and S. J. Consolmagno (2000): The porosity of dark meteorites. *Icarus*, (**146**):213-219.

Bronshten. V. A.: Physics of meteoric phenomena. Fizika meteornykh iavlenii, Moscow, Izdatel'stvo Nauka, 1981) Dordrecht, D. Reidel Publishing Co., 1983, 372 p. Translation., 1983.

Ceplecha, Z.: Geometric, dynamic, orbital and photometric data on meteoroids from photographic fireball networks. *Astronomical Institutes of Czechoslovakia, Bulletin*, (**38**):222-234, 1987.

Ceplecha, Z. K, et al.: Meteor phenomena and bodies . *Space Science Reviews*, (84): 327-471, 1998.

Close, S.: Theory and analysis of meteor head echoes and meteoroids using height-resolution multi-frequency radar data, 2004.

Davidsson, B. J. R. and P. J. Gutierrez: Estimating the nucleus density of Comet 19P/Borrelly. *Icarus* (168):392-408, 2004.

Greenberg, J. M. and J. I. Hage: From interstellar dust to comets – A unification of observational constraints, *Astrophysical Journal*, (36):260-274, 1990.

Grogan, K., S. F. Dermott, and D. D. Durda: The size-frequency distribution of the zodiacal cloud: Evidence from the solar system dust bands, *Icarus*, (**152**):251-267, 2001.

Gustafson, B. A. S.: 1994, Physics of zodiacal dust. Annual Review of Earth and Planetary Sciences, (22): 553.

Hilton, J. L.: Asteroid masses and densities in asteroids III, ed. Bottke, W.F., Cellino, A., Paolicchi, P. and R.P. Binzel), University of Arizona Press, pp. 103-112.

Hawkes R. L. and J. Jones: A quantitative model for the ablation of dustball meteors. *Monthly Notices of the Royal Astronomical Society*, (**173**):339-356, November 1975.

Jacchia. L.G.: The physical theory of meteors. viii. fragmentation as cause of the faint meteor anomaly. *Astrophysical Journal*, (**121)**:521—527, March 1955.

Janches, D., J. D. Mathews, D. D. Meisel, and Q. H. Zhou: Micrometeor observations using the arecibo 430 MHz Radar. I. Determination of the ballistic parameter from measured doppler velocity and deceleration results, *Icarus*, (**145**):53-63.

Jacchia. L. G.: The moon, meteorites and comets. 1963.

Jones, J. and P. Brown: Sporadic meteor radiant distributions: orbital survey results. *Mon. Not. R. Astron. Soc.* (**265):**524-532, 1993.

Justus, C. G and D. L. Johnson: The gram model: status of development and future aspects, *Advances in Space Research*, Volume 19, Issue 4, p. 549-558

Levin, B.: The physical theory of meteors and meteoric matter in the solar system, 1956.

Love, S. G., D. J. Joswiak, and D. E. Brownlee: Densities of stratospheric micrometeorites. *Icarus*, (**111**):227-236, 1994.

McDonnell, J. A. M. and D. J. Gardner: Meteoroid morphology and densities: decoding satellite impact data. *Icarus*, (**133**):25-35, 1998.

McKinley, D. W. R.: Meteor science and engineering. McGraw-Hill, 1961.

Nagel, K., G. Neukum, J. S. Dohnanyi, H. Fechtig, and W. Gentner: Density and chemistry of interplanetary dust particles, derived from measurements of lunar microcraters. In *Lunar and Planetary Science Conference*, pages 1021-1029, April 1976.

Rietmeijer, F. and J. Nuth: Collected extraterrestrial materials: Constraints on meteor and fireball compositions. *Earth, Moon and Planets*, (**82/83**):325-350, 2000.

Rubio et al.: Modeling the photometric and dynamical behavior of super-schmidt meteors in the earth's atmosphere. *Astronomy and Astrophysics*, (**389**):680-691, 2002.

Sagdeev et al.: Is the nucleus of Comet Halley a low density body? *Nature*, (**331**):240-242, 1988

Sirono, S. and J. M. Greenberg: Do cometesimal collisions lead to bound rubble piles or to aggregates held together by gravity. *Icarus* (**145**): 230-238, 2000.

Verniani, F.: Il Nuovo Cimento, (**33**):1173-1184, August 1964.

Verniani, F.: Structure and fragmentation of meteoroids. *Space Science Reviews*, (**10**):230, 1969.

Whipple, F. L.: A comet model. i. the acceleration of Comet Encke. *Astrophysical Journal*, (**111**):375-394, March 1950.

Whipple, F. L.: A comet model. ii. physical relations for comets and meteors. *Astrophysical Journal*, (**113**):464-474, May 1951.

4. DATABASE

4.1 Background and Justification

The Meteor Properties Database is a Microsoft Access 2000 program that can be used with any version of MS Access 2000 or higher. Chosen because of its widespread use, this database management system was used to build a user-interactive querying environment capable of probing meteor data collected by ALTAIR and analyzed by collaborators at MIT-Lincoln Laboratory and the University of Western Ontario. Another factor in the decision to use MS Access was that it, as an integral part of the MS Office family, has an added bonus beyond that of general familiarity: data can be exported to MS Excel for further analysis and graphing. Additionally, the Query-By-Form feature in MS Access makes user-interactive queries easy to program and intuitive for the user.

4.2 Distribution and Installation

The Meteor Properties Database is a 17 MB file distributed via CD-ROM by NASA's Space Environments and Effects (SEE) Program and is subject to export control. As stated previously, it can be used with any version of MS Access 2000 or higher.

The CD-ROM contains an electronic copy of the final report and the database itself, "MeteorProperties.mdb". The user has only to double-click this file to launch the Meteor Properties Database. The warning "The database 'MeteorProperties' is read-only" will appear. Click "Ok." This should not affect the functioning of the database in any way. Please make sure that MS Access is open in full-screen mode and that your screen resolution settings are at least 1024 x 768 pixels.

4.3 Organization

The Main Switchboard, the main means of navigation, will appear when the database is launched. The Switchboard offers the user 7 different query options:

1. ***Observational queries*** – query information about the observation conditions, namely the frequency at which meteors were detected and analyzed (UHF, VHF, both UHF and VHF, etc), the date and time of observation, and the pointing direction of the ALTAIR beam.

2. ***Physical data queries*** – query the density and mass of the meteor according to which scattering solution (3D Spherical or Overdense) was used in the analysis.

3. ***Velocity queries*** – query the various velocity measurements and calculations, including heliocentric, geocentric, initial, and pre-atmospheric velocities.

4. ***Orbital parameter queries*** – query the semi-major axis, eccentricity, perihelion distance, aphelion distance, argument of perihelion, longitude of the ascending node, and inclination of the meteoroid orbit.

5. ***Radiant position queries*** – query the various methods for specifying the position of the radiant, both geocentric and apparent. This includes right ascension and declination, latitude and longitude in ecliptic coordinates, and altitude and azimuth.

6. ***Meteor path queries*** – query the characteristics of the meteor path, namely the unit vector describing the path, the beam deviation angle, the first and last detected meteor heights, and the length of the path.

Each of the above queries are termed "simple queries" due to fact that they let the user explore one aspect of the meteors' characteristics – orbital *or* physical *or* velocity calculations, etc. They are quick queries if, for example, you are just interested in how many meteors have hyperbolic orbits, *or* what meteors have a mass above a certain limit.

But if you want to know how many meteors have hyperbolic orbits *and* masses above a certain limit then the simple queries are too rudimentary. To explore multiple aspects of the meteors' characteristics – orbital *and* physical *and* velocity calculations, etc. – the last query on the Main Switchboard, " Advanced queries" is necessary.

7. ***Advanced queries*** – combines all of the aspects of the observational, physical data, velocity, orbital parameter, radiant position, and meteor path queries on 6 different tabs and allows the user to set limits on the errors where possible.

The last three command buttons on the Switchboard are "Help" which gives you this same organizational information, "About" which gives general information about the database and contact information, and "Exit" which exits the application.

4.4 Querying

The colored labels indicate the fields over which you may query. On the Advanced queries form these fields are located under each tab. Upper and lower bounds may be input in the text boxes provided. Additionally, you may restrict the amount of error in the calculation on the Advanced queries form, where possible.

Default values are entered into the text boxes when the query form is loaded. These values appear in gray. The defaults span the entire range of data, and are designed to return all values of the field to which they are tied. You may enter your own bounds for any field – if you do, these values appear in black text. If you delete a default and do not enter a replacement value your query will return no results.

To perform a query, click the "Run Query" command button. A short pause in activity may occur as searching commences, but the results of your query will open in a new window.

To return all of the lower and upper bounds (and their associated errors in the Advanced case) to their default values, click the "Reset to Defaults" command button. The query form will be reloaded.

For help with querying or various field definitions the "Help" command button is useful. The last button, "Back to Main", returns you to the Main Switchboard.

4.5 Querying Field Definitions

A brief description of each field over which you may query can be found in the Status Bar at the bottom of the screen when you click in any of the text boxes related to the field of interest in any of the query forms. For an in-depth description of the fields, see Table 20, where all of the fields comprising the results are described. The fields over which the user may query have the Query Name listed. All Query Names with colored labels can also be queried with the "Advanced queries" form. The fields *only* searchable with the "Advanced queries" form are indicated. For a description of the science, see Section 2 – Radar Observations and Analysis – and Section 3 – Orbit and Bulk Density Analysis.

4.6 Query Results

The results of your query will open in a new window in spreadsheet form, with a meteor in each row and its properties in the adjacent columns. The scroll bars at the bottom and right side of the window allow you to navigate the results. The Record Selector, which also allows navigation from meteor to meteor via the arrow buttons, displays the number of results matching the query parameters.

A brief description of the columns making up the results can be seen in the Status bar at the bottom of your screen when you click on the column heading, or when you click in the field of interest. For further description, see Table 20.

If there are no rows present beyond the column headers then there are no results. Try varying your input parameters.

Each of the 7 queries have their own default sorting scheme as follows:

1. *Observational queries* – sorted by increasing date and time.
2. *Physical data queries* – sorted by increasing density.
3. *Velocity queries* – sorted by increasing heliocentric velocity.
4. *Orbital parameter queries* – sorted by increasing semi-major axis.
5. *Radiant position queries* – sorted by increasing date and time.
6. *Meteor path queries* – sorted by increasing initial height.
7. *Advanced queries* – sorted by increasing date and time.

You may sort by any column you wish by clicking the column heading of interest, right clicking on the mouse, and selecting “Sort Ascending” or “Sort Descending”. To sort multiple adjacent columns simultaneously, hold down the shift key and select the column headings of interest, and then right click to select “Sort Ascending” or “Sort Descending” while still holding Shift. The columns will be sorted from left to right.

To save the query results as an MS Excel file or a text file, use the “Save as .xls” and “Save as .txt” command buttons, respectively. An “Output To” window will appear allowing you to choose a directory and filename for your results. When saving the results, the default sorting scheme is used.

The “Print results” command button prints the results of your query to your default printer. When printing the results the default sorting scheme is used. A cautionary note: the 60+ columns and *x* number of rows of data making up your results may eat up quite a bit of paper.

For help manipulating the results or determining the various field definitions the “Help” command button is useful. The “Close” command button closes the results form.

4.7 Contact Information

For additional information regarding this database contact:

Space Environments and Effects Program
http://see.msfc.nasa.gov/

Table 20. All of the fields comprising the results are described. The fields over which the user may query have Query Names with colored labels can also be queried with the "Advanced queries" form. The fields *only* searcl queries" form are indicated.

Query Name	Field name	Definition
	Dataset name	Name of the dataset; for reference. "Mvper981645" corresponds tc 1998 at 16:45 UT. "Muleo991654" corresponds to a UHF Leonid (
	Tag	Meteor tag number; for reference. The combination of Dataset na
Observational	Obs. Type	Type of observation: UHF (422 MHz) or VHF (160 MHz).
Observational	Dual	If the meteor was observed in both UHF and VHF, "Yes" will app meteor was observed in either UHF or VHF, "No" will appear.
	Corresp. tag	If meteor was observed in both UHF and VHF (Dual column = Ye tag number of the corresponding meteor in the other frequency ran Type = UHF, Dual = Yes, and Corresp. tag = 75. "Mvleo981500" meteor detected at VHF.
Observational	Year	The year of observation. This data was collected during the Leoni and the Perseid shower of 1998.
Observational	Month	The month of observation. As this data was collected during the P only two values of the month field are 8 and 11.
	Day	The day of observation. There were only two distinct month/day c August 12th and November 17th -- so there is no need to search or
Observational	UT	The UT (Universal Time) of observation.
Observational	Beam_x	Pointing direction of ALTAIR beam; normalized unit vector (x co
Observational	Beam_y	Pointing direction of ALTAIR beam; normalized unit vector (y co
Observational	Beam_z	Pointing direction of ALTAIR beam; normalized unit vector (z co
Physical data	No. 3D pts	Number of data points (radar pulse returns) used in the 3D spheric
Physical data	Density – 3D	Mean bulk density determined using the 3D spherical model masse for each radar pulse return was calculated and averaged.
Advanced only	St. dev (3D density)	Standard deviation in Density – 3D, the standard deviation in the b to point (kg).
Physical data	Initial mass – 3D	Initial mass of the meteor according to the 3D spherical model (kg
Advanced only	Mu – 3D	Best-fit shape variation parameter for bulk density determined usir
Advanced only	K – 3D	Shape factor for 3D spherical model analysis; see Ceplecha et al (1
Physical data	No. OverD pts	Number of data points (radar pulse returns) used in the Overdense
Physical data	Density – OverD	Mean bulk density determined using the Overdense model masses for each radar pulse return was calculated and averaged.

Table 20. All of the fields comprising the results are described. The fields over which the user may query have Query Names with colored labels can also be queried with the "Advanced queries" form. The fields *only* searcl queries" form are indicated. (Continued)

Query Name	Field name	Definition
Advanced only	St. dev (OverD density)	Standard deviation in Density – OverD, the standard deviation in t point to point (kg).
Physical	Initial mass – OverD	Initial mass of the meteor according to the Overdense model (kg).
Advanced only	Mu – OverD	Best-fit shape variation parameter for bulk density determined usir
Advanced only	K – OverD	Shape factor for Overdense model analysis; see Ceplecha et al (19
Velocity	Heliocentric velocity	Heliocentric velocity of the meteor (km/s).
Advanced only	d Helio velocity	Error in the heliocentric velocity calculation (km/s).
Velocity	Geocentric velocity	Geocentric velocity of the meteor (km/s).
Advanced only	d Geo velocity	Error in the geocentric velocity calculation (km/s).
Velocity	Pre-atmos. velocity	Pre-atmospheric velocity of the meteor (km/s). Corrected for dece
Velocity	Initial velocity	Initial instantaneous velocity of the meteor (km/s). This is the velc data point.
Orbital param.	Semi-major axis (a)	Orbital parameter: semi-major axis of the meteoroid orbit (AU).
Advanced only	d Semi-major axis	Error in the semi-major axis calculation (AU).
Orbital param.	Eccentricity (e)	Orbital parameter: Eccentricity of the meteoroid orbit.
Advanced only	d Eccentricity	Error in the eccentricity calculation.
Orbital param.	Perihelion distance	Orbital parameter: Perihelion distance (AU).
Advanced only	d Perihelion distance	Error in the perihelion distance calculation (AU).
Orbital param.	Aphelion distance	Orbital parameter: Aphelion distance (AU).
Advanced only	d Aphelion distance	Error in the aphelion distance calculation (AU).
Orbital param.	Argument of Perihelion (Omega)	Orbital parameter: Argument of perihelion (degrees).
Advanced only	d Omega	Error in the argument of perihelion calculation (degrees).
Orbital param.	Ascending node	Orbital parameter: Longitude of the ascending node (degrees).
Advanced only	d Ascending node	Error in the longitude of the ascending node calculation (degrees).
Orbital param.	Inclination	Orbital parameter: Inclination of the meteoroid orbit (degrees).
Advanced only	d Inclination	Error in the inclination calculation (degrees).
Radiant pos.	Geocentric Ra	Right ascension of the geocentric radiant (degrees). Corrected for rotation.
Advanced only	d Geo Ra	Error in the geocentric right ascension calculation (degrees).
Radiant pos.	Geocentric Dec	Declination of the geocentric radiant (degrees). Corrected for Eart

Table 20. All of the fields comprising the results are described. The fields over which the user may query have Query Names with colored labels can also be queried with the "Advanced queries" form. The fields *only* searcl queries" form are indicated. (Concluded)

Query Name	Field name	Definition
Advanced only	d Geocentric Dec	Error in the geocentric declination calculation (degrees).
Radiant pos.	Ecliptic longitude (Lambda)	Ecliptic longitude of the geocentric radiant (degrees).
Advanced only	d Lambda	Error in the ecliptic longitude calculation (degrees).
Radiant pos.	Ecliptic latitude (Beta)	Ecliptic latitude of the geocentric radiant (degrees).
Advanced only	d Beta	Error in the ecliptic latitude calculation (degrees).
Radiant pos.	Apparent Ra	Right ascension of the apparent radiant (degrees).
	d App Ra	Error in the apparent right ascension calculation (degrees).
Radiant pos.	Apparent Dec	Declination of the apparent radiant (degrees).
	d App Dec	Error in the apparent declination calculation (degrees).
Radiant pos.	Altitude	Altitude of the apparent radiant (degrees).
Radiant pos.	Azimuth	Azimuth of the apparent radiant (degrees).
Meteor path	U	Unit vector of the meteor trajectory (U component, east wrt ALTA
Meteor path	V	Unit vector of the meteor trajectory (V component, north wrt ALT
Meteor path	W	Unit vector of the meteor trajectory (W component, zenith wrt AL
Meteor path	Beam dev. angle	Deviation angle between the ALTAIR beam direction and the met
Meteor path	Initial height	Initial height of the meteor (km). The height of the meteor at first
	Max RCS height	Height of the meteor with maximum radar cross section (km).
Meteor path	Final height	Final height of the meteor (km). The height of the meteor at last d
Meteor path	Path length	Length of the meteor path (km).